UNIVERSITY OF OKLAHOMA

GRADUATE COLLEGE

POROELASTIC AFTER-CLOSURE PRESSURE DECLINE ANALYSIS IN DUAL-POROSITY DUAL-PERMEABILITY FORMATIONS

A DISSERTATION

SUBMITTED TO THE GRADUATE FACULTY

in partial fulfillment of the requirements for the

Degree of

DOCTOR OF PHILOSOPHY

By

CHAO LIU
Norman, Oklahoma
2016

POROELASTIC AFTER-CLOSURE PRESSURE DECLINE ANALYSIS IN DUAL-POROSITY DUAL-PERMEABILITY FORMATIONS

A DISSERTATION APPROVED FOR THE
MEWBOURNE SCHOOL OF PETROLEUM AND GEOLOGICAL ENGINEERING

BY

_____
Dr. Younane N. Abousleiman, Chair

_____
Dr. Shihshu W. Wei

_____
Dr. Ahmad Ghassemi

_____
Dr. Deepak Devegowda

_____
Dr. Xingru Wu

Dedicated to my family.

Acknowledgements

I would like to express my wholehearted and deepest gratitude to Dr. Younane N. Abousleiman who introduced me to the area of Poromechanics. I thank Dr. Abousleiman for his patient guidance, technical advice, encouragement of independent thinking and continuous support during my Ph.D. studies at the University of Oklahoma. His enthusiasm and commitment to academic excellence and insight into scientific and engineering problems have always motivated me to strive for the best.

Dr. Shihshu W. Wei, Dr. Ahmad Ghassemi, Dr. Deepak Devegowda and Dr. Xingru Wu are gratefully acknowledged for serving as my committee members.

I would also like to thank Dr. Shihshu W. Wei and Dr. Shengliang Pan (TongJi University, China) for helping me establish my foundation in mathematics. Their superior knowledge and great humility have always been my aspiration.

My special thanks go to my colleagues and friends, Dr. Son K. Hoang, Dr. Amin Mehrabian, Dr. Shengli Chen and Dr. Minh H. Tran, for their intellectual discussions, creative ideas and constructive criticism of my work. Special thanks also go to Ms. Carla L. Cates, the Administration and Operations Manager of the integrated PoroMechanics Institute, who is always so helpful during my studies at iPMI. I am also thankful to Mr. Junxin Guo, Miss Batoul H. Maatouk, Mr. Yang Zhou and Miss Thao P. Le for many stimulating discussions and their friendship with me.

I owe my great appreciation to my parents, Mr. Bingdong Liu and Ms. Haiping Wu, my brother, Mr. Zhibin Liu, and my sister, Ms. Nianzhao Liu, for their unconditional love and support. I am deeply indebted to my wife, Ms. Hong Jiang, and my son,

Xuanyu Liu, whose English name is Ian J. Liu, for their love, support and the happiness they bring to my life.

Table of Contents

List of Tables

List of Figures

Abstract

The dual-porosity and dual-permeability theory of poroelasticity is used to analyze the wellbore dual-pressure responses of dual-porosity or naturally fractured formations. The pressure decline is analyzed by modeling the dual-pressure regimes of the dual-porosity and dual-permeability medium during the after-closure phase of hydraulic fracturing. The analysis shows that both the matrix and natural fractures permeability, as well as the developed fracture length, can be estimated based on the obtained pseudo-linear and pseudo-radial dual-pressure and dual-flow regimes.

The estimations are made by use of the corresponding 1/2 and -1 slopes in the time-history plots of the wellbore pressure derivative. The transition period between pseudo-linear and pseudo-radial regimes is also analyzed. The solution involves three time scales related to the rate of fluid flow through and in between the matrix and fractures network. Findings indicate the possible emergence of an additional -1/2 slope in the log-log pressure-derivative plot of low-permeability shale formations. It is further shown that the transient pressure-response of the formation could be calibrated by incorporating an appropriate inter-porosity coefficient, as a measure of the linear fluid exchange capacity between the matrix and fracture porosities. The analytical expressions for the time markers of the upper limit for the pseudo-linear regime, lower limit for the pseudo-radial regime and the time at which the dip bases occur in pressure-derivative curves are given to estimate this parameter.

The solution is successfully applied to and matched with a published set of field data to provide estimations for the associated reservoir properties. The field data analysis is elaborated upon by a corresponding sensitivity analysis, through which the prominent

poroelastic parameters of the solution are determined. Lastly, the definition of conventional key parameters attributed to solutions of this type, such as formation total compressibility, storage coefficients and hydraulic diffusivity, are reformulated using the presented dual-porosity poroelastic approach to the problem.

Chapter 1 : Introduction

1.1 Introduction to Pressure Decline Analysis

Formation permeability determination is crucial in optimization of hydraulic fracturing design, oil and gas production. Formation permeability has traditionally been determined through well tests. Conventional pressure transient tests are powerful in formations with high permeability, but in tight formations with low permeability they can be time-consuming and provide only local estimates of formation properties if short-time tests are performed. Furthermore, the information might be affected by the near-wellbore damage and skin effects, where the formation permeability is decreased because of the accumulation of solid particles from the mud filtrate (Nunes et al. 2010). Conventional pressure buildup and drawdown transient pressure tests might even be impossible to determine the ultra-low permeability of unconventional formations, since the flow in such formations is ultra-slow without stimulation. Such disadvantages of conventional well testing could be avoided by using the “impulse fracture test” (Nolte 1979; Abousleiman 1991; Gu et al. 1993; Abousleiman et al. 1994; Nolte et al. 1997). In this test, a small volume of fluid is injected into the formation under pressure high enough to create a short fracture, and then the well is shut down, either locally close to the target depth or at the wellhead. The test is illustrated by Figure 1.1.

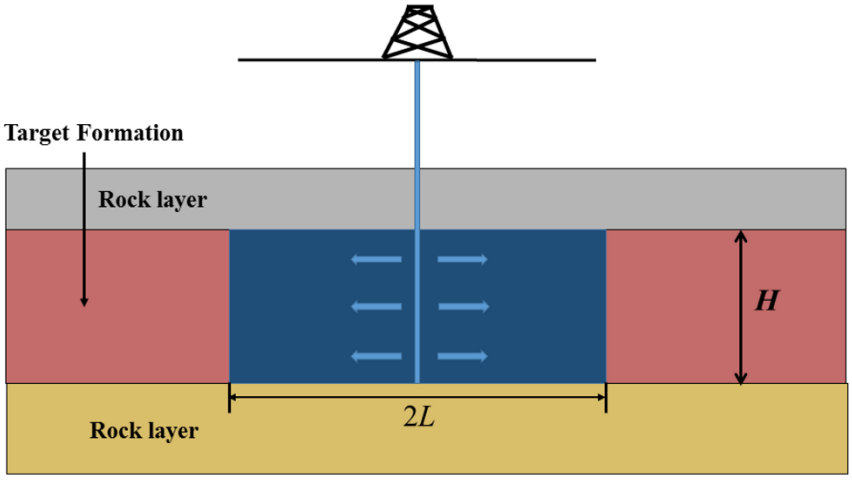

Figure 1.1—Illustration of the impulse fracture test. 2L is the created hydraulic fracture length, H is the fracture height.

The recorded pressure response is then used to estimate formation properties and fracture geometry. Figure 1.2 illustrates the typical wellbore pressure response during such test. A fluid is pumped into the wellbore at a constant rate. Wellbore pressure is increasing with pumping time and reaches the fracture initial pressure as time proceeds. During this time period, little of the injected fluid flows into the formation if the formation has low permeability. As surface pumping continues, formation breakdown pressure (the maximum wellbore pressure) is reached. Then wellbore pressure drops significantly due to hydraulic fracture propagation into the formation. When the pressure stabilizes, the injection is stopped. Then another significant pressure drop occurs because the friction in the wellbore decreases rapidly, based on which the instantaneous shut-in pressure can be determined. Without proppants, the hydraulic fracture closes as time proceeds and eventually fracture closure pressure is reached when the hydraulic fracture is closed. Details of such pressure definitions can be found in the literature (Nolte 1988; Cramer and Nguyen 2013). A clean fluid is

usually used in the impulse fracture test. The difference between the fracture initiation and breakdown pressures is small.

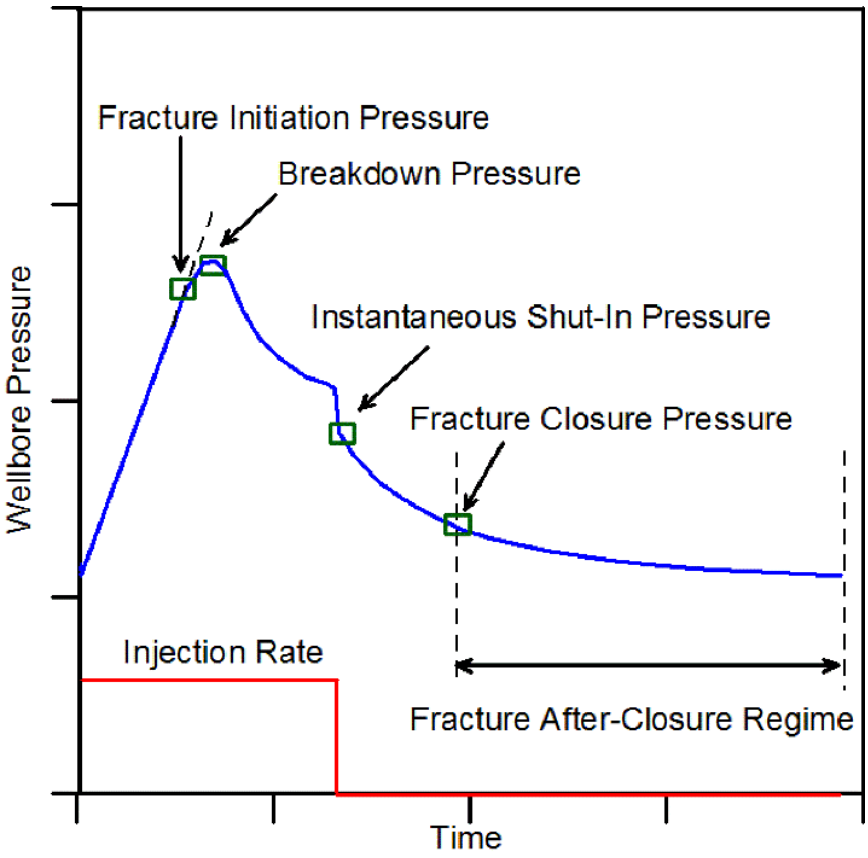

Figure 1.2—Schematic of wellbore pressure response during the impulse fracture test.

The impulse fracture test was originally used to determine the fluid leakoff coefficients, fracture closure time, fracture length and width (Nolte 1979; Kuhlman 1990; Economides and Nolte 2000). The reservoir properties determined by this test should be more representative of the reservoir and avoid the near-wellbore effects because the created fracture can pass through the damage zone and provide a larger area for true formation properties. Formation permeability is usually estimated through simulation of the fluid exchange between the hydraulic fracture and the formation rock

by a distribution of the fluid point sources (Gu et al. 1993; Abousleiman et al. 1994). The fluid point source distribution is defined along the trajectory of the fracture, with its intensity determined by the leakoff rate.

The pressure decline analysis consists mainly of two categories: pre-closure analysis and after-closure analysis. The pre-closure analysis focuses on the period after shut-in and before fracture closure while the after-closure pressure decline corresponds to the fracture after-closure regime, as shown in Figure 1.2. This dissertation focuses on the after-closure analysis.

1.1.1 Pre-Closure Analysis

Nolte (1979) first introduced the pre-closure analysis to estimate fracture closure pressure, leak-off coefficient, fluid efficiency, fracture length and width. A PKN model is selected to simulate the hydraulic fracture geometry, as illustrated in Figure 1.3. In the PKN model, a hydraulic fracture is simulated as a bi-wing fracture with constant height. Both horizontal and vertical cross sections of the fracture are ellipitical. The fracturing fluid pressure is constant in the vertical direction.

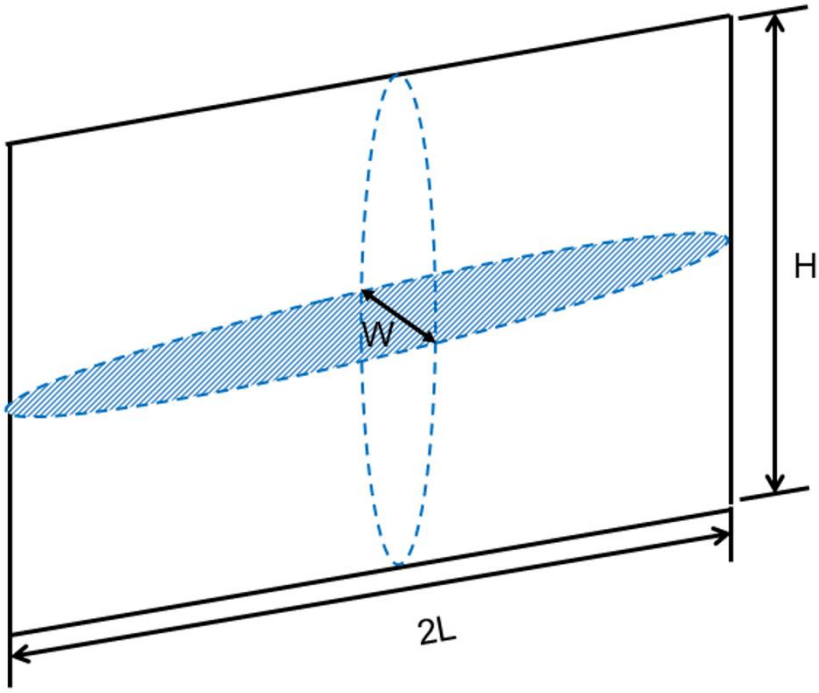

Figure 1.3—PKN model for the hydraulic fracture geometry. H is fracture height, W is fracture width, and 2L is fracture length.

The continuity equation for flow of an incompressible fluid in the fracture was presented by Nordgren (1972) as follows:

$$\frac{\partial q}{\partial x} + q_l + \frac{\partial A}{\partial t} = 0 \quad \text{..... (1.1)}$$

where $q(x,t)$ is the volume rate of flow through a cross section ($x = x_0$) of the fracture, $q_l(x,t)$ is the volume rate of fluid loss to the formation per unit length of fracture, $A(x,t)$ is the cross-sectional area of the fracture.

Solving equation 1.1, Nolte (1979) derived the following pressure variation during hydraulic fracture closure:

$$p_e - p_w(\Delta t_p) = \frac{H_p C_L E \sqrt{t_p}}{H^2(1-\nu^2)\beta_s} G(\Delta t_p) \quad \text{..... (1.2)}$$

where p_e is the pressure at the end of pumping, $\Delta t_p = (t-t_p)/t_p$, t_p is the pumping time, H_p is the fluid loss height, C_L is the leakoff coefficient, E is the Young's modulus, ν is the Poisson's ratio, and β_s is the ratio of average and wellbore pressure while shut-in, and

$$G(\Delta t_p) = \frac{4}{\pi}\left[g(\Delta t_p) - g_0\right] \quad \text{..... (1.3)}$$

$$g(\Delta t_p) = (1+\Delta t_p)\,ArcSin\left(1/\sqrt{1+\Delta t_p}\right) + \sqrt{\Delta t_p} \quad \text{for low fluid efficiency .....(1.4a)}$$

$$g(\Delta t_p) = \frac{4}{3}\left[(1+\Delta t_p)^{3/2} - (\Delta t_p)^{3/2}\right] \quad \text{for high fluid efficiency..... (1.4b)}$$

Equation 1.2 indicates that the pressure drop after shut-in and before fracture closure is proportional to G time. The linear proportional limit point allows estimation of the fracture closure pressure and closure time (Nolte 1979).

Barree (1998) introduced the curves of dp/dG and Gdp/dG vs. G time to assist with the identification of fracture closure pressure. The linear proportional limit of the curve Gdp/dG vs. G time also indicates the fracture closure, as illustrated by Figure 1.4.

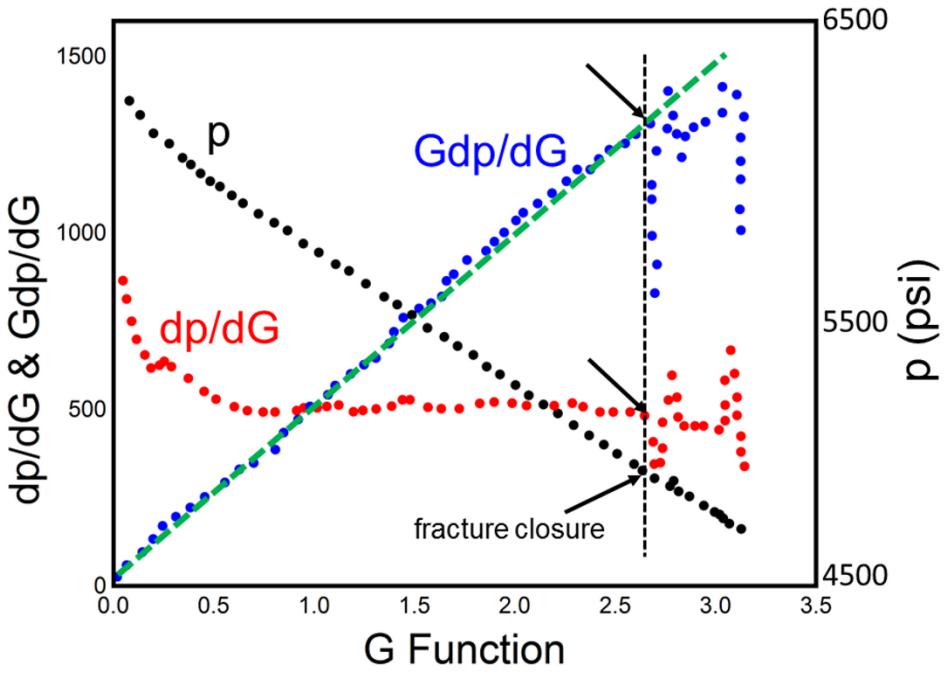

Figure 1.4—A set of field data digitized from Barree (1998).

The pre-closure analysis presented by Nolte (1979) is based on some ideal assumptions, including constant fracture height, Carter's leak-off model, constant fracture area during closure, and fracturing fluid is incompressible. Such assumptions might not be satisfied in field cases, which results in non-linear behaviors in the curves of *p* and *Gdp/dG* vs. *G* time. Some of the factors that contribute to such non-linear behaviors have been investigated, including wellbore storage, tip extension, pressure dependent leak-off, and fracture height recession (Warpinski 1985; Economides and Nolte 2000; McClure et al. 2016).

1.1.2 After-Closure Analysis

Gu et al. (1993) estimated the formation permeability based on the pseudo-radial flow regime, in which the asymptotic behavior of pressure is inversely proportional to the permeability of the formation. Using line source simulation, Abousleiman et al.

(1994) presented the theory to analyze the after-closure pressure decline both in the pseudo-radial flow regime and the pseudo-linear flow regime, in which the linear flow from the hydraulic fracture to the formation still dominates. The method as described estimates both the hydraulic fracture length and permeability. Figure 1.5 illustrates the 1/2 slope in the pseudo-linear flow regime and -1 slope in the pseudo-radial flow regime, based on which the formation permeability and hydraulic fracture length were estimated (Abousleiman et al. 1994). Analysis of the pseudo-linear flow region was later extended to investigate spurt loss and closure time (Nolte et al. 1997). Soliman et al. (2005) present a technique to determine the after-closure flow regimes, including pseudo-radial flow regime, bilinear flow regime (accounting for residual conductivity of the hydraulic fracture), and pseudo-linear flow regime, which allows estimating the formation permeability, reservoir pressure, and fracture properties. The after-closure analysis technique was also shown to be an economical alternative for reservoir characterization involving formations with both relatively high permeability (Talley et al. 1999; Chipperfield and Britt 2000) and low permeability (Britt et al. 2004).

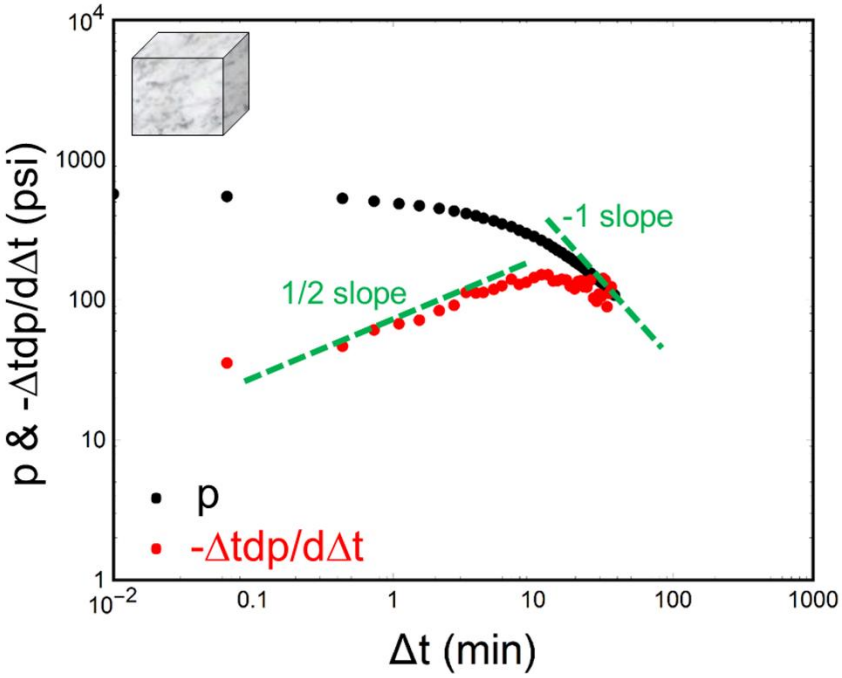

Figure 1.5—A set of field data digitized from Abousleiman et al. (1994). A single porosity rock formation.

The after-closure pressure decline analyses mentioned previously apply to single-porosity formations. However, extension of their application from single-porosity formations to dual-porosity or naturally fractured formations is necessary. The fluid leakoff rate, for instance, could be much larger compared to non-fractured formations, and dominated by natural fractures. This is contrary to cases of non-fractured formations, where the leakoff is controlled by the permeability of rock matrix, injected fluid rheology, and fracture geometry (Penny et al. 1985). To date, only a few methods are available to assess the after-closure analysis of naturally fractured formations. Nolte and Smith (1981) presented a method to identify natural fractures by a log-log plot of net pressure versus treating time. It is shown that the excessive leakoff to the natural fractures will be reflected on the net pressure response curves, where they tend to flatten. Houze et al. (1988) presented the pressure transient response when a well is

producing through a vertical fracture with infinite conductivity in a naturally fractured reservoir. Ozkan and Raghavan (1991) provided an extensive library of point source and line source solutions in a naturally fractured reservoir, accounting for various reservoir geometry and boundary conditions. Chipperfield (2006) presented an analytical instantaneous line source solution for a dual-porosity reservoir, using the analytical continuous line source solution given by Aguilera (1987). The after-closure pressure versus the inverse squared Nolte time was plotted in a log-log scale [Nolte Diagnostic Plot (NDP)] to identify natural fractures and estimate reservoir permeability, storativity ratio, and inter-porosity flow coefficient. The after-closure pressure analysis was also presented in a step-by-step procedure by Uribe et al. (2007; 2008). More recently, Soliman et al. (2010) applied the analysis to naturally fractured formations, coalbed methane, and fractured horizontal wells. Two situations are examined—when the hydraulic fracture closes and when it stays open during the shut-in period. Case studies of the after-closure analysis for naturally fractured reservoirs can be also found in Chipperfield (2005; 2006), Uribe et al. (2007), and Soliman et al. (2010).

Figure 1.6 illustrates the shapes of pressure and pressure derivative curves for a dual-porosity dual-permeability formation. The hump in the pressure curve and the trough in the pressure derivative curve clearly indicate that the formation has dual-porosity dual-permeability properties. So far, the after-closure analysis of dual-porosity dual-permeability formations is highly dependent on the Warren and Root model. It is an idealized dual-porosity model, assuming that the secondary porosity consists of an orthogonal system of uniform fractures and that fluid can communicate

between primary and secondary porosities but cannot permeate through the primary porosity elements. It also assumes that there is only pure fracture fluid flow to the wellbore without matrix fluid flow to the wellbore.

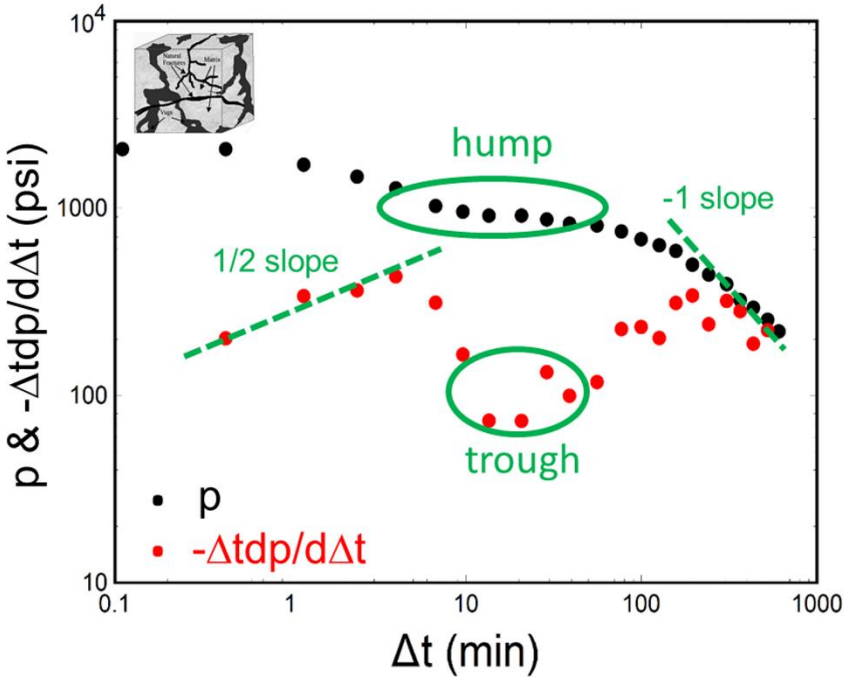

Figure 1.6—A set of field data digitized from Chipperfield (2006). A dual-porosity dual-permeability rock formation.

1.2 Introduction to Poroelasticity

1.2.1 Poroelasticity

Biot (1941) first presented the isotropic poroelastic theory describing the coupled processes of fluid flow, stress variation and rock matrix deformation in a porous medium which is fully saturated with an incompressible fluid. Later on, the theory was generalized to account for a compressible fluid and matrial anisotropy (Biot 1955; Biot and Willis 1957; Rice and Cleary 1976). The isotropic and anisotropic poroelasticity has been widely used in many areas of the oil and gas industry. To name

a few, such areas include wellbore stability analysis (Detournay and Cheng 1988; Cui et al. 1997; Abousleiman and Cui 1998; Abousleiman et al. 2000; Ekbote and Abousleiman 2005; Ekbote and Abousleiman 2006; Nguyen and Abousleiman 2010a; Tran et al. 2011), Mandel's problem (Mandel 1953; Abousleiman et al. 1996), rock failure around a hydraulic fracture (Warpinski et al. 2004; Ge and Ghassemi 2008; Ghassemi et al. 2010), wellbore strengthening (Alberty and McLean 2004; Mehrabian et al. 2015; Mehrabian and Abousleiman 2016; Mehrabian 2016), surface deformation and reservoir compaction (Geertsma 1973; Mehrabian and Abousleiman 2015b), solid cylinder, hollow cylinder and wellbore (Rice and Cleary 1976; Abousleiman and Cui 1998).

The governing equations for isotropic poroelasticity can be found in a variety of publications (Biot 1941, Biot 1955, Coussy 2004). They are revisited here and expressed explicitly in the following paragraphs.

For a homogenous and isotropic fully saturated porous medium, the constitutive equations can be expressed as follows:

$$\sigma_{ij} = \frac{E}{1+\nu}\left(\varepsilon_{ij} + \frac{\nu}{1-2\nu}\varepsilon_{kk}\delta_{ij}\right) + \alpha p \quad \text{..... (1.5)}$$

$$\zeta = -\alpha\varepsilon_{kk} + \frac{p}{M} \quad \text{..... (1.6)}$$

where σ_{ij} and ε_{ij} are the stress and strain tensors, respectively, E and ν are the Young's modulus and Poisson's ratio, α is the effective pore pressure, δ_{ij} is the Kronecker delta function, ζ is the fluid content variation, M is the effective coupled Biot's moduli.

Disregarding the body forces, the quasi-static equilibrium equation can be written as:

$$\frac{\partial \sigma_{ij}}{\partial x_j} = 0 \quad \text{..... (1.7)}$$

The fluid continuity equation is expressed as:

$$\frac{\partial \zeta}{\partial t} + \frac{\partial q_i}{\partial x_i} = 0 \quad \text{..... (1.8)}$$

where q is the total volumetric fluid flux.

The fluid flux due to the pore pressure gradient obeys Darcy's law:

$$q_i = -\frac{k}{\mu}\frac{\partial p}{\partial x_i} \quad \text{..... (1.9)}$$

where k is the permeability, and μ is the fluid viscosity.

Under the condition of small deformations, the strain-displacement relations can be expressed as follows:

$$\varepsilon_{ij} = \frac{1}{2}\left(\frac{\partial u_i}{\partial x_j} + \frac{\partial u_j}{\partial x_i}\right) \quad \text{..... (1.10)}$$

where u_i is the i^{th} component of the displacement vector.

1.2.2 Dual-Poroelasticity

Some rocks might contain natural fractures (Slatt and Abousleiman 2011; Slatt and O'Brien 2011). Such natural fractures usually have higher permeability than the rock matrix. Moreover, open natural fractures should be softer than the matrix. Such differences between the matrix and fracture system result in the dual-porosity dual-permeability nature of rock formations. The previously discussed single poroelasticity theory might fail to explain the behaviors of such dual-porosity dual-permeability rock

formations during field operations and laboratory testing. It should be noted that organic-rich shale also has dual-porosity dual-permeability properties since the poromechnical and physical properties of the organic matter are usually significantly different from the ones of non-organic matrix (Eliyahu et al. 2015).

The original dual-porosity dual-permeability concept for fractured/fissured rocks was proposed by Barenblatt et al. (1960). The two overlapping continua, primary porosity and secondary porosity, possess their own fluid pressure fields. Warren and Root (1963) proposed an idealized dual-porosity model, assuming that the secondary porosity consists of an orthogonal system of uniform fractures and that fluid can communicate between primary and secondary porosities, but not among the primary porosity elements. Their models are based on pure flow without coupling among pore pressure, stresses and rock deformation. Later on, the coupled dual-porosity dual-permeability poroelastic model was presented, where the matrix and fracture systems are treated as two overlapping porous media that have their individual physical and poromechanical properties (Wilson and Aifantis 1982; Berryman and Wang 1995). Berryman and Pride (2002) investigated the isotropic dual-poroelastic coefficients which can be determined from the constituents' properties and make the dual-poroelastic formulation more applicable. Nguyen (2010) presented the formulations to determine the transversely isotropic dual-poroelastic coefficients. Some rocks, like naturally fractured and/or organic-rich shale (Slatt and Abousleiman 2011; Slatt and O'Brien 2011), might even have N-porosity and N-permeability properties. Recently, Mehrabian and Abousleiman (2014) derived the fully coupled N-poroelasticity

formulations and applied them to the Mandel's problem and laboratory quasi-2D compression test on shale samples (Mehrabian and Abousleiman 2015a).

Many numerical simulations have been conducted for flow analysis of fractured reservoir (Kazemi et al. (1976) for two-phase flow; Sonier et al. (1988) for three-phase flow; Zimmerman et al. (1993) for non-linear inter-porosity flow; to name a few). A numerical simulation has also been carried out by Gelet et al. (2012) for a vertical wellbore under non-isothermal conditions. Regarding analytical solutions, existing solutions include axisymmetric wellbore (Wilson and Aifantis 1982), one-dimensional consolidation (Lewallen and Wang 1998), plane-strain vertical wellbore (Li 2003), inclined wellbore (Abousleiman and Nguyen 2005; Nguyen and Abousleiman 2009; Nguyen et al. 2009), and Mandel's problem and cylindrical geometry (Nguyen and Abousleiman 2009; Nguyen and Abousleiman 2010b).

The governing equations for the dual-poroelasticity can be found in many publications (Wilson and Aifantis 1982; Berryman and Wang 1995; Berryman and Pride 2002; Abousleiman and Nguyen 2005) and are described in the following paragraphs.

The constitutive equations for a homogeneous and isotropic dual-poroelastic porous medium or naturally fractured rock formation can be written as follows:

$$\sigma_{ij} = \left(\overline{K} - \frac{2}{3}\overline{G} \right) \varepsilon \delta_{ij} + 2\overline{G}\,\varepsilon_{ij} + \left(\overline{\alpha}^{I} p^{I} + \overline{\alpha}^{II} p^{II} \right) \delta_{ij} \quad \text{.....(1.11)}$$

$$\zeta^{I} = -\overline{\alpha}^{I} \varepsilon + \frac{p^{I}}{\overline{M}^{I}} + \frac{p^{II}}{\overline{M}^{I,II}} \quad \text{..... (1.12)}$$

$$\zeta^{II} = -\overline{\alpha}^{II} \varepsilon + \frac{p^{I}}{\overline{M}^{I,II}} + \frac{p^{II}}{\overline{M}^{II}} \quad \text{..... (1.13)}$$

where the superscripts ^{I} and ^{II} refer to the porous rock matrix and the porous fractures medium, respectively, $\overline{K}$ and $\overline{G}$ are the overall bulk modulus and shear modulus, respectively, $\overline{\alpha}^{I}$ and $\overline{\alpha}^{II}$ are the effective pore pressure coefficients, p^{I} and p^{II} are the matrix and fracture pore pressure, respectively, ζ^{I} and ζ^{II} are the variation of total fluid contents, and $\overline{M}^{I}$, $\overline{M}^{II}$, and $\overline{M}^{I,II}$ are the effective coupled Biot's moduli.

The effective pore pressure coefficients and effective coupled Biot's moduli can be identified in terms of the individual constituent's properties and are shown explicitly in Berryman (2002), Nguyen and Abousleiman (2010), and Mehrabian and Abousleiman (2014).

Disregarding the body forces, the quasi-static equilibrium equation can be written as:

$$\frac{\partial \sigma_{ij}}{\partial x_j} = 0 \quad \text{..... (1.14)}$$

The mass conservation of each porous medium, accounting for the inter-porosity fluid pressure diffusivity term, can be expressed separately as follows:

$$\frac{\partial \zeta^{I}}{\partial t} = -\mathrm{v}^{I} \frac{\partial q_i^{I}}{\partial x_i} - \Gamma \quad \text{.....(1.15a)}$$

$$\frac{\partial \zeta^{II}}{\partial t} = -\mathrm{v}^{II} \frac{\partial q_i^{II}}{\partial x_i} - \Gamma \quad \text{..... (1.15b)}$$

where v^{I} and v^{II} are the bulk volume fractions and Γ is the inter-porosity fluid flux transfer.

The dual-permeability nature of fractured formations requires dual Darcy's law for the fluid flow, both in the matrix medium and fracture medium. Assuming that the

flow in each porous medium obeys Darcy's law, the separate Darcy's flow equations are expressed as follows (Barenblatt et al. 1960; Abousleiman and Nguyen 2005):

$$q_i^I = -\frac{k^I}{\mu}\frac{\partial p^I}{\partial x_i} \quad \text{.....(1.16a)}$$

$$q_i^{II} = -\frac{k^{II}}{\mu}\frac{\partial p^{II}}{\partial x_i} \quad \text{..... (1.16b)}$$

where k^I and k^{II} are the matrix and fracture permeability, respectively, and μ is the fluid viscosity.

The inter-porosity fluid flow is modeled as a pseudo-steady state flow which assumes the fluid exchange between the two overlapping porous media is directly proportional to the pressure differences. The inter-porosity fluid flux transfer is defined by Warren and Root (1963) as follows:

$$\Gamma = \lambda\left(p^{II} - p^{I}\right) \quad \text{..... (1.17)}$$

where λ is the interflow coefficient ($Pa^{-1}\cdot s^{-1}$) characterizing the fractured formation, such as matrix permeability and fracture geometry, distribution, and size.

Under the condition of small deformations, the strain-displacement relations can be expressed as follows:

$$\varepsilon_{ij} = \frac{1}{2}\left(\frac{\partial u_i}{\partial x_j} + \frac{\partial u_j}{\partial x_i}\right) \quad \text{..... (1.18)}$$

1.3 Objectives and Outline

This dissertation aims to apply the theory of poroelasticity to the after-closure analysis of naturally fractured formations. For this purpose, the line source theory (Carslaw and Jaeger 1959; Abousleiman et al. 1994) is first extended from the case of

single-porosity to the case of dual-porosity dual-permeability, accounting for both fracture and matrix fluid flow to the wellbore. In the dual-porosity dual-permeability model (Wilson and Aifantis 1982; Beskos and Aifantis 1986; Berryman 2002; Coussy 2004; Abousleiman and Nguyen 2005), the matrix and fracture systems are treated as two overlapping porous media that have different physical and poromechanical properties. Furthermore, an inter-porosity flow is considered between the two porous networks, the strength of which is assumed to be proportional to the pressure gradient between them. The newly-derived analytical solutions provide effective methods to determine both matrix and fracture permeability, hydraulic fracture length and inter-porosity flow coefficients based on the log-log plot of pressure derivative curve. Such parameters are crucial for hydraulic fracturing design. The analytical solutions are also applied to match field recorded wellbore pressure data to determine formation double poromechanical parameters such as Biot's coefficient, Skempton's coefficient and bulk modulus.

In Chapter 2, the line source theory will be used to simulate the wellbore pressure response after hydraulic fracture closure in a dual-porosity porous medium. Instead of using the conventional Warren and Root model, the dual-poroelastic model will be used, accounting for both flow in matrix and fractures. First, the instantaneouse point source solution for a single porosity formation will be extended to account for a dual-porosity dual-permeability formation. Second, the instantaneous line source solution will be derived based on the instantaneous point source solution. And consequently, continuous line source and finite interval line source solutions for a dual-porosity dual-permeability formation are derived to simulate wellbore pressure response after a

finite time of injection. The solutions are analyzed mathematically and the slopes of 1/2 and -1, which indicate pseudo-linear flow and pseudo-radial flow, respectively, in the log-log plots of both matrix and fracture pressure derivative curves are discussed. A slope of -1/2 is discovered during the transient period from pseudo-linear flow to pseudo-radial flow. It is proved mathematically that this transient period is significant in formations with low permeability. The plot of pressure vs. square root time is also investigated to identify the straight-line behavior during the pseudo-linear flow regime.

In Chapter 3, a numerical example for a dual-porosity dual-permeability porous medium is presented to illustrate wellbore pressure decline after hydraulic fracture closure. Both matrix and fracture pressure decline curves are illustrated. The pseudo-linear flow regime, transient period and pseudo-radial flow regime are clearly identified in the log-log plots of the dual-pressure derivative curves. Moreover, matrix and fracture permeabilities are estimated based on the combination of 1/2 slope and -1 slope or the combination of -1/2 slope and -1 slope. Besides the matrix and fracture permeabilities, the hydraulic fracture length can be also estimated based on the -1 slope and the straight-line behavior in the plot of pressure vs. square root time. Three time markers are defined, including the upper time limit of pseudo-linear flow, lower time limit of pseudo-radial flow and the time when the dip base of pressure derivative curves occurs. Such time markers are found to be sensitive to the inter-porosity flow coefficient and can be used to estimate the inter-porosity flow coefficient. A time scale is also defined to investigate the time when the two porous media reach a state of equilibrium. This time scale is inversely proportional to the inter-porosity flow

coefficient, which quantitatively shows that larger inter-porosity flow coefficient results in shorter time for the two systems to reach a sate of equilibrium.

In Chapter 4, three case studies are presented. In Case Study 1, recorded wellbore pressure response from an Australian gas field (Chipperfield 2006) during the after-closure period is studied. The hump in the pressure curve and the dip in the pressure derivative curve are clearly identified, which indicate that the studied formation is a dual-porosity dual-permeability formation. The average permeability of the formation is estimated based on the -1 slope, i.e., the pseudo-radial flow regime. The -1/2 slope on the log-log pressure derivative curve is not clearly observed, which indicates that the formation permeability is not very low. The curve of pressure vs. square root time is also plotted to identify the straight-line behavior during the pseudo-linear flow. The newly-derived analytical solution is then used to match the field data. A good match between the two can be found. Consequently, the dual-porosity poroelastic parameters of the formation are estimated. Sensitive analysis is applied and shows that the match is sensitive to both matrix and fracture permeability, matrix bulk modulus, Skempton's coefficient and Biot's coefficient, but not sensitive to fracture bulk modulus, Skempton's coefficient or Biot's coefficient. Such sensitive analysis clearly indicates that the flow in matrix should be taken into account during the after-closure analysis, since the match is sensitive to matrix permeability and matrix poromechanical parameters. In Case Studies 2 and 3, the hump in the pressure curves is not clear. But the dip behavior in the pressure derivative curves can be clearly observed, which identify the dual-porosity dual-permeability nature of the formations. The analytical solution of the fracture pressure captures the field data to some extent, based on which

formation poromechanical parameters are estimated. Conventional well test parameters, including total compressibility, storage and hydraulic diffusivity, are revisited and the equivalent poroelastic parameters are defined. These conventional well test parameters have been defined by reservoir engineers since the 1950s, and corresponding correlations for their estimates have to date been used in the industry practice of type curve and well testing analyses. However, they have never been revisited from a poromechanical standpoint. Chapter 4 offers an in-depth review of these same parameters and characterizes them by the well-known poroelastic constants which can be measured through standard and established laboratory methods (Hart and Wang 1995; Berryman and Wang 1995) or well logging data (Abousleiman et al. 2007).

Finally, Chapter 5 provides a summary of this dissertation's findings and conclusions.

Chapter 2 : Analytical Solutions for Line Source Simulation

2.1 Line Source Simulation

In the case of a single porosity formation, Gu et al. (1993) applied the instantaneous line source simulation and studied the -1 slope in the log-log pressure derivative plot for estimation of permeability. Abousleiman et al. (1994) presented both instantaneous line source and finite line source solutions and investigated the slopes of 1/2 and -1 for estimation of permeability and hydraulic fracture length. In the case of a dual-porosity formation, line source solutions were also derived to estimate fracture permeability and inter-porosity flow coefficient, using the Warren and Root model (Houze et al. 1988; Ozkan and Raghavan 1991; Chipperfield 2006). This section will apply the line source theory to simulate wellbore pressure response after hydraulic fracture closure in a dual-porosity dual-permeability formation, using the dual-poroelastic model.

Suppose the impulse fracture test is applied to a naturally fractured formation that is bounded by two impermeable ones, as illustrated in Figure 1.1. The fracturing fluid is pumped at a rate of Q_0 for a time of t_p, and the created hydraulic fracture closes at time t_c. Assume that both the wellbore section and the created hydraulic fracture extend to the full height of the formation and the hydraulic fracture is symmetric with respect to the wellbore. Ignoring the pressure difference along the vertical direction in the created fracture and approximating the problem by a plane strain problem, this allows for 2D analysis.

Considering a horizontal plane in the formation, the wellbore is simulated as one point denoted by the origin. The after-closure wellbore pressure can be simulated by the finite interval line source solution (i.e., the pressure influence at the middle point

of a finite line source with an injection of a volume of $Q_0 t_p$ for a finite duration t_c, as shown in Figure 2.1). The length of the line source, $2L_e$, is expected to be longer than the maximum length of the hydraulic fracture, $2L$, because the injection is more concentrated near the well region, which creates an illusion of a longer line source (Abousleiman et al. 1994). At the origin, both a matrix and fracture after-closure pressure decline will be investigated.

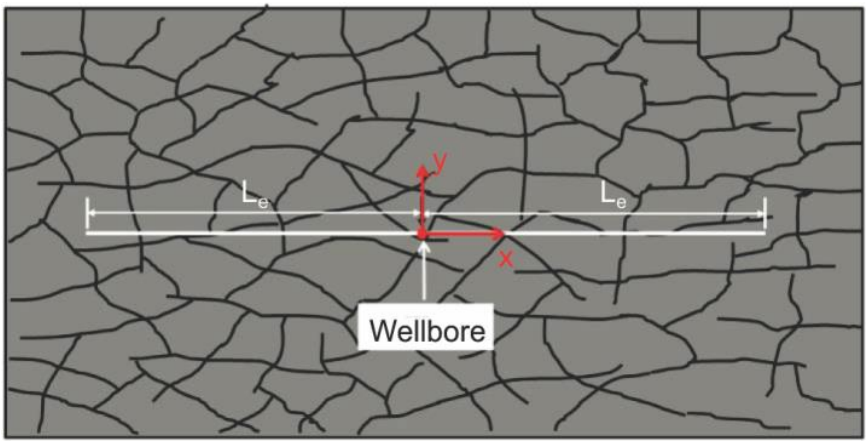

Figure 2.1—Line source simulation in a naturally fractured rock formation.

2.2 Analytical Solutions

The homogeneity and infinite extents of solution domain in this problem and fluid source-type boundary conditions caused the coupled governing equations of poroelasticity (Eqs. 1.11-1.18) to recover the pressure equations in the uncoupled form as follows (i.e., Eq. B-1 in Appendix B):

$$A\frac{\partial}{\partial t}\begin{bmatrix} p^{I} \\ p^{II} \end{bmatrix} = D\nabla^2\begin{bmatrix} p^{I} \\ p^{II} \end{bmatrix} + \Gamma\begin{bmatrix} p^{I} \\ p^{II} \end{bmatrix} \quad \text{..... (2.1)}$$

Where the coefficients matrixes A, D and Γ are expressed in Eq. A-8, A-12 and A-13, respectively.

Note that the above governing equations of the dual pressure fields have the same form as the ones given by Barenblatt et al. (1960) who presented the original dual-continuum theory and provided the dual pressure governing equations as follows:

$$A'\frac{\partial}{\partial t}\begin{bmatrix} p^{I} \\ p^{II} \end{bmatrix} = D'\nabla^{2}\begin{bmatrix} p^{I} \\ p^{II} \end{bmatrix} + \Gamma'\begin{bmatrix} p^{I} \\ p^{II} \end{bmatrix} \quad \text{..... (2.2)}$$

$$\text{where } A' = \begin{bmatrix} \phi_m C_{tm} & -\beta_{*} \\ -\beta_{**} & \phi_f C_{tf} \end{bmatrix}; D' = \begin{bmatrix} \frac{k^{I}}{\mu} & 0 \\ 0 & \frac{k^{I}}{\mu} \end{bmatrix}; \Gamma' = \frac{\alpha}{\mu}\begin{bmatrix} -1 & 1 \\ 1 & -1 \end{bmatrix} \quad \text{..... (2.3)}$$

Comparisons between Eqs. A-8, A-12 and A-13 and 2.3 show that the primary significance of poroelasticity in this specific application and solution is identified by calibrating parameters in the coefficient matrices A', D' and Γ' with poroelastic parameters in the coefficient matrices A, D and Γ, respectively. Results are shown in Table 4.4.

To obtain the solutions of a finite interval line source with an injection of a volume of $Q_0 t_p$ for a duration t_c, it is necessary to derive the solutions of instantaneous point source, instantaneous line source, and continuous line source. The steps to derive the solutions are illustrated in Figure 2.2 and are also explicitly presented as follows: (1) the pressure influence solution resulting from an instantaneous point source with a unit fluid volume injection in a plane with single porosity and single permeability (Carslaw and Jaeger 1959; Abousleiman et al. 1994) is extended to the dual-porosity dual-permeability case (matrix: $p^{I}_{\text{inst,point}}$; fracture: $p^{II}_{\text{inst,point}}$); (2) the solutions (matrix: $p^{I}_{\text{inst,line}}$; fracture: $p^{II}_{\text{inst,line}}$) resulting from an instantaneous line source with a uniform intensity along a length of $2L_e$ are obtained by integrating the former solutions along

the length; (3) the solutions (matrix: $p^{I}_{\text{cont,line}}$; fracture: $p^{II}_{\text{cont,line}}$) resulting from a continuous line source with a uniform intensity along a length of $2L_e$ and of time t are obtained by integrating the former instantaneous line source solutions with respect to time; and (4) the solutions (matrix: $p^{I}_{\text{line,w}}$; fracture: $p^{II}_{\text{line,w}}$) at the wellbore resulting from a finite interval line source with an injection of a volume of $Q_0 t_p$ for a duration t_c can be obtained as follows:

$$p^{I}_{\text{line,w}}(\Delta t) = \frac{Q_0 t_p}{2HL_e t_c}\left[p^{I}_{\text{cont,line}}(t_c + \Delta t) - p^{I}_{\text{cont,line}}(\Delta t)\right] \quad \text{(2.4)}$$

$$p^{II}_{\text{line,w}}(\Delta t) = \frac{Q_0 t_p}{2HL_e t_c}\left[p^{II}_{\text{cont,line}}(t_c + \Delta t) - p^{II}_{\text{cont,line}}(\Delta t)\right] \quad \text{(2.5)}$$

where Δt is the after-fracture-closure time, H is the fracture height, and $2L_e$ is the equivalent fracture length, which is expected to be longer than the actual maximum fracture length. The details for deriving the various source solutions are presented in Appendix A.

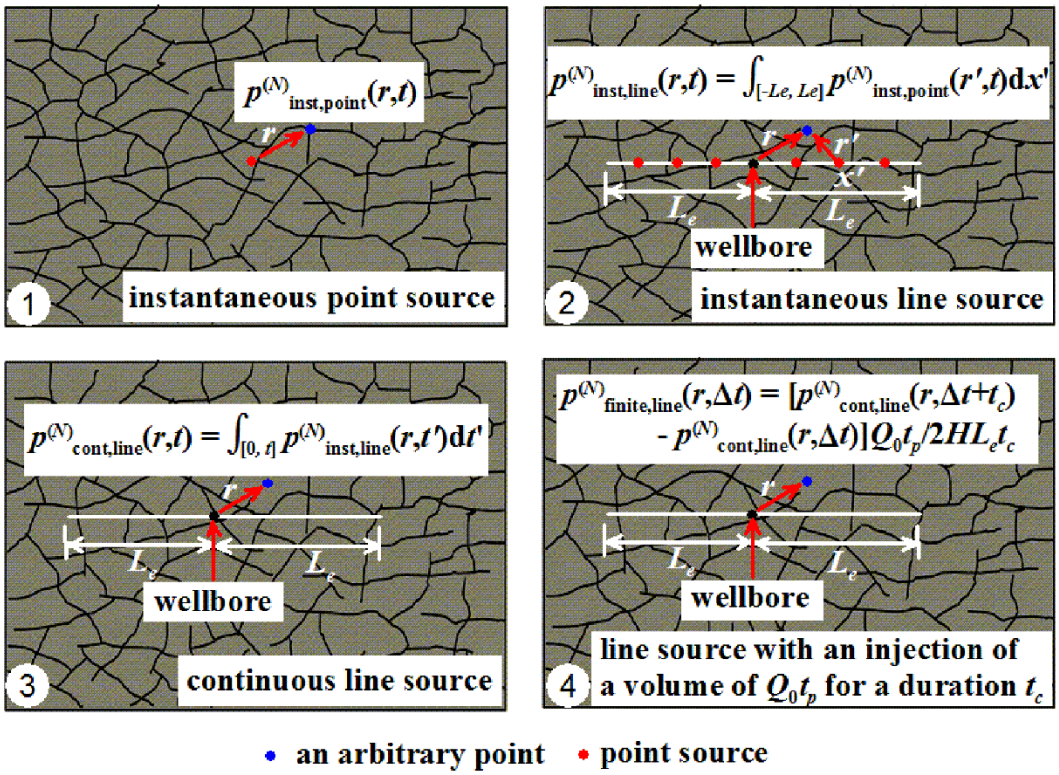

Figure 2.2—Illustration of the steps to derive the finite line source solutions, N= I, II.

Note that the dependency of the rock matrix and fracture pressures p^I and p^{II} on the rock strain is implicit in the constitutive equations of poroelasticity (See Eqs. 1.11-1.13). However, solving for these pressures via Eq. 2.1 does not directly involve the rock strain or stress. For this reason, the well-known poroelastic coupling effects such as Mandel-Cryer effect (Abousleiman et al. 1996) or Noordbergum effect (Verruijt 1969, Gambolati 1974) are not tractable with the presented solution. Conversely, this dissertation considers an infinite domain for the analysis. Together with domain homogeneity, this assumption results in the seemingly uncoupled form of the governing equations of the matrix and fracture pressures (Eq. 2.1).

Alternatively, Mehrabian and Abousleiman (2009) identified a variation of Noordbergum effect, known as dilative intake effect, as a result of the possible inhomogeneity in the poroelastic solution domain. The pore pressure buildup in the pore fluid due to an embedded point fluid sink (or conversely pressure decline in the pore space near a point fluid source) is related to contraction/dilation of the relatively compliant rock matrix surrounding a stiffer reservoir. However, again, the domain homogeneity assumption of present study does not allow for capturing such poroelastic coupling effects.

2.3 Flow Regimes Identification

The following three flow regimes will be discussed in this section: pseudo-linear flow regime, pseudo-radial flow regime, and some transient period between these two regimes. Furthermore, it will be demonstrated that the transient period is significant for low permeability rock formations.

2.3.1 Pseudo-Linear Flow Regime

In the pseudo-linear flow regime, when $\Delta t \rightarrow 0^+$, six quantities at the wellbore will be investigated. They are listed as follows: p^I , p^{II} , $-dp^I/d\Delta t$, $-dp^{II}/d\Delta t$, $-\Delta t dp^I/d\Delta t$, and $-\Delta t dp^{II}/d\Delta t$. Appendix B shows that, when $\Delta t \rightarrow 0^+$, the last four of these six quantities can be approximated by the following four quantities: $-d\bar{p}^I/d\Delta t$, $-d\bar{p}^{II}/d\Delta t$, $-\Delta t d\bar{p}^I/d\Delta t$, and $-\Delta t d\bar{p}^{II}/d\Delta t$, where overbar stands for the pressure solutions without considering inter-porosity flow between the matrix and fractures. When $\Delta t \rightarrow 0^+$, the pressures p^I and p^{II} are different from $\bar{p}^I$ and $\bar{p}^{II}$ for relatively large inter-porosity flow coefficients, but the difference might not be significant for relatively small inter-porosity flow coefficients, as shown in Figure 2.3.

Pressures p^I and p^{II} during the pseudo-linear flow regime are analyzed by approximating them by $\bar{p}^I$ and $\bar{p}^{II}$, neglecting the inter-porosity flow.

Furthermore, it is shown in Appendix B that, when $\Delta t \rightarrow 0^+$, the slope of -1/2 is expected in the log-log plots of $-d\bar{p}^I/d\Delta t$ and $-d\bar{p}^{II}/d\Delta t$ vs. Δt; the slope of 1/2 is expected in the log-log plots of $-\Delta t d\bar{p}^I/d\Delta t$ and $-\Delta t d\bar{p}^{II}/d\Delta t$ vs. Δt; and a straight-line asymptotic behavior is expected in the plots of $\bar{p}^I$ and $\bar{p}^{II}$ vs. $\Delta t^{1/2}$.

Previous work, including Fig. 4.3 in Abousleiman (1991) and Fig. 9-37 in Economides and Nolte (2000), has tried to illustrate the pseudo-linear flow from a hydraulic fracture to a single-porosity rock formation. For dual-porosity dual-permeability rock formations, Figure 2.3 illustrates the pseudo-linear flow. Because of the higher permeability of fractures, the hydraulic diffusion rate into natural fractures is greater than that into the matrix. The flow into both the matrix and natural fractures is perpendicular to the hydraulic fracture surface. Hydraulic fracture length contributes to the pressure response at the wellbore and can be estimated based on this flow period.

During the test, the injection is more concentrated near the well region (Abousleiman et al. 1994). Considering the conductivity of the created hydraulic fracture, Cinco-Ley et al. (1989) showed the non-uniform distribution of the fluid flux into the formation along the hydraulic fracture during the pseudo-linear flow. Because of the non-uniform flux distribution which is different from the linear flow, (Cinco-Ley et al. 1989) proposed the name of pseudo-linear flow.

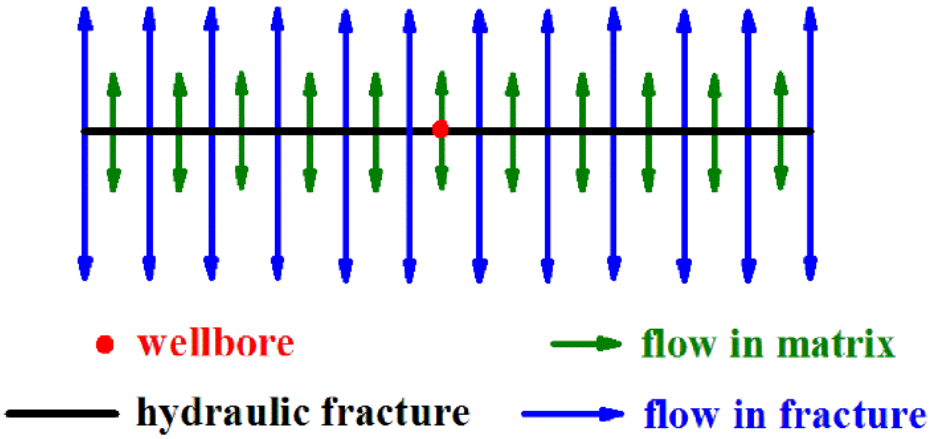

Figure 2.3—Illustration of pseudo-linear flow in a naturally fractured formation.

2.3.2 Pseudo-Radial Flow Regime

In the numerical example section, it will be shown that, when $\Delta t \to \infty$, both the matrix and fracture pore pressures at the wellbore have the following asymptotic behavior:

$$p(\Delta t) \approx \frac{Q_0 t_p \mu}{4\pi(\mathrm{v}^I k^I + \mathrm{v}^{II} k^{II})H} \frac{1}{\Delta t} \quad \text{..... (2.6)}$$

Eq. 2.6 indicates that, when $\Delta t \to \infty$, a slope of -1 is expected in the log-log plots of p^I, p^{II}, $-\Delta t dp^I / d\Delta t$, and $-\Delta t dp^{II} / d\Delta t$ vs. Δt, and a slope of -2 is expected in the log-log plots of $-dp^I / d\Delta t$ and $-dp^{II} / d\Delta t$ vs. Δt.

Comparing Eq. 2.6 with Eq. 15 in Abousleiman et al. (1994) for a single-porosity case

$$p(\Delta t) \approx \frac{Q_0 t_p \mu}{4\pi k H} \frac{1}{\Delta t} \text{ as } \Delta t \to \infty \quad \text{..... (2.7)}$$

the average permeability for a dual-porosity dual-permeability system can be defined by

$$k_{avg} = \mathrm{v}^I k^I + \mathrm{v}^{II} k^{II} \quad \text{..... (2.8)}$$

In the case of single porosity, Fig. 4.2 in Abousleiman (1991) and Fig. 9-37 in Economides and Nolte (2000) illustrate the pseudo-radial flow, which is not affected by the hydraulic fracture geometry but instead is governed by reservoir mobility and can be used to estimate reservoir permeability. Based on the previous analysis, when a pseudo-radial flow period occurs in a dual-porosity dual-permeability formation, the latter behaves as an overall system with an average permeability defined by Eq. 2.8, as illustrated in Figure 2.4. Analysis of this period allows for estimating the reservoir average permeability.

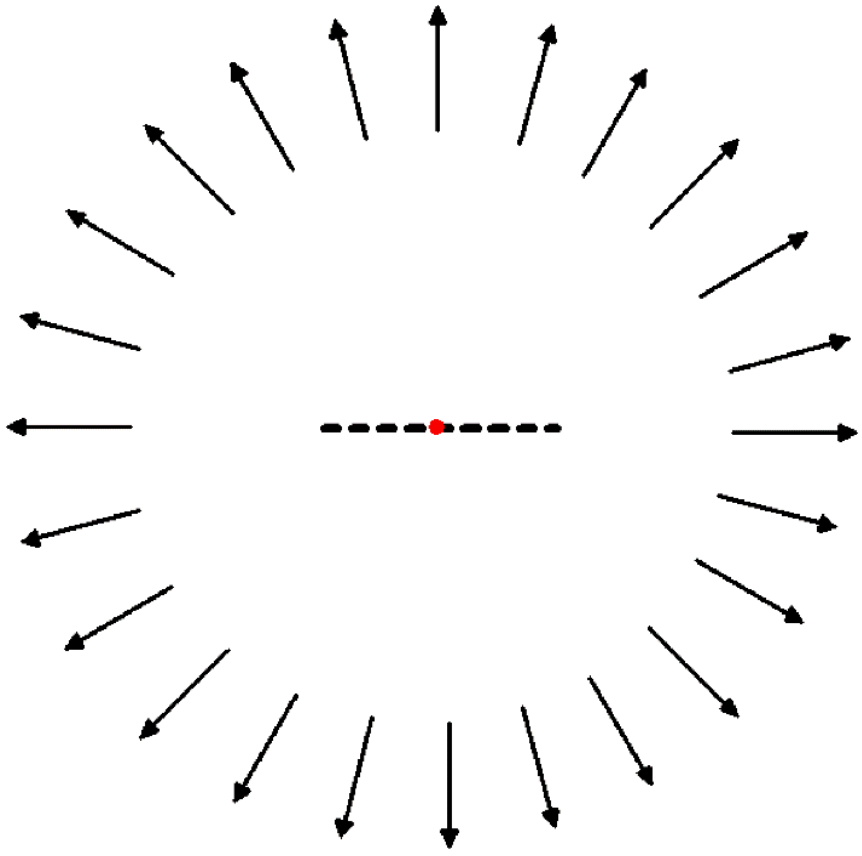

Figure 2.4—Illustration of pseudo-radial flow in a naturally fractured formation.

2.3.3 Transient Period between Pseudo-Linear and Pseudo-Radial Flow Regimes

Eqs. B-18 and B-20 indicate that, for some transient period between the pseudo-linear and pseudo-radial flow regimes, a slope of -3/2 might be able to be observed in the log-log plots of $-d\bar{p}^{I}/d\Delta t$ and $-d\bar{p}^{II}/d\Delta t$ vs. Δt and a slope of -1/2 in the log-log plots of $-\Delta t d\bar{p}^{I}/d\Delta t$ and $-\Delta t d\bar{p}^{II}/d\Delta t$ vs. Δt. Yet, to obtain Eqs. B-18 and B-20, the following equation (i.e., Eq. B-17) must be satisfied:

$$\frac{\sqrt{\bar{\lambda}^{I}}L_e e^{-\frac{\bar{\lambda}^{I}L_e^2}{4\Delta t}}}{2\sqrt{\pi}(\Delta t)^2}, \frac{\sqrt{\lambda^{II}}L_e e^{-\frac{\bar{\lambda}^{II}L_e^2}{4\Delta t}}}{2\sqrt{\pi}(\Delta t)^2} << 1;\ Erf\left(\frac{\sqrt{\bar{\lambda}^{I}}L_e}{2\sqrt{\Delta t}}\right), Erf\left(\frac{\sqrt{\bar{\lambda}^{II}}L_e}{2\sqrt{\Delta t}}\right) \approx 1 \quad \text{..... (2.9)}$$

To satisfy the conditions (Eq. 2.9), the two quantities ($\sqrt{\bar{\lambda}^{I}}L_e$ and $\sqrt{\bar{\lambda}^{II}}L_e$) are required to be relatively large. Yet, a short fracture is usually created in an impulse fracture test (i.e., L_e is usually relatively small). If the test is implemented in shale formations with relatively low permeability, conditions (Eq. 2.9) might be satisfied and slopes of -3/2 and -1/2 might be able to be observed. This can be supported by the following numerical example in which a shale formation with low permeability (in the range of nd) is studied and the two slopes are observed and the field case study in which the rock formation has relatively high permeability (in the range of md) and the two slopes are not clearly observed. Therefore, the two slopes of -3/2 and -1/2 might exist in unconventional reservoirs with relatively low permeability and might not exist in conventional reservoirs with relatively high permeability.

Note that the dual-poroelastic formulation reduces to two coupled diffusion equations as shown in the matrix form of Eq. 2.1. Each is associated with an apparent diffusion coefficient of the corresponding porosity network. By assuming no inter-

porosity flow, Eq. C-4 implies that $\bar{\lambda}^{I}$ and $\bar{\lambda}^{II}$ are the two eigenvalues of the matrix AD^{-1}, which indicates that $1/\bar{\lambda}^{I}$ and $1/\bar{\lambda}^{II}$ are the two eigenvalues of the matrix DA^{-1}. If degenerate the dual-poroelastic case to single poroelastic case, Eq. 2.1 would degenerate to the pressure diffusion equation, $\partial p/\partial t = c_p \nabla^2 p$, which is Eq. 5.26 in Coussy (2004).

Furthermore, the matrix DA^{-1} would degenerate to the hydraulic diffusivity coefficient for the poroelastic case,

$$c_p = \frac{k}{\mu} \frac{3BK(1-\nu)}{\alpha^2 B(1+\nu) + 3(1-\nu)(\alpha - \alpha^2 B)} \quad \text{..... (2.10)}$$

which is Eq. 5.22 in Coussy (2004). Thus, for the dual-poroelastic case, the two eigenvalues of the matrix DA^{-1}, $1/\bar{\lambda}^{I}$ and $1/\bar{\lambda}^{II}$, can be physically defined as the effective pressure diffusion coefficients in the porous rock matrix and the fracture network, respectively, while neglecting the inter-porosity flow.

Fig. 4.3 in Abousleiman (1991) illustrates the transient flow in a single-porosity formation. For a dual-porosity dual-permeability formation, Figure 2.5， Figure 2.6, and Figure 2.7 illustrate and compare the transient periods for the following three cases: $\lambda = 0$, $0 < \lambda < \infty$, and $\lambda = \infty$, respectively. The curvatures of the arrows describing flow in natural fractures are designed to be larger (i.e., “bend worse”) than the corresponding curvatures of the arrows describing flow in the matrix. This is because the fracture permeability is higher, and fracture systems tend to achieve a pseudo-radial flow regime faster than a matrix when neglecting the inter-porosity flow (i.e., $\lambda = 0$), which is supported by Figure 3.2. Furthermore, in the extreme case of no inter-porosity flow (i.e., $\lambda = 0$), the flow in the matrix and the flow in fractures behave

separately, without hydraulic communication (Figure 2.5). In the case of finite nonzero inter-porosity flow (i.e., $0 < \lambda < \infty$), the two flows have hydraulic communication and tend to behave as one overall flow in the rock formation as time progresses. The arrows representing flow in the matrix and flow in fractures tend to merge as time progresses (Figure 2.6). In the other extreme case of infinite inter-porosity flow (i.e., $\lambda = \infty$), any pressure difference between the matrix and fracture will be balanced instantaneously because of the infinite inter-porosity flow. As a result, the matrix and fractures pore pressure fields are identical. The dual-porosity dual-permeability formation behaves as one overall system during the entire after-closure period (Figure 2.7). These analyses are also numerically supported by Figure 3.2.

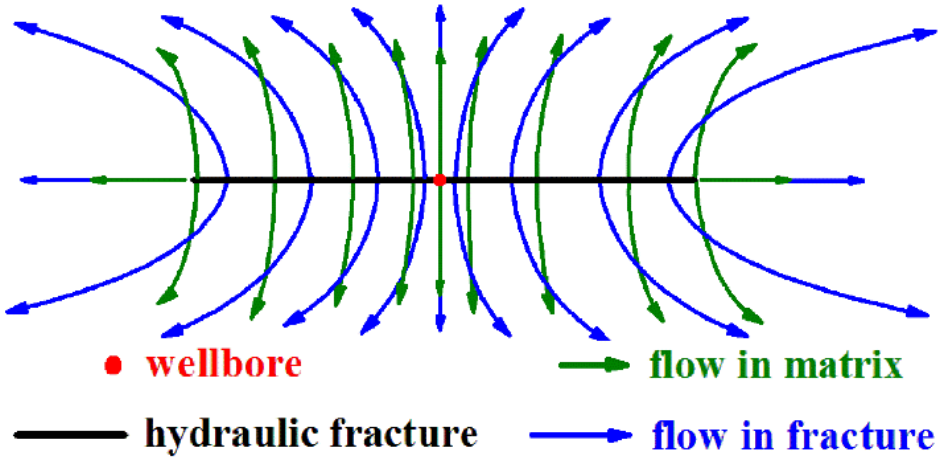

Figure 2.5—Illustration of transient period between pseudo-linear and pseudo-radial flow regimes, λ = 0. The flow in matrix is separated from the flow in fracture.

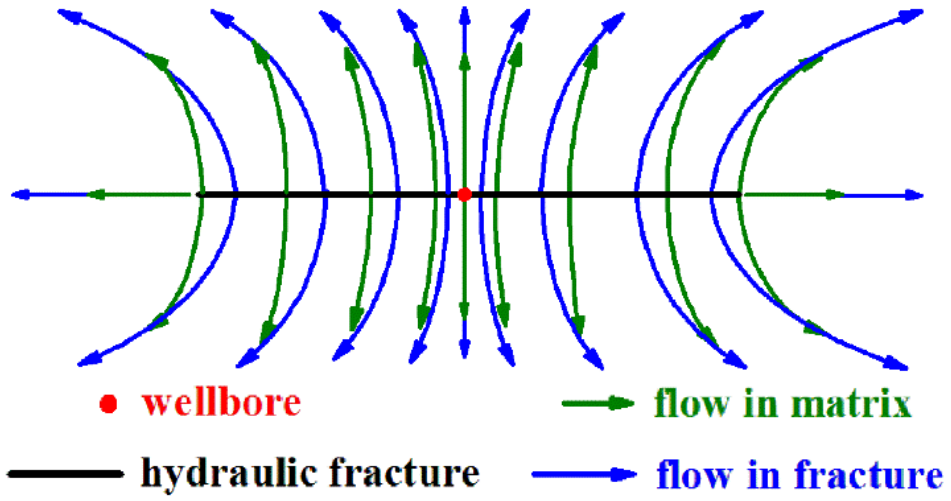

Figure 2.6—Illustration of transient period between pseudo-linear and pseudo-radial flow regimes, $0 < \lambda < \infty$. Matrix and fracture tend to reach a state of equilibrium as time proceeds.

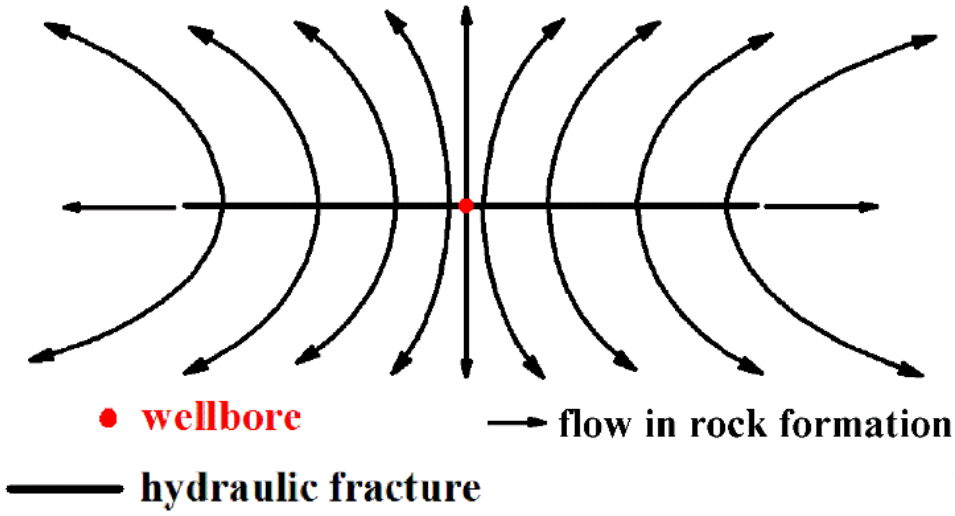

Figure 2.7—Illustration of transient period between pseudo-linear and pseudo-radial flow regimes, $\lambda = \infty$. Matrix and fracture behave as one average system.

Based on the previous analysis, one can imagine the influence of the inter-porosity flow coefficient on the flow behavior of the transient period. When the inter-porosity

flow coefficient becomes larger, the matrix and fracture pore pressures should converge faster and the arrows representing the two flows should also merge faster, which can be numerically supported by Figure 3.3. Note that the hydraulic fracture length also contributes to the pressure response at the wellbore during the transient period.

In a single-porosity formation, a similar analysis can be easily derived and obtained following the same steps, part of which can be found in previous published work, e.g., the analysis of -1 slope in the pseudo-radial flow regime can be found in Gu et al. (1993) and Abousleiman et al. (1994), and the analysis of 1/2 slope in the pseudo-linear flow regime can be found in Abousleiman et al. (1994). For comparison, the after-closure analysis for both a single-porosity formation and naturally fractured formation is summarized in Tables 2.1 through 2.3. The flow regimes and the corresponding slope behavior are summarized in Table 2.4.

Table 2.1—Log(-Δtdp/dΔt) vs. Log(Δt).

Flow Regime	Single Porosity	Dual Porosity
Pseudo-linear 1/2 slope	$-\Delta t\dfrac{dp(\Delta t)}{d\Delta t} \approx \dfrac{Q_0 t_p \mu\sqrt{c_p}}{4\sqrt{\pi}kHL_e t_c}\sqrt{\Delta t}$	$-\Delta t\dfrac{d\bar{p}^{I}_{\text{line,w}}(\Delta t)}{d\Delta t} \approx \dfrac{Q_0 t_p\left(\bar{n}^{I}_{11}\bar{C}^{I}\sqrt{\bar{\lambda}^{I}}+\bar{n}^{II}_{12}\bar{C}^{II}\sqrt{\bar{\lambda}^{II}}\right)}{4\sqrt{\pi}HL_e t_c}\sqrt{\Delta t}$ $-\Delta t\dfrac{d\bar{p}^{II}_{\text{line,w}}(\Delta t)}{d\Delta t} \approx \dfrac{Q_0 t_p\left(\bar{n}^{I}_{21}\bar{C}^{I}\sqrt{\bar{\lambda}^{I}}+\bar{n}^{II}_{22}\bar{C}^{II}\sqrt{\bar{\lambda}^{II}}\right)}{4\sqrt{\pi}HL_e t_c}\sqrt{\Delta t}$

Transient period -1/2 slope	$-\Delta t\frac{dp(\Delta t)}{d\Delta t} \approx \frac{Q_0 t_p \mu\sqrt{c_p}}{8\sqrt{\pi}kHL_e}\frac{1}{\sqrt{\Delta t}}$	$-\Delta t\frac{dp^I_{\text{line,w}}(\Delta t)}{d\Delta t} \approx \frac{Q_0 t_p\left(\bar{n}^I_{11}\bar{C}^I\sqrt{\bar{\lambda}^I}+\bar{n}^{II}_{12}\bar{C}^{II}\sqrt{\bar{\lambda}^{II}}\right)}{8\sqrt{\pi}HL_e}\frac{1}{\sqrt{\Delta t}}$ $-\Delta t\frac{dp^{II}_{\text{line,w}}(\Delta t)}{d\Delta t} \approx \frac{Q_0 t_p\left(\bar{n}^I_{21}\bar{C}^I\sqrt{\bar{\lambda}^I}+\bar{n}^{II}_{22}\bar{C}^{II}\sqrt{\bar{\lambda}^{II}}\right)}{8\sqrt{\pi}HL_e}\frac{1}{\sqrt{\Delta t}}$
Pseudo-radial -1 slope	$-\Delta t\frac{dp(\Delta t)}{d\Delta t} \approx \frac{Q_0 t_p \mu}{4\pi kH}\frac{1}{\Delta t}$	$-\Delta t\frac{dp(\Delta t)}{d\Delta t} \approx \frac{Q_0 t_p \mu}{4\pi(\mathrm{v}^I k^I+\mathrm{v}^{II}k^{II})H}\frac{1}{\Delta t}$

Where $c_p = \frac{k}{\mu}\frac{3BK(1-v)}{\alpha^2 B(1+v)+3(1-v)(\alpha-\alpha^2 B)}$ is the hydraulic diffusivity for the poroelastic case, which is Eq. 5.22 in Coussy (2004).

Table 2.2—Log(-dp/dΔt) vs. Log(Δt)

Flow Regime	Single Porosity	Dual Porosity
Pseudo-linear -1/2 slope	$-\frac{dp(\Delta t)}{d\Delta t} \approx \frac{Q_0 t_p \mu\sqrt{c_p}}{4\sqrt{\pi}kHL_e t_c}\frac{1}{\sqrt{\Delta t}}$	$-\frac{d\bar{p}^I_{\text{line,w}}(\Delta t)}{d\Delta t} \approx \frac{Q_0 t_p\left(\bar{n}^I_{11}\bar{C}^I\sqrt{\bar{\lambda}^I}+\bar{n}^{II}_{12}\bar{C}^{II}\sqrt{\bar{\lambda}^{II}}\right)}{4\sqrt{\pi}HL_e t_c}\frac{1}{\sqrt{\Delta t}}$ $-\frac{d\bar{p}^{II}_{\text{line,w}}(\Delta t)}{d\Delta t} \approx \frac{Q_0 t_p\left(\bar{n}^I_{21}\bar{C}^I\sqrt{\bar{\lambda}^I}+\bar{n}^{II}_{22}\bar{C}^{II}\sqrt{\bar{\lambda}^{II}}\right)}{4\sqrt{\pi}HL_e t_c}\frac{1}{\sqrt{\Delta t}}$

Transient -period -3/2 slope	$-\frac{dp(\Delta t)}{d\Delta t} \approx \frac{Q_0 t_p \mu\sqrt{c_p}}{8\sqrt{\pi}kHL_e}\frac{1}{(\Delta t)^{3/2}}$	$-\frac{dp^I_{\text{line,w}}(\Delta t)}{d\Delta t} \approx \frac{Q_0 t_p\left(\bar{n}^I_{11}\bar{C}^I\sqrt{\bar{\lambda}^I}+\bar{n}^{II}_{12}\bar{C}^{II}\sqrt{\bar{\lambda}^{II}}\right)}{8\sqrt{\pi}HL_e}\frac{1}{(\Delta t)^{3/2}}$ $-\frac{dp^{II}_{\text{line,w}}(\Delta t)}{d\Delta t} \approx \frac{Q_0 t_p\left(\bar{n}^I_{21}\bar{C}^I\sqrt{\bar{\lambda}^I}+\bar{n}^{II}_{22}\bar{C}^{II}\sqrt{\bar{\lambda}^{II}}\right)}{8\sqrt{\pi}HL_e}\frac{1}{(\Delta t)^{3/2}}$
Pseudo- radial -2 slope	$-\frac{dp(\Delta t)}{d\Delta t} \approx \frac{Q_0 t_p \mu}{4\pi kH}\frac{1}{(\Delta t)^2}$	$-\frac{dp(\Delta t)}{d\Delta t} \approx \frac{Q_0 t_p \mu}{4\pi(\mathrm{v}^I k^I+\mathrm{v}^{II}k^{II})H}\frac{1}{(\Delta t)^2}$

Table 2.3—p(Δt) vs. $(\Delta t)^{1/2}$

Flow Regime	Single Porosity	Dual Porosity
Pseudo- linear straight line	$p(\Delta t) \approx \frac{Q_0 t_p \mu}{4\pi kHt_c}\left[\frac{2\sqrt{\pi c_p t_c}}{L_e}Erf\left(\frac{L_e}{2\sqrt{c_p t_c}}\right)+E_1\left(\frac{L_e^2}{4c_p t_c}\right)-\frac{2\sqrt{\pi c_p}}{L_e}\sqrt{\Delta t}\right]$	$\bar{p}^I_{\text{line,w}}(\Delta t) \approx \frac{Q_0 t_p \bar{n}^I_{11}\bar{C}^I\bar{\lambda}^I}{4\pi Ht_c}\left[\frac{2\sqrt{\pi t_c}}{\sqrt{\bar{\lambda}^I}L_e}Erf\left(\frac{\sqrt{\bar{\lambda}^I}L_e}{2\sqrt{t_c}}\right)+E_1\left(\frac{\bar{\lambda}^I L_e^2}{4t_c}\right)\right]+\frac{Q_0 t_p \bar{n}^{II}_{12}\bar{C}^{II}\bar{\lambda}^{II}}{4\pi Ht_c}\left[\frac{2\sqrt{\pi t_c}}{\sqrt{\bar{\lambda}^{II}}L_e}Erf\left(\frac{\sqrt{\bar{\lambda}^{II}}L_e}{2\sqrt{t_c}}\right)+E_1\left(\frac{\bar{\lambda}^{II}L_e^2}{4t_c}\right)\right]-\frac{Q_0 t_p\left(\bar{n}^I_{11}\bar{C}^I\sqrt{\bar{\lambda}^I}+\bar{n}^{II}_{12}\bar{C}^{II}\sqrt{\bar{\lambda}^{II}}\right)}{2\sqrt{\pi}HL_e t_c}\sqrt{\Delta t}$

		$\bar{p}^{II}_{\text{line,w}}(\Delta t) \approx$ $\frac{Q_0 t_p \bar{n}^I_{21} \bar{C}^I \bar{\lambda}^I}{4\pi H t_c}\left[\frac{2\sqrt{\pi t_c}}{\sqrt{\bar{\lambda}^I} L_e} Erf\left(\frac{\sqrt{\bar{\lambda}^I} L_e}{2\sqrt{t_c}}\right) + E_1\left(\frac{\bar{\lambda}^I L_e^2}{4t_c}\right)\right]$ $+\frac{Q_0 t_p \bar{n}^{II}_{22} \bar{C}^{II} \bar{\lambda}^{II}}{4\pi H t_c}\left[\frac{2\sqrt{\pi t_c}}{\sqrt{\bar{\lambda}^{II}} L_e} Erf\left(\frac{\sqrt{\bar{\lambda}^{II}} L_e}{2\sqrt{t_c}}\right) + E_1\left(\frac{\bar{\lambda}^{II} L_e^2}{4t_c}\right)\right]$ $-\frac{Q_0 t_p\left(\bar{n}^I_{21} \bar{C}^I \sqrt{\bar{\lambda}^I} + \bar{n}^{II}_{22} \bar{C}^{II} \sqrt{\bar{\lambda}^{II}}\right)}{2\sqrt{\pi} H L_e t_c} \sqrt{\Delta t}$

Table 2.4—Flow regimes and the corresponding slopes.

Plots	Pseudo-Linear	Transient Period (Significant for low permeability formations)	Pseudo-Radial
$\log(-\Delta t dp/\Delta t)$ vs. $\log \Delta t$	1/2	-1/2	-1
$\log(-dp/\Delta t)$ vs. $\log \Delta t$	-1/2	-3/2	-2
p vs. $\sqrt{\Delta t}$	Straight Line		

2.4 Summary

In this section, the line source theory is applied to simulate the wellbore pressure response after hydraulic fracture closure in a dual-porosity formation, using the dual-poroelastic model. The instantaneous point source solution for a single porosity formation is extended to account for a dual-porosity dual-permeability formation. The instantaneous point source solution is then used to derive the instantaneous line source solution, and consequently, continuous line source and finite interval line source

solutions for a dual-porosity dual-permeability formation. The slopes of 1/2 and -1, which indicate pseudo-linear flow and pseudo-radial flow, respectively, in the log-log plots of both matrix and fracture pressure derivative curves are discussed. Furthermore, a slope of -1/2 is discovered during the transient period from pseudo-linear flow to pseudo-radial flow. It is proved that this transient period is significant in formations with low permeability. The plot of pressure vs. square root time is also investigated to identify the straight-line behavior during the pseudo-linear flow regime.

Chapter 3 : Hydraulic Fracture After-Closure Analysis

3.1 After-Closure Dual-Pressure Decline Curves

In this section, a numerical example is studied to illustrate dual-pressure decline curves and the corresponding flow regimes during the after-closure phase of hydraulic fracturing in a dual-porosity dual-permeability porous medium. The rock parameters in Table 3.1 are selected to mimic the Woodford shale in Abousleiman et al. (2013). For the natural fractures system, an amount of methods to estimate poroelastic parameters were proposed by Cook (1992), based on the individual fracture characteristics, orientation and spacing. In general, if natural fractures are open, their permeability is higher than the matrix. Moreover, open natural fractures should be softer than the matrix. The fracture bulk modulus is selected 50 times smaller than the matrix in this example.

Table 3.1—Selected rock parameters for simulation.

Parameters	K (GPa)	ν	B	α	k (nd)	μ (cp)	v (%)	λ (1/MPa/D)
Matrix (I)	4.8	0.3	0.56	0.88	45	1	99	1×10^{-5}
Fracture (II)	4.8/50	0.3	0.96	0.9	1×10^{5}	1	1	

The hydraulic treatment simulation data used are as follows: $Q_0 = 0.008$ m^3/s, $t_p = 6$ min, $t_c = 8$ min, $H = 10$ m, $L_e = 25$ m.

Figure 3.1 illustrates the after-closure flow regimes, including the pseudo-linear flow regime, the pseudo-radial flow regime, and the transient period between these two regimes. Both matrix and fracture pressure responses together with the pressure derivatives at the wellbore are plotted. The slopes 1/2, -1/2, and -1 can be clearly identified in the pressure derivative curves.

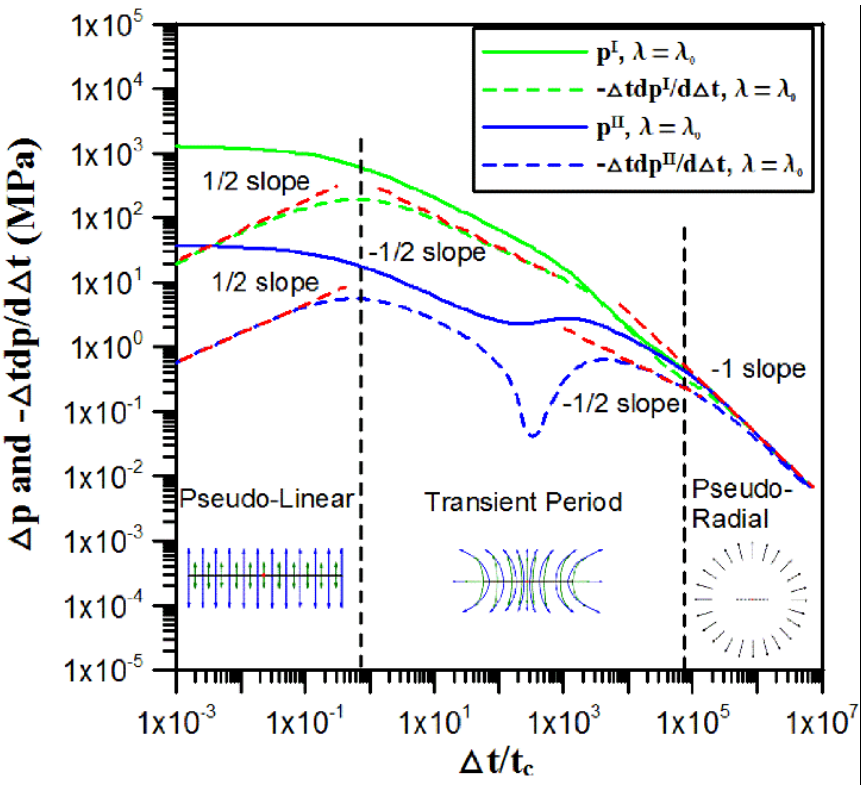

Figure 3.1—Illustration of after-closure flow regimes. The three flow regimes and their corresponding slopes are clearly identified in the dual pressure derivative curves.

Figure 3.2 shows the matrix and fracture after-closure pressure responses at the wellbore for three different inter-porosity flow coefficients—λ = 0, λ = 1 × 10^{-5}/MPa/D, and $\lambda = \infty$—together with a straight line, which is defined by

$$\log p = \log \frac{Q_0 t_p \mu}{4\pi(\mathrm{v}^I k^I + \mathrm{v}^{II} k^{II}) H t_c} - \log \frac{\Delta t}{t_c} \quad \text{..... (3.1)}$$

It can be observed that, in the case of no inter-porosity flow (i.e., λ = 0), when $\Delta t \to \infty$, the matrix and fracture behave as two separate systems. Yet, in the case of finite nonzero inter-porosity flow (i.e., λ = 1 × 10^{-5}/MPa/D), when $\Delta t \to \infty$, the matrix and fracture pore pressure and pressure derivative curves converge to the straight line with a slope of -1. This means the naturally fractured formation behaves as an overall

system, with an average permeability of $v^I k^I + v^{II} k^{II}$ when it reaches the pseudo-radial flow regime. In the case of infinite inter-porosity flow (i.e., $\lambda = \infty$), matrix and fracture pore pressures are identical and the naturally fractured formation behaves as one overall averaged system during the entire after-closure period.

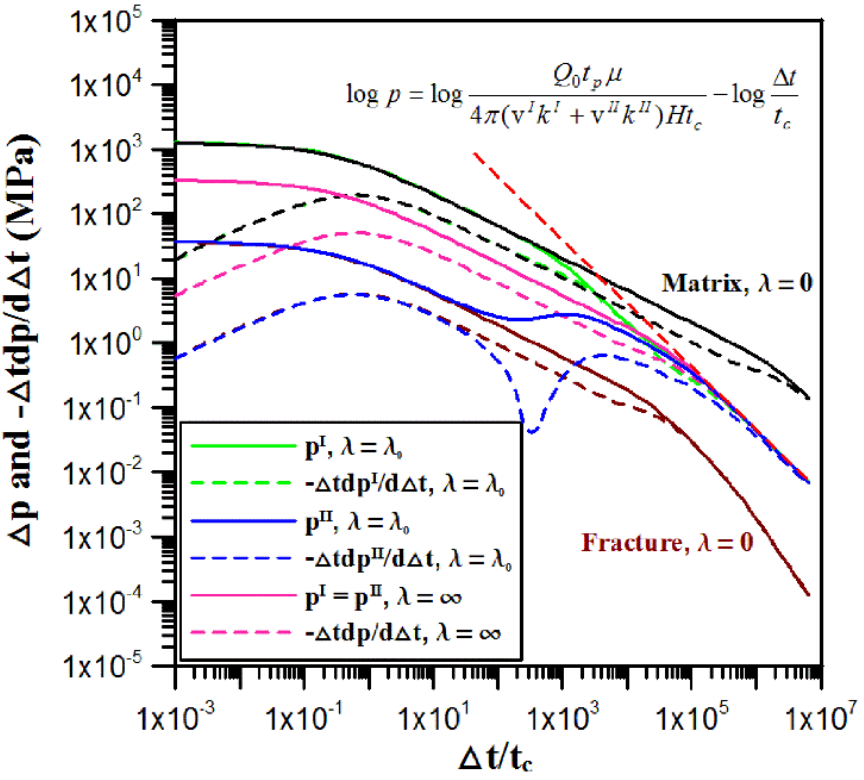

Figure 3.2—Evolution of Δp and –Δtdp/dΔt at the wellbore, $\lambda_0 = 1 \times 10^{-5}$/MPa/D. Matrix and fracture eventually reach a state of equilibrium for a finite inter-porosity flow coefficient.

To obtain a visualized comparison, Figure 3.3 illustrates the effects of finite inter-porosity flow coefficient λ on the matrix and fracture pore pressure responses at the wellbore. In the case of a finite nonzero value of the inter-porosity flow coefficient (i.e., $0 < \lambda < \infty$), when λ becomes larger, the matrix and fracture pore pressures converge faster.

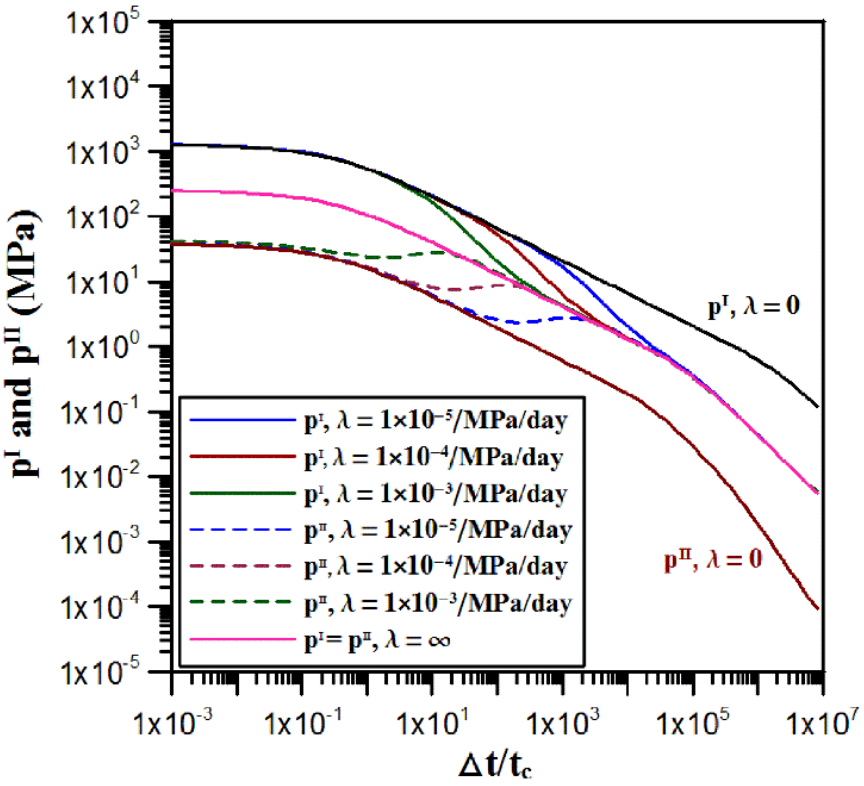

Figure 3.3—Effects of inter-porosity flow coefficient λ on p^I and p^{II} at the wellbore. Matrix and fracture reach a state of equilibrium faster for larger inter-porosity flow coefficient, which is quantitatively illustrated.

3.2 Formation Properties Estimation

The after-closure analysis will be applied on both matrix and fracture pressure decline curves to estimate formation properties.

3.2.1 Matrix Pressure Curve Analysis

The curve of matrix pore pressure derivative $-\Delta t dp^I/d\Delta t$ in Figure 3.1 shows that the slopes of 1/2, -1/2, and -1 are clearly observed in the pseudo-linear regime, transient period, and pseudo-radial regime, respectively. A combination of the 1/2 slope and -1 slope allows estimating the matrix and fracture permeability, as shown in Eq. 3.4.

Similarly, a combination of the -1/2 slope and -1 slope allows estimating the two permeabilities, as shown in Eq. 3.6. The details are presented below.

In the pseudo-radial flow regime, by reading the pressure intercept p_i (p_i = 5.0×10^4 MPa) between the $\Delta t/t_c$ = 1-axis with the straight line with slope of -1, the average permeability of the naturally fractured rock can be estimated as follows:

$$k_{avg} = \mathrm{v}^I k^I + \mathrm{v}^{II} k^{II} = \frac{Q_0 t_p \mu}{4\pi H p_i t_c} = 9.5\times10^{-19}\,\mathrm{m}^2 \quad \text{..... (3.2)}$$

Compared with the "true" value 10.4 × 10^{-19} m^2, the value provided by Eq. 3.2 shows good agreement.

In the pseudo-linear flow regime, by extending the $\Delta t/t_c$ = 1-axis to intersect the straight line with a slope of 1/2 and reading the pressure intercept p_i (p_i = 700 MPa), the following quantity can be estimated based on Eq. B-6:

$$\bar{n}_{11}^I \bar{C}^I \sqrt{\bar{\lambda}^I} + \bar{n}_{12}^{II} \bar{C}^{II} \sqrt{\bar{\lambda}^{II}} = \frac{4\sqrt{\pi} H L_e \sqrt{t_c}\, p_i}{Q_0 t_p} = 9.4\times10^{12}\ \mathrm{Pa}\sqrt{\mathrm{s}}/\mathrm{m} \quad \text{..... (3.3)}$$

A good agreement also can be obtained when comparing the value from Eq. 3.3 with the "true" value 1.1 × 10^{13} Pa·s$^{1/2}$/m. Note that the left side of Eq. 3.3 depends on the poromechanical and physical properties of the rock formation, based on Eq. C-2. Treating the left side of Eq. 3.3 as a function of k^I and k^{II}, and assuming other parameters are known, the matrix and fracture permeability can be estimated by solving Eqs. 3.2 and 3.3 with Mathematica software as follows:

k^I = 3.2 × 10^{-20} m^2 = 32 nd; k^{II} = 9.2 × 10^{-17} m^2 = 0.92 × 10^5 nd ..... (3.4)

Note that Eq. 3.3 is based on the without-inter-porosity-flow case. As previously analyzed, the quantity $-\Delta t dp^I / d\Delta t$ at $\Delta t \to 0^+$ can be approximated by $-\Delta t d\bar{p}^I / d\Delta t$, which is also shown in Figure 3.1.

The slope of -1/2 is observed in some transient period between the pseudo-linear and pseudo-radial flow regimes, as shown in Figure 3.1. Note that Figure 3.2 shows that the slope of -1/2 might be different for the cases of with-inter-porosity flow and without-inter-porosity flow. However, it is still interesting to investigate the slope of -1/2 for the case of with-inter-porosity flow approximated by the case of without-inter-porosity flow. By extending the straight line with a slope of -1/2 to intersect the $\Delta t/t_c$ = 1-axis, and reading the pressure intercept p_i (p_i = 400 MPa), the following quantity can be estimated based on Eq. B-10:

$$\bar{n}_{11}^I \bar{C}^I \sqrt{\bar{\lambda}^I} + \bar{n}_{12}^{II} \bar{C}^{II} \sqrt{\bar{\lambda}^{II}} = \frac{8\sqrt{\pi} H L_e \sqrt{t_c}\, p_i}{Q_0 t_p} = 10.7 \times 10^{12} \text{ Pa}\sqrt{\text{s}}/\text{m} \quad \text{..... (3.5)}$$

A combination of Eqs. 3.2 and 3.5 provides the estimation of matrix and fracture permeability as follows:

$k^I = 2.8 \times 10^{-20}$ m^2 = 28 nd; $k^{II} = 9.3 \times 10^{-17}$ m^2 = 0.93×10^5 nd..... (3.6)

The estimation presented in Eq. 3.6 also shows good agreement with the “true” values.

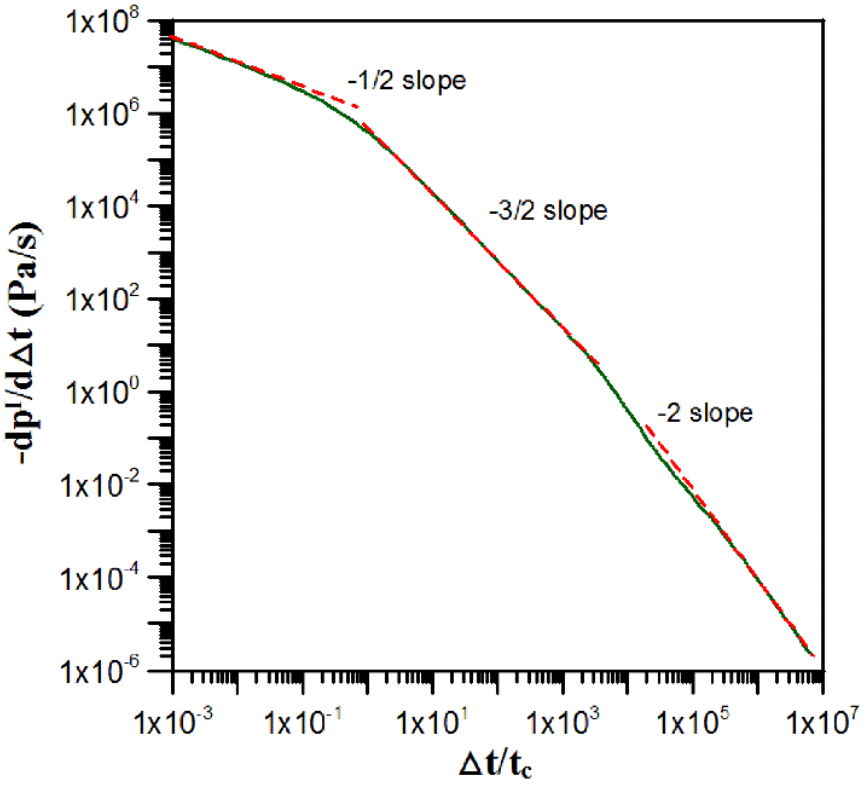

Figure 3.4—Evolution of $-dp^I/d\Delta t$ at the wellbore. -1/2, -3/2 and -2 slopes are clearly identified in the three flow regimes.

Figure 3.4 illustrates the evolution of $-dp^I/d\Delta t$ at the wellbore. The slopes of -1/2, -3/2, and -2 in Figure 3.4 correspond to the slopes of 1/2, -1/2, and -1 in Figure 3.1. Similar to the previous pressure analysis, the estimation of matrix and fracture permeability based on Figure 3.4 would have the same results as the one based on Figure 3.1, which will be omitted.

To further apply the after-closure analysis, Figure 3.5, Figure 3.6 and Figure 3.7 are investigated to estimate matrix permeability, fracture permeability, and hydraulic fracture length. Figure 3.8 and Figure 3.9 show the time markers of the dip bases in the matrix and fracture derivative curves.

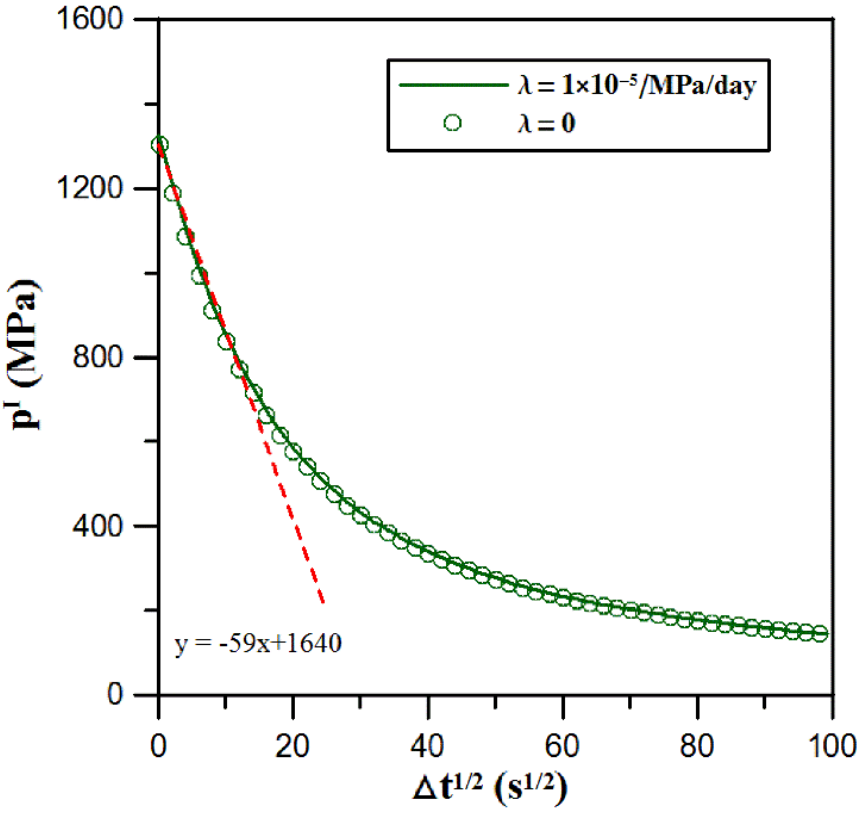

Figure 3.5—Evolution of p^I at the wellbore. The straigt-line behavior is clearly identified in the pseudo-linear flow regime.

Figure 3.5 shows a plot of p^I vs. $\Delta t^{1/2}$. The straight line asymptotic behavior can be observed at $\Delta t \rightarrow 0^+$. Approximating the straight line using Eq. B-8, the following two equations can be obtained:

$$\frac{Q_0 t_p \bar{n}_{11}^I \bar{C}^I \bar{\lambda}^I}{4\pi H t_c}\left[\frac{2\sqrt{\pi t_c}}{\sqrt{\bar{\lambda}^I}L_e}Erf\left(\frac{\sqrt{\bar{\lambda}^I}L_e}{2\sqrt{t_c}}\right)+E_1\left(\frac{\bar{\lambda}^I L_e^2}{4t_c}\right)\right]$$
$$+\frac{Q_0 t_p \bar{n}_{12}^{II} \bar{C}^{II} \bar{\lambda}^{II}}{4\pi H t_c}\left[\frac{2\sqrt{\pi t_c}}{\sqrt{\bar{\lambda}^{II}}L_e}Erf\left(\frac{\sqrt{\bar{\lambda}^{II}}L_e}{2\sqrt{t_c}}\right)+E_1\left(\frac{\bar{\lambda}^{II} L_e^2}{4t_c}\right)\right]=1640\times 10^6 \quad \text{..... (3.7)}$$

$$\frac{Q_0 t_p \left(\bar{n}_{11}^{I} \bar{C}^{I} \sqrt{\bar{\lambda}^{I}} + \bar{n}_{12}^{II} \bar{C}^{II} \sqrt{\bar{\lambda}^{II}}\right)}{2\sqrt{\pi} H L_e t_c} = 59 \times 10^{6} \quad \text{..... (3.8)}$$

Eqs. 3.2, 3.7, and 3.8 can be used to estimate k^I, k^{II}, and L_e. Using Mathematica software to solve the three equations provides an estimation of matrix permeability, fracture permeability, and equivalent fracture length as follows:

$k^I = 1.0 \times 10^{-19}$ m^2 = 100 nd; $k^{II} = 8.6 \times 10^{-17}$ m^2 = 0.86×10^5 nd; L_e = 20.0 m..... (3.9)

It can be observed that combining the slope of -1 in the curve of $-\Delta t dp^I/d\Delta t$ with the straight line asymptotic behavior in the curve of p^I allows estimating the matrix permeability, fracture permeability, and equivalent fracture length.

The above analysis is based on matrix pressure and pressure derivative curves. The following section will discuss fracture pressure and pressure derivative curves.

3.2.2 Fracture Pressure Curve Analysis

Analysis can also be applied to the curve of fracture pressure derivative $-\Delta t dp^{II}/d\Delta t$ in Figure 3.1. Eq. 3.2 can also be obtained based on the -1 slope in Figure 3.1. Similarly, by reading the pressure intersect p_i (p_i = 19 MPa) between the straight line of the 1/2 slope with the $\Delta t/t_c$ = 1-axis, according to Eq. B-7, the following equation can be obtained:

$$\bar{n}_{21}^{I} \bar{C}^{I} \sqrt{\bar{\lambda}^{I}} + \bar{n}_{22}^{II} \bar{C}^{II} \sqrt{\bar{\lambda}^{II}} = \frac{4\sqrt{\pi} H L_e \sqrt{t_c}\, p_i}{Q_0 t_p} = 2.6 \times 10^{11} \text{ Pa}\sqrt{\text{s}}/\text{m} \quad \text{..... (3.10)}$$

Solving Eqs. 3.2 and 3.10 using Mathematica software provides an estimation of the matrix and fracture permeability as follows:

$k^I = 2.7 \times 10^{-20}$ m^2 = 27 nd; $k^{II} = 9.2 \times 10^{-17}$ m^2 = 0.92×10^5 nd .....(3.11)

The estimated matrix and fracture permeabilities in Eq. 3.11 are based on the slopes of -1 and 1/2. As previously discussed, they can also be estimated based on the slopes of -1 and -1/2, which are presented below.

The slope of -1/2 is also observed in Figure 3.1. Based on Eq. B-11, the pressure intersect p_i (p_i = 9 MPa) between the straight line of the -1/2 slope with the $\Delta t/t_c$ = 1-axis can also be read to estimate the following equation:

$$\bar{n}_{21}^{I}\bar{C}^{I}\sqrt{\bar{\lambda}^{I}}+\bar{n}_{22}^{II}\bar{C}^{II}\sqrt{\bar{\lambda}^{II}}=\frac{8\sqrt{\pi}HL_e\sqrt{t_c}\,p_i}{Q_0 t_p}=2.4\times10^{11}\ \text{Pa}\sqrt{\text{s}}/\text{m} \quad \text{..... (3.12)}$$

Eqs. 3.2 and 3.12 allow estimating the matrix and fracture permeability as follows:

$k^I = 50.9 \times 10^{-20}$ m^2 = 509 nd; $k^{II} = 4.5 \times 10^{-17}$ m^2 = 0.45×10^5 nd ..... (3.13)

By comparing the estimations from Eqs. 3.11 and 3.13 with the "true" values of k^I and k^{II}, it is observed that, to estimate k^I and k^{II} based on the -1/2 slope and -1 slope, the estimation from the matrix pressure derivative curve provides more accurate results than that from the fracture pressure derivative curve, in this case. This is because the analysis of the -1/2 slope ignores the effects of inter-porosity flow. In this data set, considering the matrix pressure derivative curve, the -1/2 slope is the same for the with-inter-porosity-flow case and without-inter-porosity-flow case; however, considering the fracture pressure derivative curve, the -1/2 slope is different for the two cases, as shown in Figure 3.2.

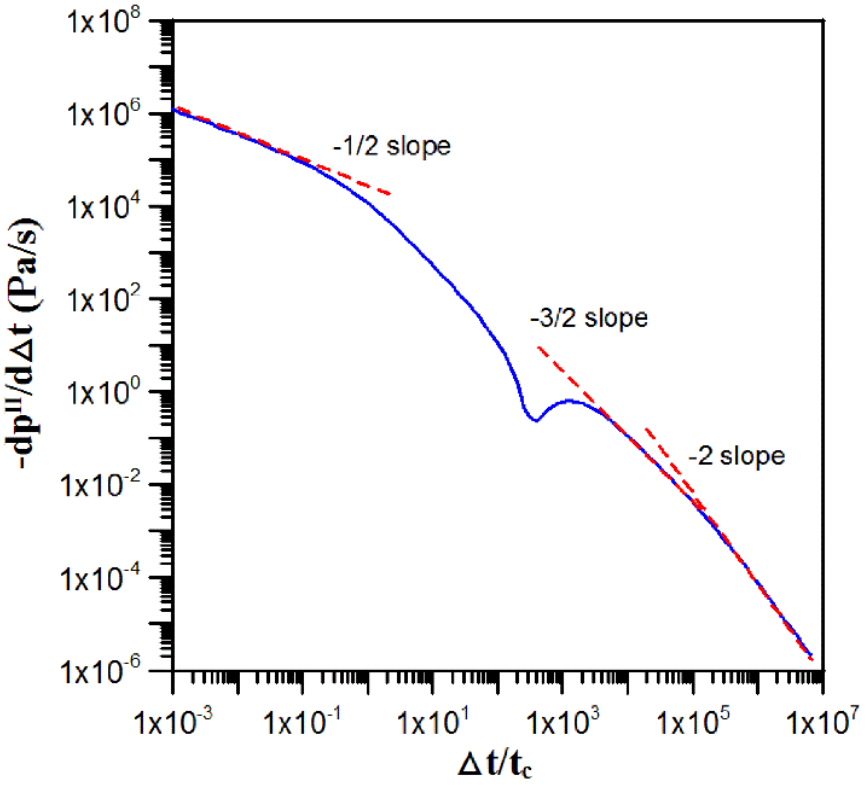

Figure 3.6—Evolution of $-dp^{II}/d\Delta t$ at the wellbore. -1/2, -3/2 and -2 slopes are clearly identified in the three flow regimes.

Figure 3.6 shows the evolution of $-dp^{II}/d\Delta t$ at the wellbore. The slopes of -1/2, -3/2, and -2 in Figure 3.6 correspond to the slopes of 1/2, -1/2, and -1 in Figure 3.1. Similarly, the estimation of matrix and fracture permeability based on Figure 3.6 would provide the same results as the one based on Figure 3.1, which will be omitted.

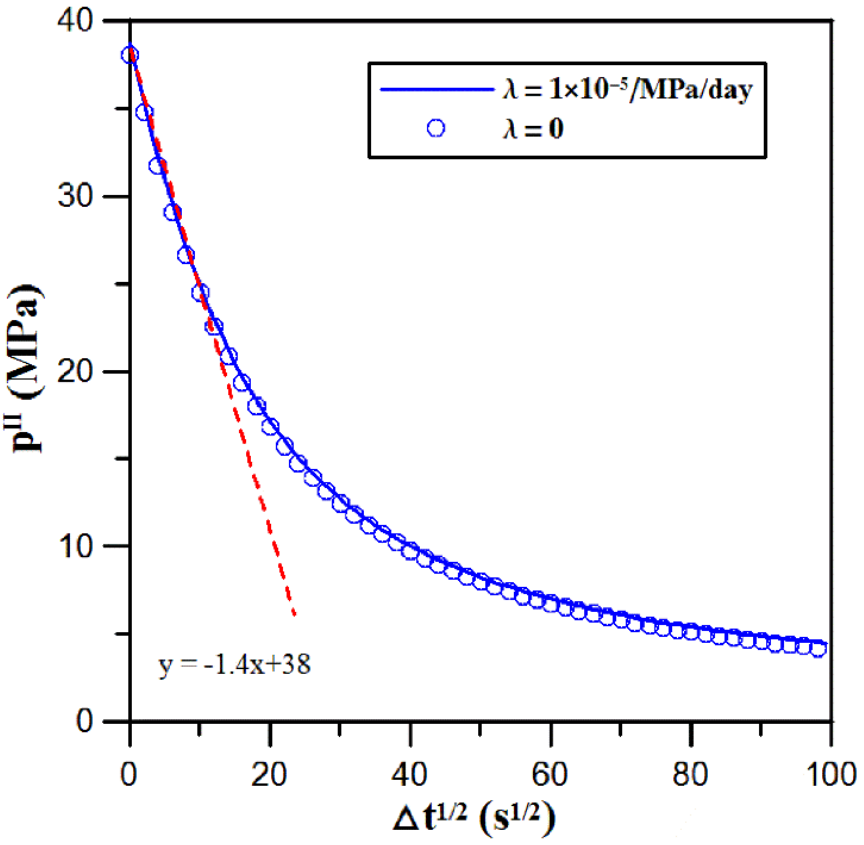

Figure 3.7—Evolution of p^{II} at the wellbore. The straigt-line behavior is clearly identified in the pseudo-linear flow regime.

Figure 3.7 shows the plot of p^{II} vs. $\Delta t^{1/2}$. The straight line asymptotic behavior is observed at $\Delta t \rightarrow 0^{+}$. Approximating the straight line using Eq. B-9 provides the following two equations:

$$\frac{Q_0 t_p \bar{n}_{21}^{I} \bar{C}^{I} \bar{\lambda}^{I}}{4\pi H t_c}\left[\frac{2\sqrt{\pi t_c}}{\sqrt{\bar{\lambda}^{I}} L_e} Erf\left(\frac{\sqrt{\bar{\lambda}^{I}} L_e}{2\sqrt{t_c}}\right) + E_1\left(\frac{\bar{\lambda}^{I} L_e^2}{4t_c}\right)\right] + \frac{Q_0 t_p \bar{n}_{22}^{II} \bar{C}^{II} \bar{\lambda}^{II}}{4\pi H t_c}\left[\frac{2\sqrt{\pi t_c}}{\sqrt{\bar{\lambda}^{II}} L_e} Erf\left(\frac{\sqrt{\bar{\lambda}^{II}} L_e}{2\sqrt{t_c}}\right) + E_1\left(\frac{\bar{\lambda}^{II} L_e^2}{4t_c}\right)\right] = 38\times 10^6 \quad \text{..... (3.14)}$$

$$\frac{Q_0 t_p \left(\bar{n}_{21}^{I} \bar{C}^{I} \sqrt{\bar{\lambda}^{I}} + \bar{n}_{22}^{II} \bar{C}^{II} \sqrt{\bar{\lambda}^{II}}\right)}{2\sqrt{\pi} H L_e t_c} = 1.4\times 10^6 \quad \text{..... (3.15)}$$

Eqs. 3.2, 3.14, and 3.15 can be combined to estimate k^I, k^{II}, and L_e as follows:

$k^I = 1.0 \times 10^{-21}$ m^2 = 1.0 nd; $k^{II} = 9.5 \times 10^{-17}$ m^2 = 0.95×10^5 nd; L_e = 25.1 m ..... (3.16)

3.2.3 Definitions of Time Markers

Figure 3.8 and Figure 3.9 present the effects of the inter-porosity flow coefficient on the matrix and fracture pressure responses at the wellbore. Its influence on the time marker of the dip base of the pressure derivative curves is interesting. Stewart and Ascharsobbi (1988) and Chipperfield (2006) present the analytical expression of the dimensionless time marker of the dip base in the fracture pressure derivative curve for the Warren and Root dual-porosity model. In the case of the dual-porosity dual-permeability model used in this chapter, the analytical expressions for the time markers of the dip bases in both matrix and fracture pressure derivative curves are shown below.

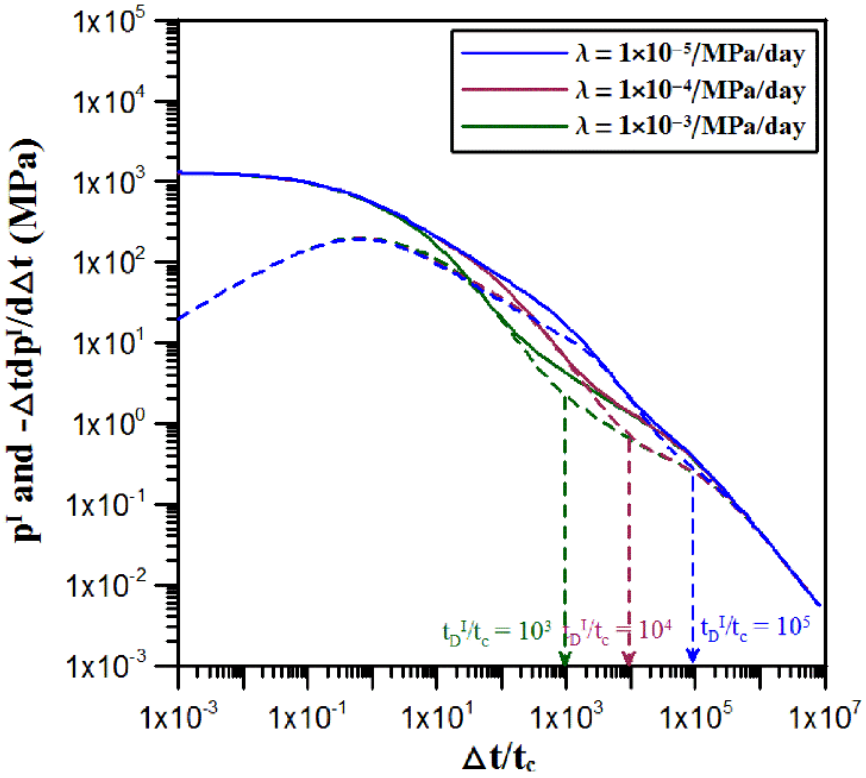

Figure 3.8—Effects of inter-porosity flow coefficient on the evolution of p^I & $-\Delta t dp^I/d\Delta t$. The time marker for the dip base is inversely proportional to λ.

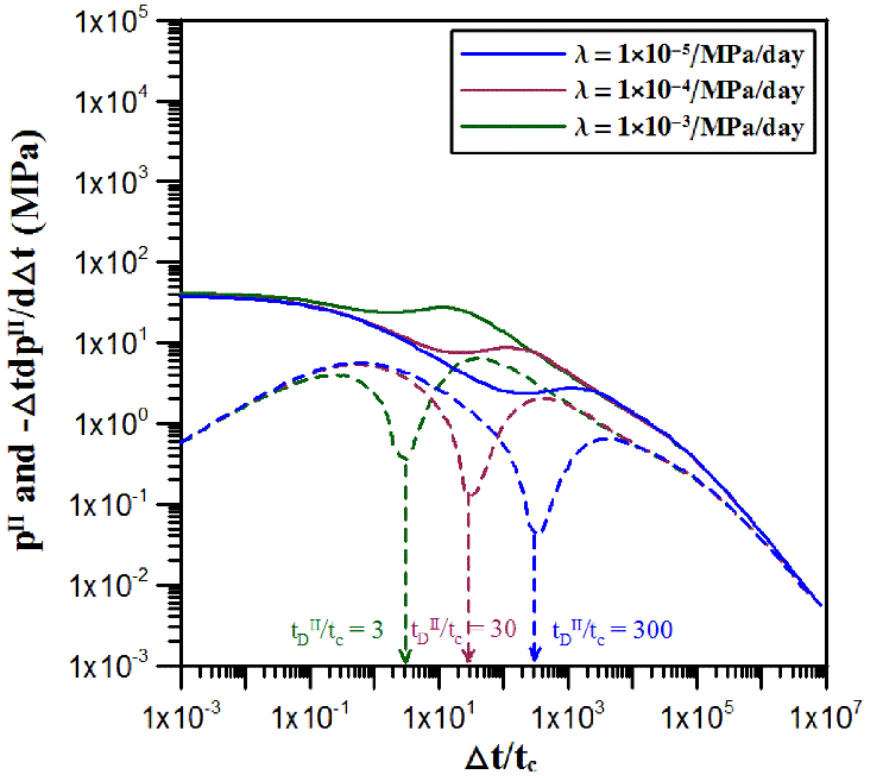

Figure 3.9—Effects of inter-porosity flow coefficient on the evolution of p^{II} & $-\Delta t dp^{II}/d\Delta t$. The time marker for the dip base is inversely proportional to λ.

Denoting the time markers of the dip bases in $-\Delta t dp^{I}/d\Delta t$ and $-\Delta t dp^{II}/d\Delta t$ curves by t_D^I and t_D^{II}, sensitive analysis based on Eq. B-1 indicates that the time markers have the following forms:

$$t_D^I = C_0 \frac{\left(\lambda_A^I\right)^a \left(\lambda_A^{II}\right)^{1-a}}{\lambda} \frac{\nu^I k^I}{\nu^{II} k^{II}} \quad \text{..... (3.17)}$$

$$t_D^{II} = C_0 \frac{\left(\lambda_A^{II}\right)^a \left(\lambda_A^{I}\right)^{1-a}}{\lambda} \frac{\nu^{II} k^{II}}{\nu^{I} k^{I}} \quad \text{..... (3.18)}$$

where λ_A^I and λ_A^{II} are the two eigenvalues of the matrix A.

The pressure derivative curves shown in Figure 3.8 and Figure 3.9 indicate that $t_D^I/t_c \approx 1.0\times10^5$ and $t_D^{II}/t_c \approx 300$ when λ = 1 × 10^{-5}/MPa/D. Substitution of the two

values into Eqs. 30 and 31 provides that: $C_0 \approx 0.6$, a ≈ 6.4. Eqs. 3.17 and 3.18 indicate that the time markers of the base dip in both matrix and fracture derivative curves are inversely proportional to the inter-porosity flow coefficient. In fact, similarly, the time markers of the hump in matrix and fracture pressure curves also could be determined to be inversely proportional to the inter-porosity flow coefficient, as shown in Figure 3.8 and Figure 3.9.

Next, the time marks of upper limit time for pseudo-linear flow and the lower limit time for pseudo-radial flow will be given for both matrix and fracture pressure derivative curves.

Denoting the time marks of upper limit for pseudo-linear regime in $-\Delta tdp^{I}/d\Delta t$ and $-\Delta tdp^{II}/d\Delta t$ curves by t_U^I and t_U^{II}, and lower limit for pseudo-radial regime in $-\Delta tdp^{I}/d\Delta t$ and $-\Delta tdp^{II}/d\Delta t$ curves by t_L^I and t_L^{II}, respectively, the above analysis shows that t_U^I and t_L^I have the same form with Eq. 3.17, t_U^{II} and t_L^{II} have the same form with Eq. 3.18. Figure 3.8 and Figure 3.9 indicate that $t_U^I / t_c \approx t_U^{II} / t_c \approx 0.4$ when λ = 1 × 10^{-5}/MPa/D. Substitution of the two values into Eqs. 3.17 and 3.18 provides $C_0 \approx 1.4 \times 10^{-4}$, a ≈ 3.1 for t_U^I and t_U^{II}. Figure 3.8 and Figure 3.9 also indicate that $t_L^I / t_c \approx t_L^{II} / t_c \approx 2 \times 10^5$ when λ = 1 × 10^{-5}/MPa/D. Substitution of the two values into Eqs. 3.17 and 3.18 provides $C_0 \approx 67.8$, a ≈ 1.3 for t_L^I and t_L^{II}.

To investigate when the two porous media reach a state of equilibrium, a timescale (Mehrabian and Abousleiman 2015a) can be defined by

$$\tau = \left(\frac{1}{\overline{M}^{I}} + \frac{1}{\overline{M}^{II}} \right) \Big/ \lambda \quad \text{..... (3.19)}$$

Figure 3.3 shows that, for the case of $\lambda = 1\times10^{-5}$/MPa/day, the two porous media reach a state of equilibrium when $\Delta t/t_c > 3\times10^4$ which approximately corresponds to the relation of $\Delta t > 5.8\tau$. Such relation is further supported by the cases of $\lambda = 1\times10^{-4}$/MPa/day and $\lambda = 1\times10^{-3}$/MPa/day. One can imagine that the two porous media behave as one medium for large enough λ and never reach equilibrium during the test for small enough λ. Extreme cases of $\lambda = 0$ and $\lambda = \infty$ are illustrated in Figure 3.3.

It is also interesting to define another time scale when the two systems start the pseudo-radial flow. Before giving the definition, the time scales for the matrix and fracture to start their own pseudo-radial flow for the case of no inter-porosity flow should be defined.

Using the effective pressure diffusion coefficients discussed in Chapter 2, the time scales for matrix and fracture to start the pseudo-radial flow for the case of no inter-porosity flow can be defined, respectively, as follows:

$$\bar{\tau}^{I} = L_e^2 \bar{\lambda}^{I} \quad \text{..... (3.20)}$$

$$\bar{\tau}^{II} = L_e^2 \bar{\lambda}^{II} \quad \text{..... (3.21)}$$

Then the time scale, τ_r, for the two systems to start the pseudo-radial flow can be defined by taking the harmonic average over the above two time scales as follows:

$$\frac{1}{\tau_r} = \frac{\mathrm{v}^{I}}{\bar{\tau}^{I}} + \frac{\mathrm{v}^{II}}{\bar{\tau}^{II}} \quad \text{..... (3.22)}$$

Figure 3.3 shows that, for the case of $\lambda = 1\times10^{-5}$/MPa/day, the two systems start the pseudo-radial flow when $\Delta t/t_c > 4\times10^5$ which approximately corresponds to the relation of $\Delta t > 0.1\tau_r$. This time scale, τ_r, is not sensitive to the inter-porosity flow

coefficient as shown in Figure 3.3. That is why its definition does not involve the inter-porosity flow coefficient.

3.3 Summary

In this section, a numerical example is presented to illustrate wellbore pressure decline after hydraulic fracture closure in a dual-porosity dual-permeability formation. The pseudo-linear flow regime, transient period and pseudo-radial flow regime are clearly identified in the log-log plots of the dual-pressure derivative curves. Furthermore, it is also illustrated how to estimate the dual permeabilities based on the combination of 1/2 slope and -1 slope or the combination of -1/2 slope and -1 slope. It is shown that the dual permeabilities and hydraulic fracture length can also be estimated based on the -1 slope and the straight line behavior in the plot of pressure vs. square root time. Different time markers are also defined, allowing to estimate the inter-flow coefficient. Two time scales are also defined to investigate the time when the two porous media reach a state of equilibrium and the time when the pseudo-radial flow starts.

Chapter 4 : Field Applications

In this Chapter, the newly-derived analytical solution is utilized to analyze field data. Three field cases are studied. Field data for the first two cases is digitized from Chipperfield (2005; 2006), and field data for the third case is provided by Halliburton. The dual-porosity dual-permeability nature of the studied formations can be clearly identified by the hump in the pressure curves or the dip in the pressure derivative curves. 1/2 and -1 slopes are also observed to show the pseudo-linear and pseudo-radial flow regimes. Because data is lacking to solve the corresponding equations (Eq. 3.2, 3.10, 3.14 and 3.15) to estimate the permeability and fracture length based on such slopes, another method is implemented by matching the analytical solution with field data.

Conventional well test parameters, including formation total compressibility and hydraulic diffusivity, were defined by reservoir engineers since the 1950s (Hall 1953), and corresponding correlations for their estimates have to date been used in industry practice of type curve and well testing analyses. However, they have never been revisited from a poromechanical standpoint. Such parameters are revisited and the equivalent poroelastic parameters are defined in this chapter.

4.1 Case Studies

4.1.1 Case Study 1

An Australian gas field (Chipperfield 2005; 2006) is revisited in this section to show the after-closure pressure analysis based on the previous theoretical methods. The gas field was inferred to have natural fractures by borehole-imaging tools. Pay thickness is 110 ft, and the average permeability is expected to be in the range of 0.2 to 0.5 md.

The reservoir pressure (p_i) was measured to be 2,240 psi before the stimulation treatment. A step-rate test was implemented, and a volume of 5,000 gal fluid was injected into the well at 1 to 12 bbl/min. During the step-rate test, a fluid was injected into the well for a defined period in a series of increasing pump rates. The NDP (Economides and Nolte 2000), which represents the pressure difference ($\Delta p = p_w - p_i$) vs. the inverse squared Nolte time ($1/F_l^2$), is digitized from Chipperfield (2006) and used to plot Figure 4.1 by changing the time scale to $\Delta t/t_c$. In Figure 4.1, the pressure derivative data are added, which is defined as follows (Uribe et al. 2007):

$$-\Delta t\frac{dp}{d\Delta t}=-\left(\frac{dp}{d\ln t}\right)_i=-\frac{\left[\frac{(p_i-p_{i-1})(\ln t_{i+1}-\ln t_i)}{\ln t_i-\ln t_{i-1}}+\frac{(p_{i+1}-p_i)(\ln t_i-\ln t_{i-1})}{\ln t_{i+1}-\ln t_i}\right]}{(\ln t_{i+1}-\ln t_{i-1})} \quad \text{..... (4.1)}$$

The hump in the pressure difference plot and the dip in the pressure derivative plot indicate the existence of natural fractures in this gas field. The slope of 1/2 at $\Delta t \rightarrow 0^+$, the slope of -1 at $\Delta t \rightarrow \infty$, and the dip in the pressure derivative plot can be clearly identified in Figure 4.1. Considering that the formation is naturally fractured, the matrix permeability may be lower relative to that of the fracture system, and the fracture system may tend to communicate with the wellbore better than the matrix does. Then, the recorded wellbore pressure might tend to reflect the fracture pressure. Therefore, it is reasonable to use equations similar to Eqs. 3.2 and 3.10 to estimate matrix and fracture permeability. The average permeability of the formation can be approximately determined as 0.62 mD, using Eq. 3.2. If the poromechanical properties of the formation are known, substitution of them into the two equations can be used to estimate the matrix and fracture permeability. It should be noted that the slope of -1/2

is not clearly observed in Figure 4.1, which indicate that the permeability of the formation is not very low, as proved in Chapter 2.

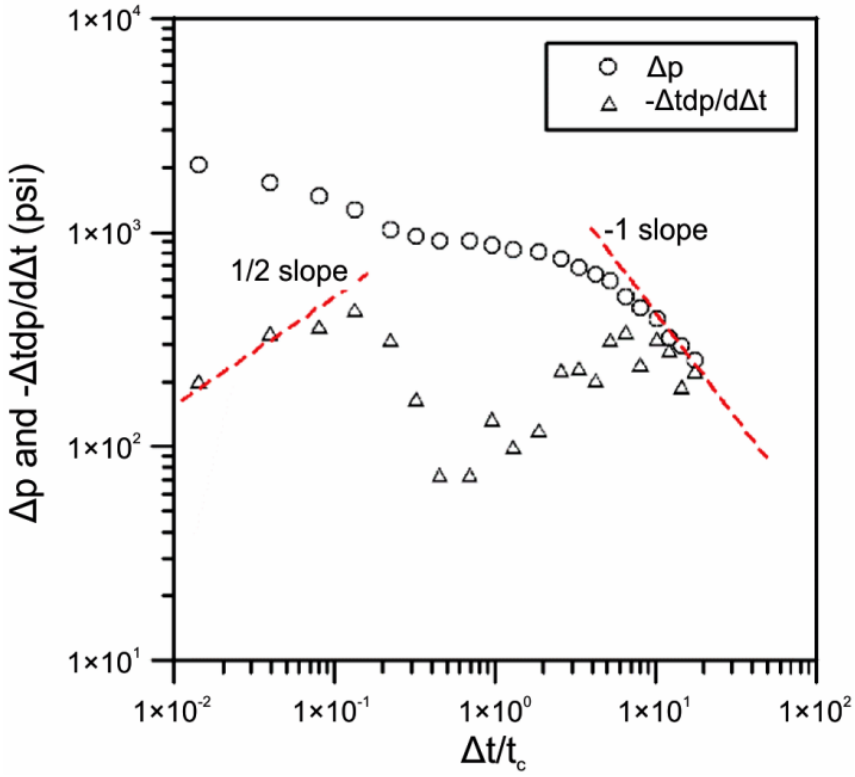

Figure 4.1—Evolution of Δp and –Δtdp/dΔt at the wellbore for field data 1. The hump and trough in the pressure and pressure derivative curves clearly indicate a dual-porosity dual-permeability rock formation.

Figure 4.2 shows the plot of $-dp/d\Delta t$ vs. $\Delta t/t_c$. The slopes of -1/2 and -2 can be clearly identified, which correspond to the slope 1/2 and -1 in Figure 4.1, respectively.

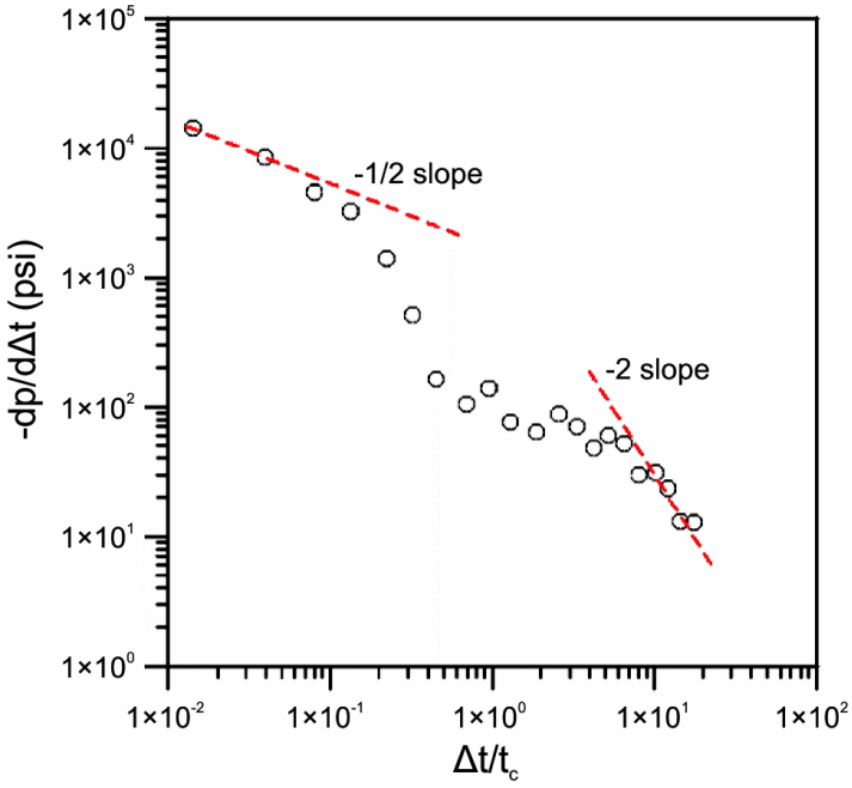

Figure 4.2—Evolution of -dp/dΔt at the wellbore for field data 1. -1/2 and -2 slopes clearly identify the pseudo-linear and pseudo-radial flow regimes, respectively.

Figure 4.3 shows the plot of Δp vs. $(\Delta t/t_c)^{1/2}$. The straight-line asymptotic behavior during the pseudo-linear flow period can be used to estimate matrix permeability, fracture permeability, and fracture length by solving Eqs. 15, 27, and 28 once the poromechanical properties of the formation are known.

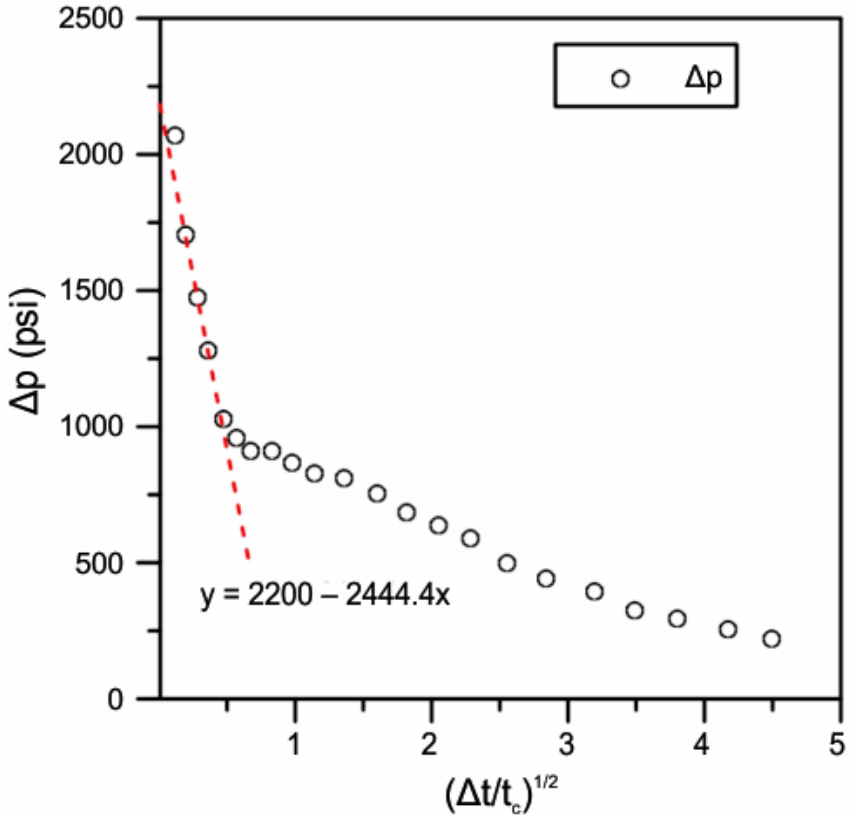

Figure 4.3—Linear-Sqrt Time plot of Δp for field data 1. The straight-line behavior is clearly observed in the pseudo-linear flow regime.

Because data is lacking to solve the corresponding equations to estimate the permeability and fracture length, another method is implemented by matching the analytical solution with the field data. Note that the water formation volume factor can often be neglected because it is close to 1.0 under most conditions. Furthermore, the injected fluid used in the step-rate test is usually an incompressible Newtonian fluid (Mader 1989). Therefore, it is reasonable to set the water formation volume factor as 1.0. An incompressible fluid is also assumed, and the wellbore storage effects are neglected in this chapter. Such assumptions are consistent with Chipperfield (2006).

The value of 5,000 gal is treated as the volume of fluid injected into the formation. In the match, when an average pump rate of 6 bbl/min (i.e., Q_0 = 6 bbl/min) is selected, the equivalent pump time t_p can be calculated to be 20.3 min based on the 5,000 gal of fluid injected. Fracture height, H, is assumed to equal the pay thickness of 110 ft. To obtain a good match between the two, the fracture closure time, t_c, is selected as 30 min and equivalent fracture length, L_e, is selected as 35 ft. Other data used for the analytical solutions are presented in Table 4.1.

Figure 4.4 shows the NDP match between the analytical solutions and the field data. It can be observed that the fracture pressure curve fit the field data well. One of the reasons that the fracture pressure rather than the matrix pressure can fit the field data is that the fracture may be able to communicate with the wellbore better than the matrix because of the relatively higher permeability of the fracture. The recorded field wellbore pressure data may tend to represent the fracture pressure at the wellbore.

Table 4.1— Input for the analytical solutions to match field data 1.

Parameters	K (GPa)	ν	B	α	k (md)	μ (cp)	v (%)	λ (1/MPa/D)
Matrix (I)	6	0.2	0.2	0.8	0.3	1	95	5.0×10^{-2}
Fracture (II)	2	0.2	0.8	0.88	8	1	5	

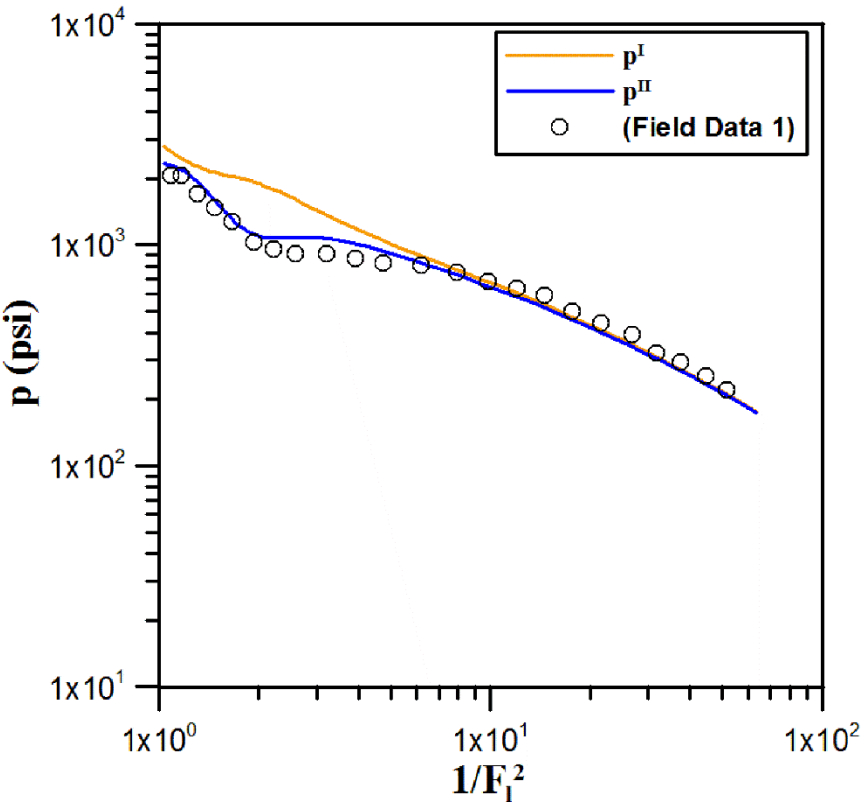

Figure 4.4—NDP match between analytical solutions and field data 1. A good match between fracture pressure and field data 1 is observed.

Figure 4.5 shows the pressure and pressure derivative match between the field data and the analytical solutions, with the time scale defined by $\Delta t/t_c$. A good match is observed for both the pressure and pressure derivative curves. The estimated average permeability from the match is $k_{avg} = v^I k^I + v^{II} k^{II} = 0.69$ md, which is in good agreement with the reported value in Chipperfield (2006) (i.e., approximately 0.2 to 0.5 md).

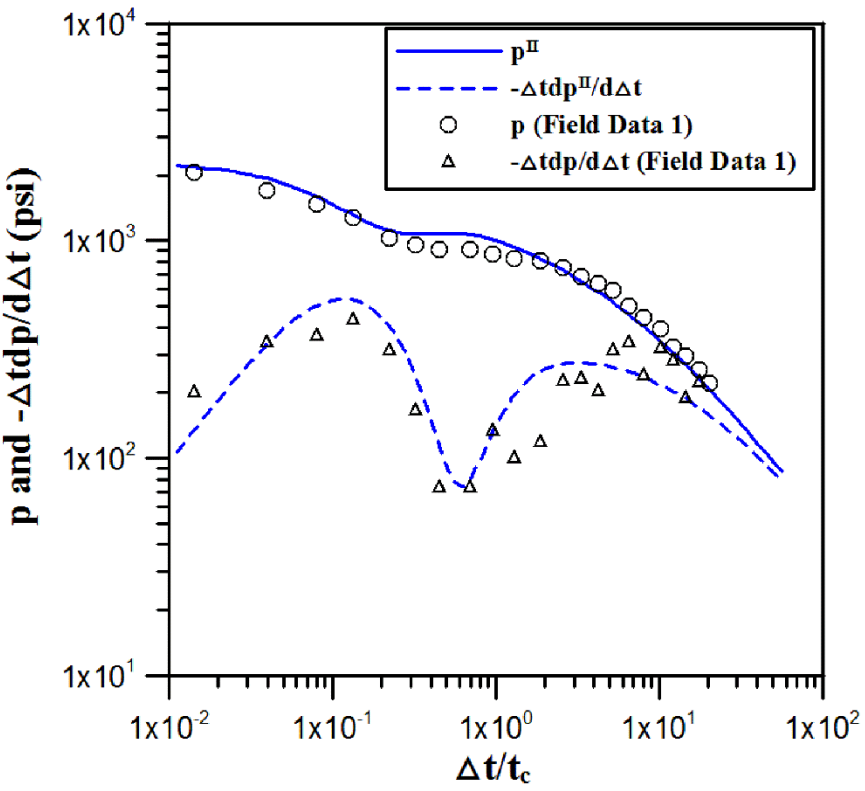

Figure 4.5—Pressure and pressure derivative match between fracture and field data 1. A good match is obtained.

To show how the poromechanical and physical properties of the formation influence the fracture pressure at the wellbore, sensitivity analysis is performed, as shown in Figure 4.6 through Figure 4.14. For comparison, all parameters are halved or doubled, except the fracture Skempton's coefficient and Biot's coefficient, both of which are larger than 1 when keeping doubled. Figure 4.6 shows the influence of the inter-porosity flow coefficient on the pressure match between the analytical solution and the field data. It can be observed that when the inter-porosity flow coefficient decreases or increases, the hump in the pressure curve shifts to the right and left, respectively, which is in agreement with previous analysis.

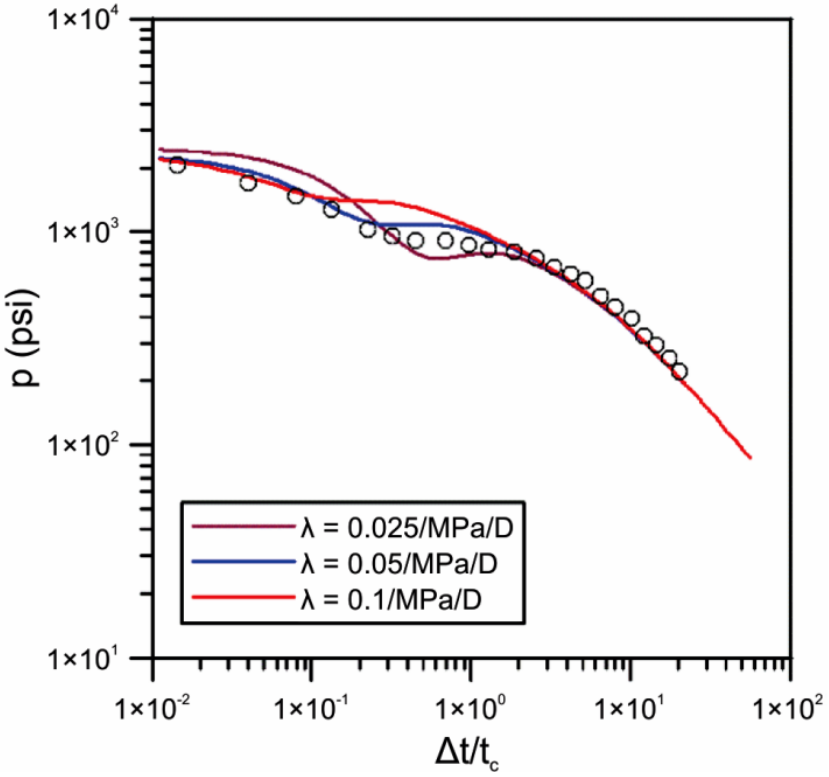

Figure 4.6—Effects of λ on the match between p^{II} and field data 1. p^{II} is sensitive to λ.

Figure 4.7 through Figure 4.14 show the sensitivity analysis on the physical and poromechanical parameters. Figure 4.7 and Figure 4.8 show that the fracture pressure at the wellbore is sensitive to both matrix and fracture permeability. When increasing the matrix and fracture permeability, the pressure curve during the pseudo-radial flow period will shift downward, which can be supported by Eq. 16 (i.e., the intercept pressure value p_i should be decreased to increase k_{avg}). Furthermore, the fracture pressure at the wellbore is sensitive to the matrix bulk modulus, Skempton's coefficient, and Biot's coefficient, as shown in Figure 4.9, Figure 4.11 and Figure

4.13. However, it is not sensitive to the fracture bulk modulus, Skempton's coefficient, and Biot's coefficient, as shown in Figure 4.10, Figure 4.12 and Figure 4.14.

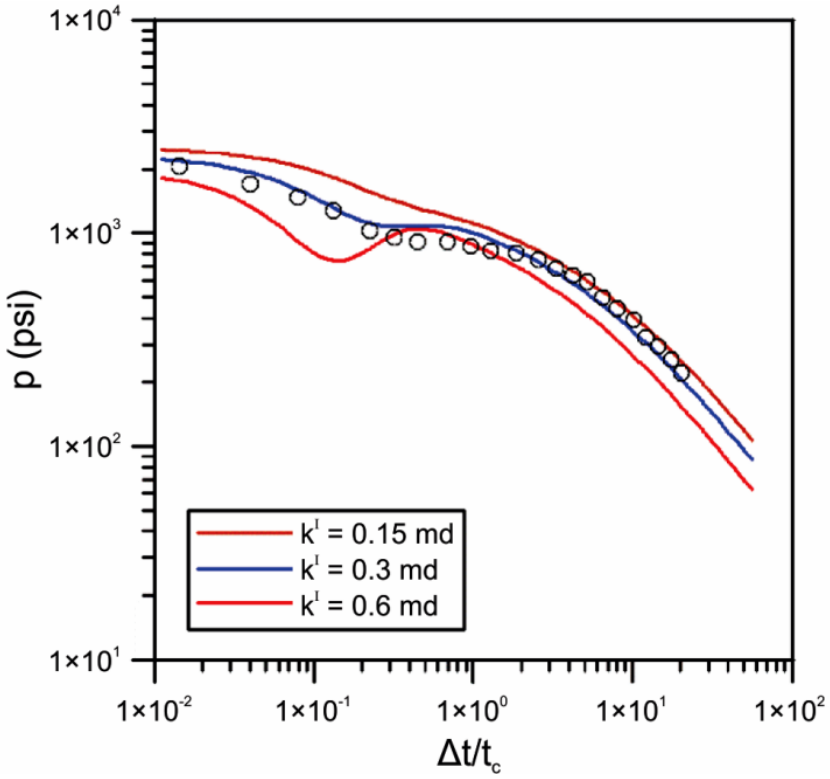

Figure 4.7—Effects of k^I on the match between p^{II} and field data 1.

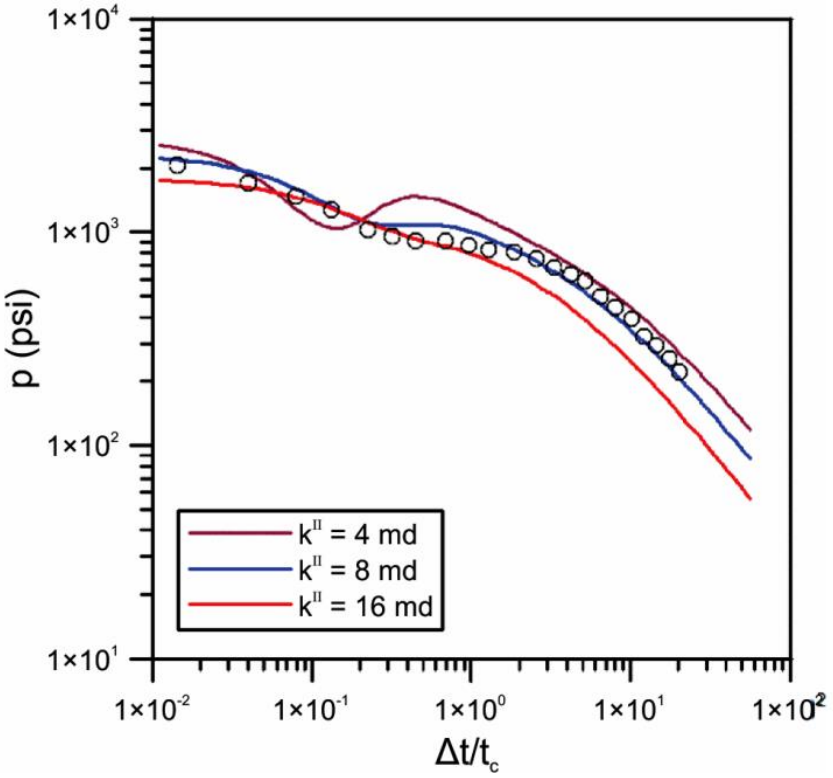

Figure 4.8—Effects of k^{II} on the match between p^{II} and field data 1.

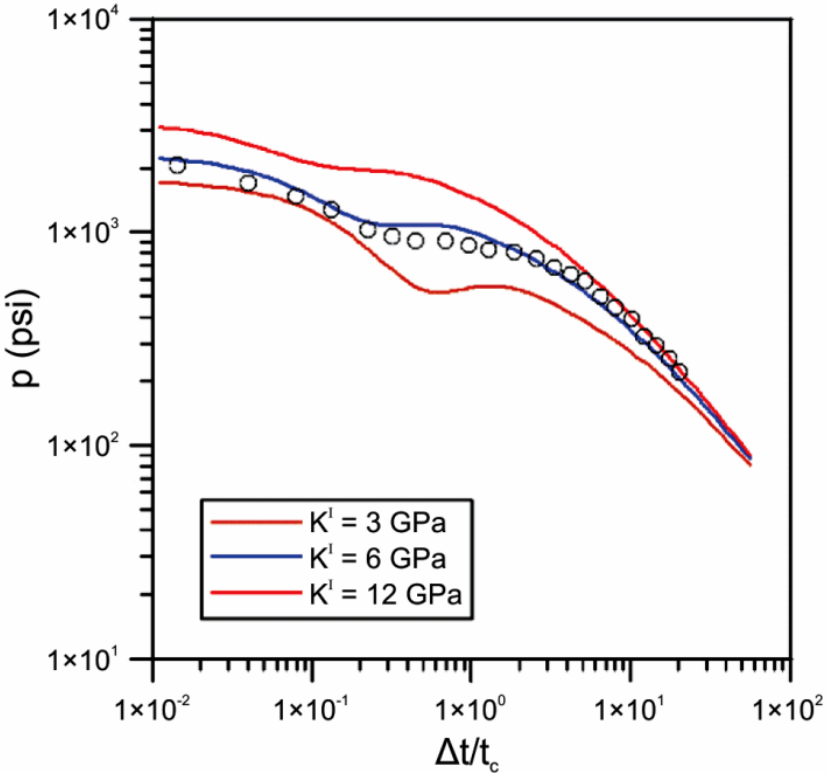

Figure 4.9—Effects of K^{I} on the match between p^{II} and field data 1.

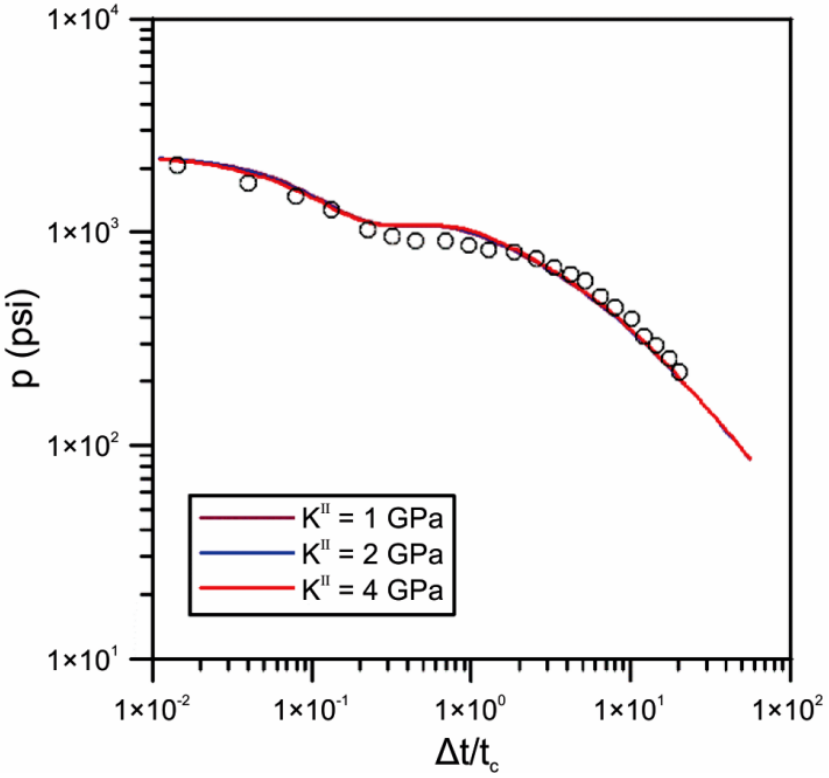

Figure 4.10—Effects of K^{II} on the match between p^{II} and field data 1.

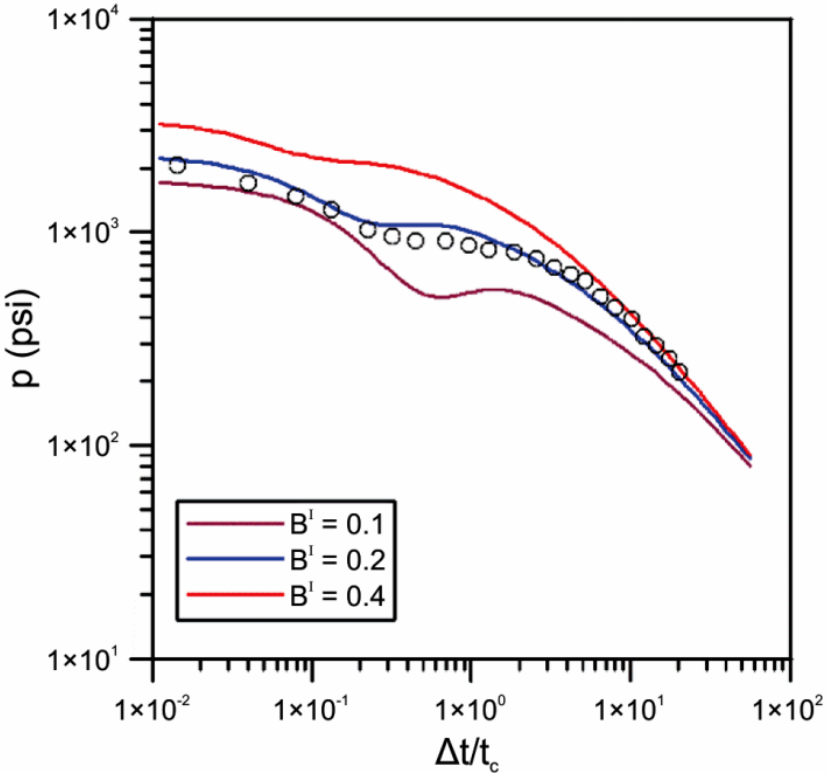

Figure 4.11—Effects of B^{I} on the match between p^{II} and field data 1.

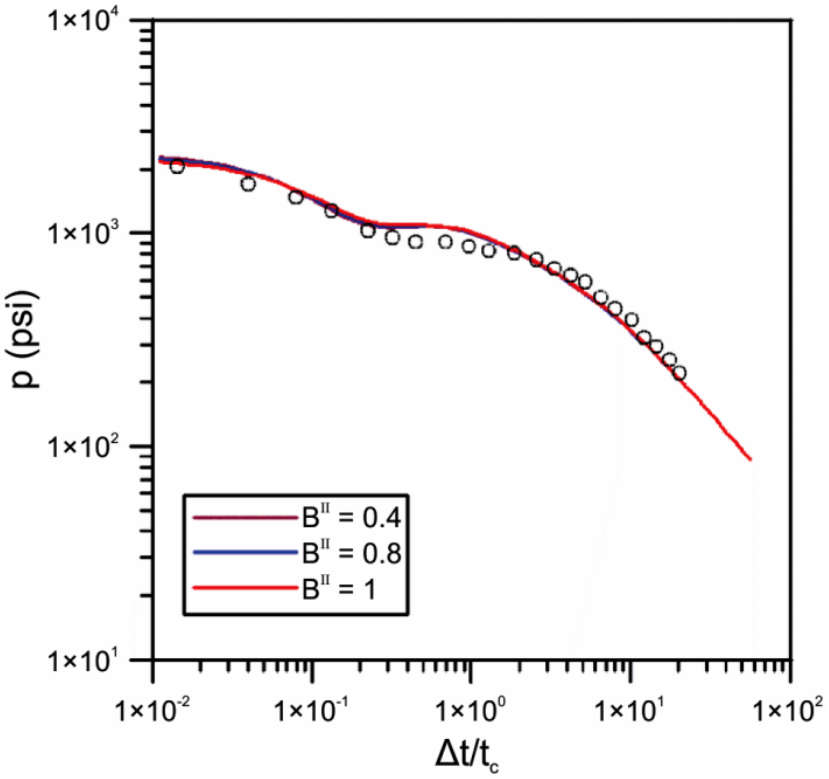

Figure 4.12—Effects of B^{II} on the match between p^{II} and field data 1.

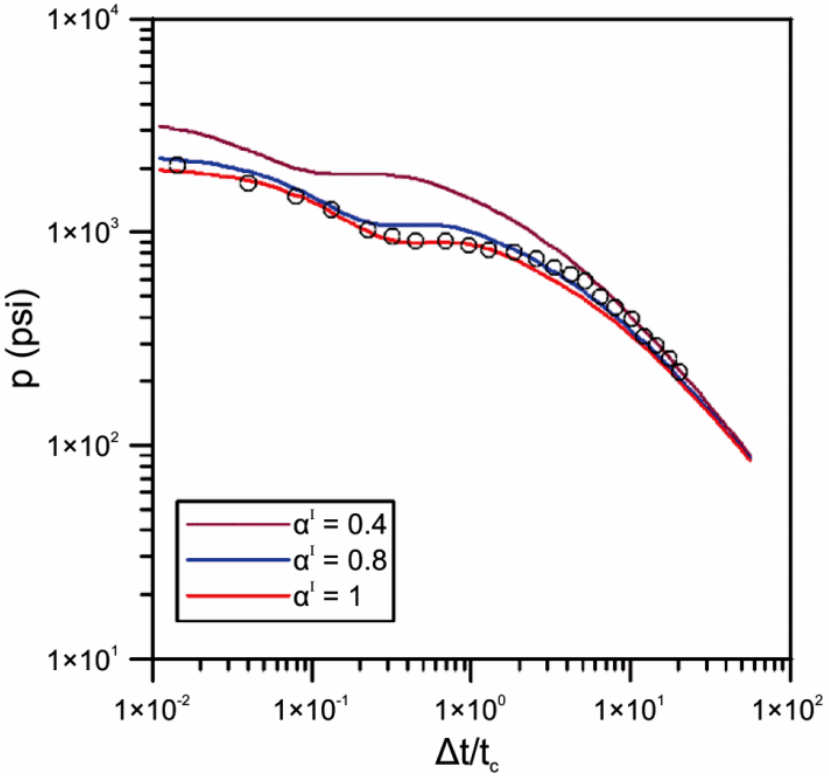

Figure 4.13—Effects of α^{I} on the match between p^{II} and field data 1.

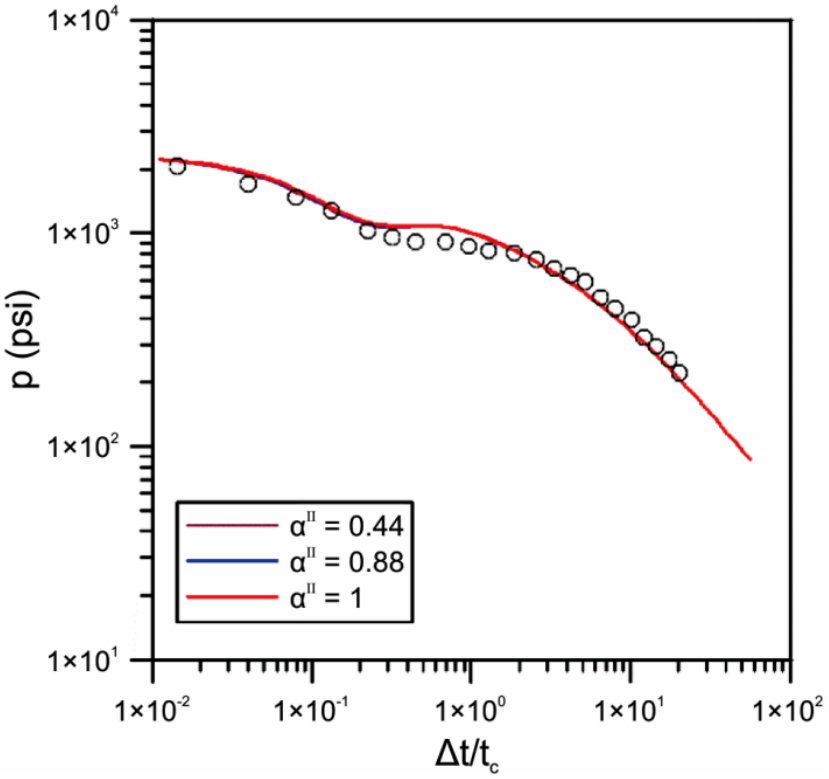

Figure 4.14—Effects of α^{II} on the match between p^{II} and field data 1.

Taking the Skempton's coefficient as an example, the match between p^{II} and field data is sensitive to B^{I}, yet not sensitive to B^{II} in this case. The sensitivity is essentially controlled by the matrix $A^{-1}D$ and $A^{-1}\Gamma$ in the pressure governing equation Eq. 2.1. Note that the sensitivity to one parameter is also dependent on the values of other parameters.

The previous analysis shows that the after-closure pressure at the wellbore is sensitive to both matrix and fracture permeability and matrix poromechanical parameters. To obtain an estimation that represents formation properties, it might not be sufficient to use the Warren and Root dual-porosity model, which ignores the fluid communication between matrix elements and in which only pure fracture flow is considered. Furthermore, the idealized "sugar cube" geometry in the Warren and Root

model might make the results problematic when treating many dual-porosity formations, for example, organic-rich shale formations. To obtain a more convincing estimation of a dual-porosity formation's properties, it is necessary to use the current poroelastic dual-porosity dual-permeability model for the analysis.

4.1.2 Case Study 2

Another Australian gas field (Chipperfield 2005) is studied in this section. The gas field was inferred to have natural fractures from core and offset well tests over the treatment interval (Chipperfield 2005). Pay thickness is estimated to be 82 ft. The reservoir pressure (p_i) was measured to be 3090 psi by bottomhole gauges before the stimulation treatment. During the impulse fracture test, a 13500 gal injection was implemented at a rate of 30 bbl/min. The after-closure portion of wellbore pressure data is digitized from Chipperfield (2005) and utilized to plot Figure 4.15 and Figure 4.16. The straight-line behavior is clearly identified in the plot of Δp vs. $(\Delta t/t_c)^{1/2}$ during the pseudo-linear flow regime, as shown in Figure 4.15.

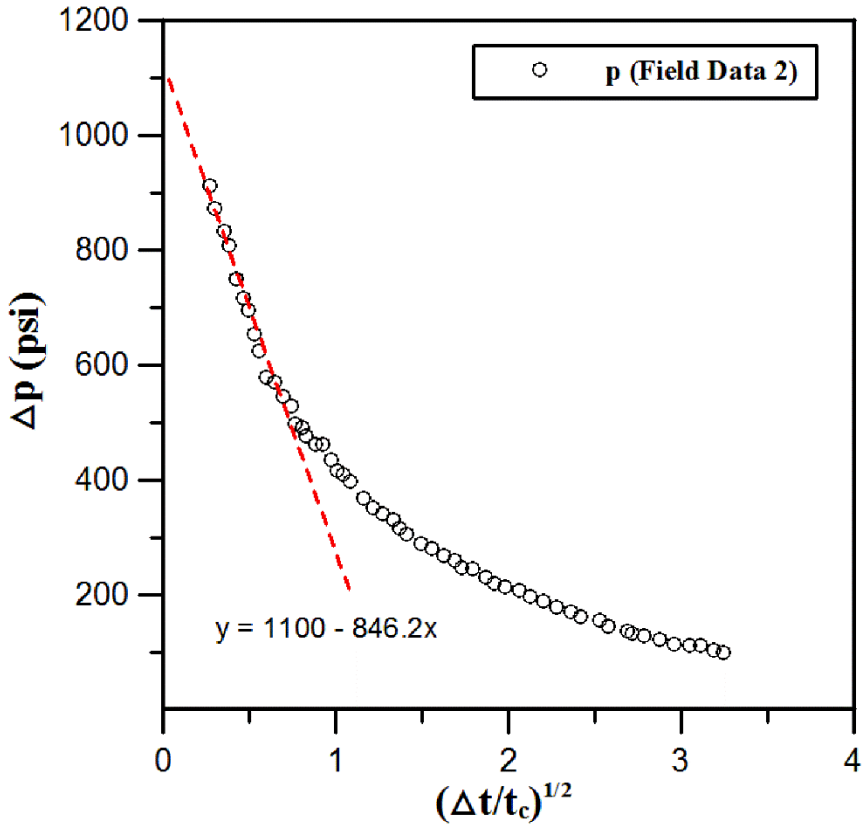

Figure 4.15—Linear-Sqrt Time plot of Δp for field data 2. The straight-line behavior is clearly observed in the pseudo-linear flow regime.

Figure 4.16 shows the plots of Δp and $-\Delta t d\Delta p/d\Delta t$ vs. $\Delta t/t_c$. Different from field data 1, the hump in the pressure curve cannot be clearly observed. But the dip in the pressure derivative curve can be clearly detected to identify the dual-porosity dual-permeability nature of the formation.The 1/2 and -1 slopes can be clearly observed from the pressure derivative curve during the pseudo-linear and pseudo-radial flow regimes. Based on the -1 slope, the formation average permeability can be estimated to be around 13.3 mD.

The analytical solution of the fracture pressure is applied to match the field data 2. Figure 4.16 shows that the analytical solution is able to capture the wellbore pressure

data to some extent. Inputs of the formation parameters are listed in Table 4.2. Other inputs for the stimulation treatment are listed as follows: H = 250 ft, Q_0 = 30 bbl/min, t_p = 10 min, t_c = 12 min, L_e = 8.2 ft.

Table 4.2—Input for the analytical solutions to match field data 2.

Parameters	K (GPa)	ν	B	α	k (md)	μ (cp)	v (%)	λ (1/MPa/D)
Matrix (I)	4	0.2	0.06	1	9	1.2	94	0.16
Fracture (II)	0.036	0.2	0.8	1	80	1.2	6	

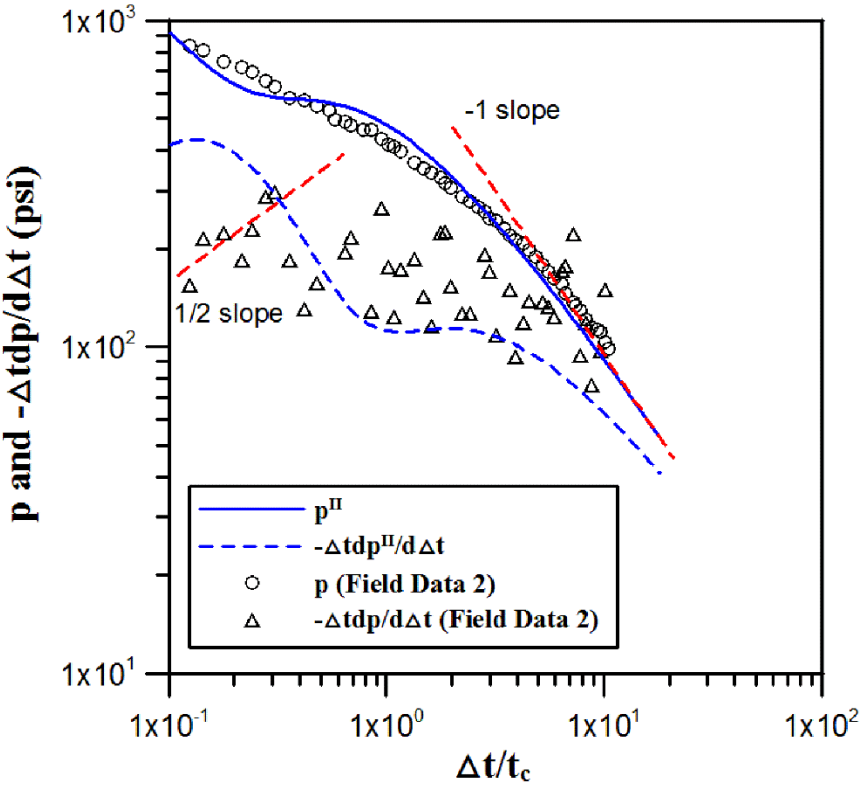

Figure 4.16—Pressure and pressure derivative match between fracture and field data 2.

Compared to the formation in Case Study 1, the one in Case Study 2 has higher matrix permeability, fracture permeability, and the inter-porosity flow coefficient. This

estimation is consistent with the studies presented by Warren and Root (1963) who showed that the matrix permeability is one of the factors that control the inter-porosity flow coefficient, specifically, higher matrix permeability usually leads to larger inter-porosity flow coefficient.

4.1.3 Case Study 3

The field data in this case is provided by Halliburton. The portion of the wellbore after-closure pressure is plotted in Figure 4.17 and Figure 4.18.

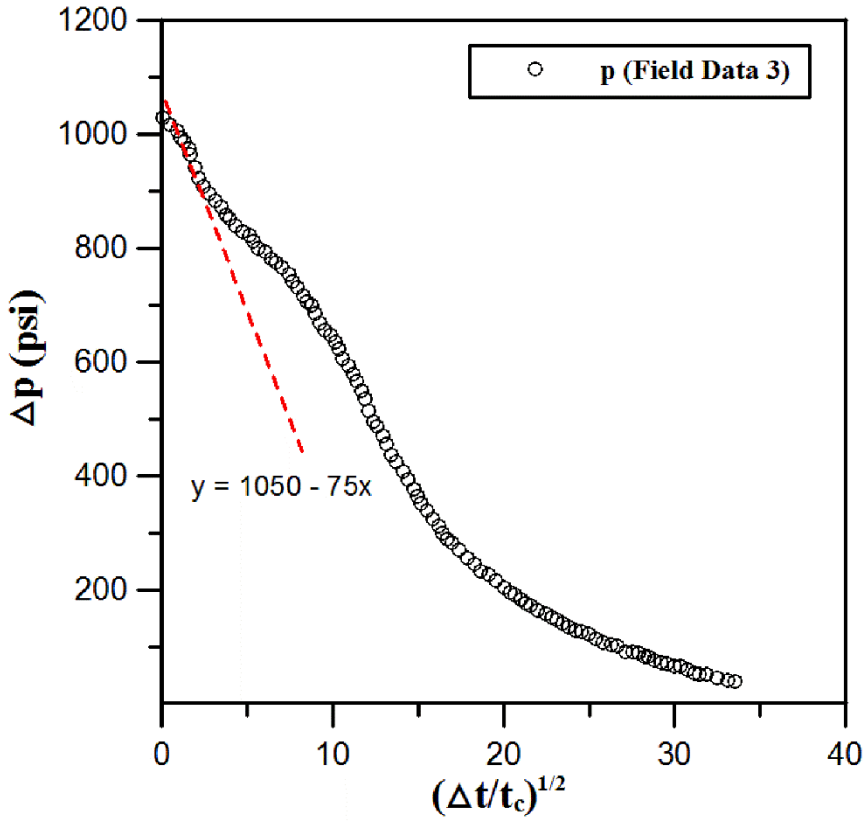

Figure 4.17—Linear-Sqrt Time plot of Δp for field data 3. The straight-line behavior is clearly observed in the pseudo-linear flow regime.

Figure 4.17 shows the plot of Δp vs. $(\Delta t/t_c)^{1/2}$ in which the straight-line behavior can be found during the pseudo-linear flow regime. Figure 4.18 shows the plots of Δp and

$-\Delta t d\Delta p/d\Delta t$ vs. $\Delta t/t_c$. The dual-porosity dual-permeability nature of the formation can be clearly identified by the dip behavior in the pressure derivative curve. 1/2 and -1 slopes can be also located on the pressure derivative curve to determine the pseudo-linear and pseudo-radial flow regimes. Formation average permeability is estimated to be around 1.6×10^3 nD, based on the -1 slope during the pseudo-radial flow.

Table 4.3—Input for the analytical solutions to match field data 3.

Parameters	K (GPa)	ν	B	α	k (md)	μ (cp)	v (%)	λ (1/MPa/D)
Matrix (I)	12	0.3	0.8	0.88	18×10^{-6}	1	99	1.5×10^{-5}
Fracture (II)	0.15	0.3	0.96	0.9	0.16	1	1	

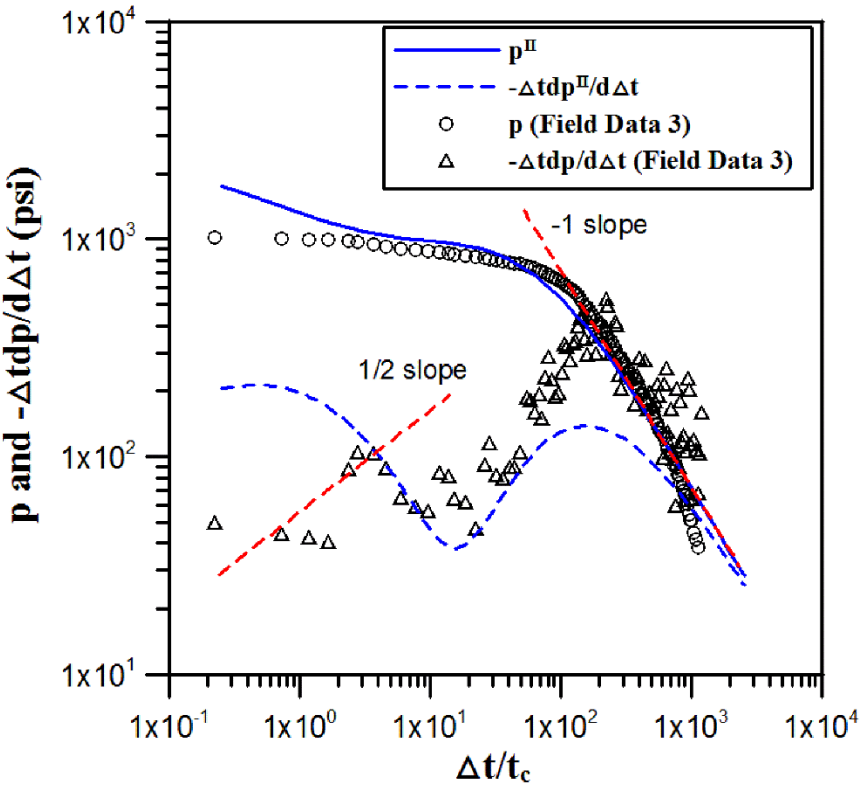

Figure 4.18—Pressure and pressure derivative match between fracture and field data 3.

The analytical solution of fracture pressure is applied to match field data 3. Inputs for the analytical solutions are listed in Table 4.3. Other inputs are listed as follows: H = 16 ft, Q_0 = 14 bbl/min, t_p = 10 min, t_c = 50 min, L_e = 19.7 ft.

Figure 4.18 shows the match between the analytical fracture pressure and the field data 3. The analytical solution is capable of capturing both pressure and pressure derivative curves. Compared to the former two cases, the formation in case 3 has the lowest matrix permeability and also the smallest inter-porosity flow coefficient. This observation further supports the statement that lower matrix permeability usually results in smaller inter-porosity flow coefficient.

4.2 Equivalent Poroelastic Well Test Parameters

In this section, some conventional well test parameters are revisited and the equivalent poroelastic parameters are defined, beginning with storage coefficients. In the area of hydrology, the storage coefficient or storativity is the volume of water released from storage per unit of surface area of an aquifer under a unit decline in the hydraulic head (Freeze and Cherry 1979). Various work has been performed to determine the storage coefficient from pumping tests. Cooper and Jacob (1946) present a method to determine the storage coefficient based on the drawdown data collected during pumping. Banton and Bangoy (1996) propose a new method, which allows determining the storage coefficient from recovery data collected from two or more locations.

For a poroelastic porous medium saturated with fluid, the unconstrained storage coefficient, S_σ, is the change of fluid content variation per unit change of the fluid

pressure when fixing the external confining pressure and is defined by the following equation (Berryman and Wang 1995; Wang 2000):

$$S_\sigma = \left.\frac{\partial \zeta}{\partial p_f}\right|_{\delta p_c = 0} = \frac{\alpha}{BK} \quad \text{..... (4.2)}$$

where ζ is the variation of fluid content, p_f is the fluid pressure, p_c is the confining pressure, α is the Biot's coefficient, B is the Skempton's coefficient, and K is the bulk modulus. For the dual-porosity model used in this chapter, the matrix and fracture unconstrained storage coefficients are $v^I\alpha^I/B^IK^I$ and $v^{II}\alpha^{II}/B^{II}K^{II}$, respectively (Berryman and Wang 1995). The unconstrained cross-storage coefficient is approximated by zero (Mehrabian and Abousleiman 2014) (i.e., the fluid volume change in one porous medium resulting from a pressure change in the other porous medium is negligible when keeping the confining pressure unchanged).

Wang (2000) also presents the constrained storage coefficient, S_ε, which is the fluid volume released from storage per unit of control volume per unit of pressure decline while maintaining the control volume constant and is defined by

$$S_\varepsilon = \left.\frac{\partial \zeta}{\partial p_f}\right|_{\varepsilon = 0} = \frac{1}{M} \quad \text{..... (4.3)}$$

where M is the Biot's modulus. For the dual-porosity model used in this chapter, the constrained and coupled matrix and the fracture and cross-storage coefficients are $1/\overline{M}^{I}$, $1/\overline{M}^{II}$ and $1/\overline{M}^{I,II}$, respectively. It can be observed that the constrained cross-storage coefficient is nonzero. As a matter of fact, its value is negative, which physically means that an increase in pressure in one porous medium tends to release fluid from the other porous medium when the bulk volume is unchanged.

Warren and Root (1963) define the storativity ratio ω as follows:

$$\omega = \frac{C_f \phi_f}{C_f \phi_f + C_m \phi_m} \quad \text{..... (4.4)}$$

where C_m and C_f are the matrix and fracture compressibility, respectively, and ϕ_m and ϕ_f are the matrix and fracture porosity, respectively. ω is less than 1 and stands for the fracture storage volume fraction. The Warren and Root model assumes only pure fracture fluid flow exists without matrix fluid flow to the wellbore, and the matrix only acts as storage.

Two other interesting terms that will be discussed below are the hydraulic diffusivity and total compressibility. Conventional hydraulic diffusivity is defined by

$$c = k/\mu\phi C_t \quad \text{..... (4.5)}$$

where ϕ is the porosity and the total compressibility C_t is defined by $C_t = C_g S_g + C_o S_o + C_w S_w + C_{formation}$ (Lee et al. 2003) and especially equals $C_w + C_{formation}$ for a formation fully saturated with water, where C_g, C_o, and C_w are the gas, oil, and water compressibilities, respectively, S_g, S_o, and S_w are the gas, oil, and water saturations, respectively, and $C_{formation}$ is the formation compressibility.

Comparison between Eq. 33 with Eq. 38 allows to define the equivalent poroelastic total compressibility as follows:

$$C_t^p = \frac{\alpha^2 B(1+v) + 3(1-v)(\alpha - \alpha^2 B)}{3BK(1-v)} \quad \text{..... (4.6)}$$

where the porosity term ϕ plays the role of switch between average over bulk volume and pore volume and is excluded from such definition.

Table 4.4 compares the conventional well test parameters with the equivalent poroelastic parameters for a fully saturated formation.

Table 4.4—Conventional well test parameters vs. equivalent poroelastic parameters; fully saturated.

	Conventional Well Test Parameters		Equivalent Poroelastic Parameters
Single porosity	Total compressibility	$C_w + C_{formation}$	$\frac{\alpha^2 B(1+\nu) + 3(1-\nu)(\alpha - \alpha^2 B)}{3BK(1-\nu)}$
	Hydraulic diffusivity	$\frac{k}{\mu\phi C_t}$	$\frac{k}{\mu}\frac{3BK(1-\nu)}{\alpha^2 B(1+\nu) + 3(1-\nu)(\alpha - \alpha^2 B)}$
Dual porosity	Matrix storage	$C_{tm}\phi_m$	$1/\overline{M}^I$
	Fracture storage	$C_{tf}\phi_f$	$1/\overline{M}^{II}$
	Matrix diffusivity	$k^I/\mu\phi_m C_{tm}$	$1/\overline{\lambda}^I$
	Fracture diffusivity	$k^{II}/\mu\phi_f C_{tf}$	$1/\overline{\lambda}^{II}$

The parameters $\overline{M}^I$, $\overline{M}^{II}$, $\overline{\lambda}^I$ and $\overline{\lambda}^{II}$ can be identified in terms of the individual constituent's physical and poromechanical properties, such as $\nu^{(N)}$, $\nu^{(N)}$, $\alpha^{(N)}$, $B^{(N)}$ and $K^{(N)}$, N= I and II, and are shown explicitly in Berryman (2002), Nguyen and Abousleiman (2010), and Mehrabian and Abousleiman (2014).

Thus, when the corresponding individual constituent's physical and poromechanical properties are estimated, as presented in Table 4.1, the corresponding equivalent poroelastic parameters also can be estimated based on the previous analysis.

The primary significance of poroelasticity in this specific application and solution is identified by revisiting the problem parameters, i.e., formation total compressibility C_t and hydraulic diffusivity c in the case of single porosity, and their counterparts in the case of dual-porosity. These parameters have been defined by reservoir engineers since

the 1950s (Hall 1953), and corresponding correlations for their estimates have to date been used in the industry practice of type curve and well testing analyses. However, they have never been revisited from a poromechanical standpoint. Table 4.4 offers an in-depth review of these same parameters and characterizes them by the well-known poroelastic constants which can be measured through standard and established laboratory methods (Hart and Wang 1995; Berryman and Wang 1995) or well logging data (Abousleiman et al. 2007).

Finally, it is of interest to provide a brief review of the single and dual-porosity models and the evolution of their applications in the pressure decline analysis, as shown in Table 4.5.

Table 4.5—A brief review of the evolution of pressure decline analysis.

Author, year	Governing Equations	Comments
Gu et al. 1993 Abousleiman et al. 1994 Nolte et al. 1997 Soliman et al. 2005	$c\Delta p = \frac{\partial p}{\partial t}$	Single porosity
Barenblatt et al. 1960	$\frac{k^I}{\mu}\Delta p^I = (C_m + \phi_m C_w)\frac{\partial p^I}{\partial t} - \beta_* \frac{\partial p^{II}}{\partial t} - \frac{\alpha}{\mu}(p^{II} - p^I)$ $\frac{k^{II}}{\mu}\Delta p^{II} = (C_f + \phi_f C_w)\frac{\partial p^{II}}{\partial t} - \beta_{**} \frac{\partial p^I}{\partial t} + \frac{\alpha}{\mu}(p^{II} - p^I)$	Considers the flow in matrix

Houze et al. 1988	$\frac{k^I}{\mu}\Delta p^I = \phi_m C_{tm}\frac{\partial p^I}{\partial t}$ $\frac{k^{II}}{\mu}\Delta p^{II} = \phi_m C_{tm}\frac{\partial p^I}{\partial t} + \phi_f C_{tf}\frac{\partial p^{II}}{\partial t}$	Considers the flow in matrix; Matrix flow is decoupled from fracture flow
This chapter	$\frac{\mathrm{v}^I k^I}{\mu}\Delta p^I = \left[\frac{\left(\bar{\alpha}^I\right)^2}{\bar{\eta}} + \frac{1}{\bar{M}^I}\right]\frac{\partial p^I}{\partial t} - \left[\frac{\bar{\alpha}^I\bar{\alpha}^{II}}{\bar{\eta}} + \frac{1}{\bar{M}^{II}}\right]\frac{\partial p^{II}}{\partial t} - \lambda(p^{II} - p^I)$ $\frac{\mathrm{v}^{II} k^{II}}{\mu}\Delta p^{II} = \left[\frac{\left(\bar{\alpha}^{II}\right)^2}{\bar{\eta}} + \frac{1}{\bar{M}^{II}}\right]\frac{\partial p^{II}}{\partial t} - \left[\frac{\bar{\alpha}^I\bar{\alpha}^{II}}{\bar{\eta}} + \frac{1}{\bar{M}^{I,II}}\right]\frac{\partial p^I}{\partial t} + \lambda(p^{II} - p^I)$	Considers the flow in matrix
Warren and Root 1963 Ozkan and Raghavan 1991 Houze et al. 1988	$\frac{k^{II}}{\mu}\Delta p^{II} = \phi_m C_{tm}\frac{\partial p^I}{\partial t} + \phi_f C_{tf}\frac{\partial p^{II}}{\partial t}$ $\phi_m C_{tm}\frac{\partial p^I}{\partial t} = \frac{\alpha k^I}{\mu}(p^{II} - p^I)$	Does not consider the flow in matrix
de Swaan 1976 Serra et al. 1983 Aguilera 1987 Chipperfield 2006	$\frac{k^{II}}{\mu}\frac{\partial^2 p^{II}}{\partial r^2} = \phi_f C_{tf}\frac{\partial p^{II}}{\partial t} - q_m\left(p^{II}, t\right)$	Does not consider the flow in matrix

Soliman et al. 2010		

A comparison between the poroelastic formulation used in this paper and the original dual-continuum theory suggested by Barenblatt et al. (1960) suggests that a flow-only model should be capable of generating the results of the poroelastic model presented in this study, provided that the following conditions are simultaneously met:

1. Flow in both matrix and fractures, as well as inter-porosity fluid exchange, in accordance with the original dual-continuum theory of Barenblatt et al. (1960) are accounted for;
2. The rock compressibility, diffusivity, and storage parameters in the governing equation (Eq. 2.1) are selected or calibrated in accordance with the poroelastic definitions of Table 4.4.

Existing publications on the pressure decline analysis, however, only partially fulfill condition 1, and none of which appear to have examined condition 2 above.

4.3 Summary

Three sets of field data are studied in this chapter. In Case Study 1, the hump in the pressure curve and the dip in the pressure derivative curve clearly indicate that a dual-porosity formation is studied. The average permeability of the formation is estimated based on the -1 slope. The -1/2 slope on the log-log pressure derivative curve is not clearly observed, which indicates that the formation permeability is not very low. The newly derived analytical solutions are then used to match the field data. A good match between the two can be found. Consequently, the dual-porosity poroelastic parameters of the formation are estimated. Sensitive analysis shows that the match is sensitive to both matrix and fracture permeability, matrix bulk modulus, Skempton's coefficient

and Biot's coefficient, but not sensitive to fracture bulk modulus, Skempton's coefficient and Biot's coefficient. In cases 2 and 3, the hump in pressure curve is not clear. But the dip behavior in the pressure derivative curves can be clearly observed, which identifies the dual-porosity dual-permeability nature of the formations. The analytical solution of the fracture pressure is able to capture the field data to some extent, based on which the formation poromechanical parameters are estimated. Conventional well test parameters are revisited and the equivalent poroelastic parameters are defined. Such definitions are predominant, since the equivalent poroelastic parameters could be easily determined from well logs or laboratory tests.

Chapter 5 : Conclusions

The dual-porosity dual-permeability poroelastic theory is applied and the analytical line source solutions are derived to simulate and analyze wellbore after-closure pressure decline curves.

In Chapter 2, the poroelastic 2D line source solutions are derived in the Laplace domain for a dual-porosity dual-permeability formation. Then the solutions in the time domain are also derived for the case of no inter-porosity flow. The latter solutions are used to approximate the former ones for pressure derivative curve slope analysis. The slope of 1/2 in the pseudo-linear flow regime, -1/2 in the transient period and -1 in the pseudo-radial flow regime are mathematically described for both matrix and fracture pressure derivative curves. Moreover, it is proved that the -1/2 slope is clearly observed for formations with low permeability. The straight-line behavior in the plot of pressure vs. square time is also mathematically investigated.

In Chapter 3, a numerical example is given to illustrate the wellbore pressure decline during the mini-frac test applied to a shale formation. The slopes of 1/2, -1/2 and -1 are clearly observed to identify the pseudo-linear flow regime, transient period and pseudo-radial flow regime. The effects of inter-porosity flow coefficient are also illustrated. The trough of the pressure derivative curve moves to the right when the inter-porosity flow coefficient decreases. A Mathematical algorithm is also presented to estimate both matrix and fracture permeabilities based on the combination of slopes 1/2 and -1 or the combination of slopes -1/2 and -1. This is important especially when the 1/2 slope in some cases is not obvious. It is also shown that a combination of -1 slope in the log-log plot of pressure derivative curve and the straight line behavior in

the linear plot of pressure vs. square root time allows estimation of matrix permeability, fracture permeability and hydraulic fracture length. Different time markers are also defined to investigate the flow regimes. Such time markers include the upper limit of pseudo-linear flow regime, the time when the dip base of pressure derivative curve occurs and the lower limit of pseudo-radial flow regime. It is found that the inter-porosity flow coefficient plays an essential role in such definitions and can be estimated based on such time markers. Time scales are also defined to study the time when the matrix and fracture systems reach an equilibrium state and the time when the pseudo-radial flow starts.

In Chapter 4, three sets of field data are studied. In case 1, the formation is clearly identified as a dual-porosity dual-permeability formation through the hump in the pressure curve and the trough in the pressure derivative curve. The slopes of -1/2 and -1 can be visibly recognized, which indicates the pseudo-linear flow and the pseudo-radial flow. Since it is a dual-porosity dual-permeability formation, the average permeability of the formation is approximately determined as 0.62 mD base on the -1 slope. To further estimate the dual permeabilities of the formation, the corresponding poroelastic parameters are required. It is noted that the -1/2 slope on the log-log pressure derivative curve is not clearly observed, which indicates that the formation permeability is not very low. This statement is further supported by the estimated average permeability, i.e., 0.62 mD. The set of field data is then further analyzed by matching the newly derived analytical solutions. A good match between the two can be found, based on which the dual-porosisty poroelastic parameters of the formation are determined. Sensitive analysis is also presented to show that the match is sensitive

to both matrix and fracture permeability, matrix bulk modulus, Skempton's coefficient and Biot's coefficient, but not sensitive to fracture bulk modulus, Skempton's coefficient and Biot's coefficient. This sensitive analysis makes it necessary to couple matrix flow in after-closure analysis since the pressure decline is sensitive to matrix permeability and matrix poroelastic parameters. In cases 2 and 3, the hump in pressure curve is not clear. But the dip behavior in the pressure derivative curves can be clearly observed, which identifies the dual-porosity dual-permeability nature of the formations. The analytical solution of the fracture pressure is able to capture the field data to some extent, based on which the formation poromechanical parameters are estimated. Finally, conventional well test parameters are revisited and the equivalent poroelastic parameters are defined. Such definitions are predominant since the equivalent poroelastic parameters could be easily determined from well logs or laboratory tests.

References

Abousleiman, Y. 1991. *A Poroelastic PKN Model with Pressure Dependent Leakoff and Formation Permeability Determination*. PhD dissertation, University of Delaware, Newark, Delaware.

Abousleiman, Y. and Nguyen, V. 2005. Poromechanics Response of Inclined Wellbore Geometry in Fractured Porous Media. *J Eng Mech-ASCE* **131** (11):1170-1183.

Abousleiman, Y., Cheng, A. H-D., Cui, L., Detournay, E., and Roegiers, J.-C. 1996. Mandel's Problem Revisited. *Geotechnique* **46** (2): 187-195.

Abousleiman, Y., Cheng, A. H-D., and Gu, H. 1994. Formation Permeability Determination by Micro or Mini- Hydraulic Fracturing. *J Eng Res Tech* **116** (2): 104–114.

Abousleiman, Y. and Cui, L. 1998. Poroelastic solutions in transversely isotropic media for wellbore and cylinder. *Int J Solids Struct* **35** (34-35): 4905-4929.

Abousleiman, Y., Ekbote, S., and Tare, U. 2000. Time-dependent wellbore (in) stability predictions: theory and case study. Presented at the 2000 IADC/SPE Asia Pacific Drilling Technology, Kuala Lumpur, Malaysia, 11-13 September. IADC/SPE 62796.

Abousleiman, Y., Hoang, S., and Liu, C. 2013. Anisotropic Porothermoelastic Solution and Hydro-Thermal Effects on Fracture Width in Hydraulic Fracturing. *Int J Numer Anal Met* **38** (5):493–517.

Abousleiman, Y., Tran, M., Hoang, S., Bobko C., Ortega, A., and Ulm, F.-J. 2007. Geomechanics Field and Laboratory Characterization of the Woodford Shale: The Next Gas Play. Presented at 2007 SPE Annual Technical Conference and Exhibition, Anaheim, California, 11-14 November. SPE 110120.

Aguilera, R. 1987. Well Test Analysis of Naturally Fractured Reservoirs. *SPE J* **2** (03): 239–252.

Alberty, M. and McLean, M. 2004. A Physical Model for Stress Cages. Presented at SPE Annual Technical Conference and Exhibition, Houston, Texas, 26-29 September. SPE 90493.

Banton, O. and Bangoy, L. 1996. A New Method to Determine Storage Coefficient from Pumping Test Recovery Data. *Groundwater* **34** (5):772–777.

Barenblatt, G., Zheltov, Iu., and Kochina, I. 1960. Basic Concepts in the Theory of Seepage of Homogeneous Liquids in Fissured Rocks [Strata]. *J Appl Mech* **24** (5):1286-1303.

Barree, D. 1998. Applications of Pre-Frac Injection/Falloff Tests in Fissured Reservoirs-Field Examples. Presented at SPE Rocky Mountain Regional/Low-Permeability Reservoirs Symposium, Denver, Colorado, 5-8 April. SPE 39932.

Berryman, J. 2002. Extension of Poroelastic Analysis to Double-Porosity Materials: New Technique in Microgeomechanics. *J Eng Mech-ASCE* **128** (8): 840–847.

Berryman, J. and Pride, S. 2002. Models for Computing Geomechanical Constants of Double-Porosity Materials from the Constituents' Properties. *J Geophys Res* **107** (B3): ECV 2-1-ECV 2-14.

Berryman, J. and Wang, H. 1995. The Elastic Coefficients of Double-Porosity Models for Fluid Transport in Jointed Rock. *J Geophys Res-Sol Ea* **100** (B12): 24611–24627.

Beskos, D. and Aifantis, E. 1986. On the Theory of Consolidation with Double Porosity-II. *Int J Eng Sci* **24** (11): 1697–1716.

Biot, M. 1941. General Theory of Three-Dimensional Consolidation. *J Appl Phys* **12** (2):155-164.

Biot, M. 1955. Theory of Elasticity and Consolidation for a Porous Anisotropic Solid. *J Appl Phys* **26** (2):182-185.

Biot, M. and Willis, D. 1957. The Elastic Coefficients of the Theory of Consolidation. *J Appl Mech* **24**:594-601.

Britt, L., Jones, J., Heidt, J. et al. 2004. Application of After-Closure Analysis Techniques to Determine Permeability in Tight Formation Gas Reservoirs. Presented at the SPE Annual Technical Conference and Exhibition, Houston, Texas, USA, 26–29 September. SPE 90865.

Carslaw, H. and Jaeger, J. 1959. *Conduction of Heat in Solids*. 2nd Edition. Oxford, UK: Oxford Science Publications.

Chipperfield, S. 2005. After-Closure Analysis for Naturally Fractured Reservoirs: Field Examples. Presented at the SPE Annual Technical Conference and Exhibition, Dallas, Texas, USA, 9–12 October. SPE 97015.

Chipperfield, S. 2006. After-Closure Analysis to Identify Naturally Fractured Reservoirs. *SPE J* **9** (01): 50–60.

Chipperfield, S. and Britt, L. 2000. Application of After-Closure Analysis for Improved Fracture Treatment Optimisation: A Cooper Basin Case Study. Presented at the SPE Rocky Mountain Regional/Low Permeability Reservoirs Symposium, Denver, Colorado, USA, 12–15 March. SPE 60316.

Cook, W. 1992. Natural Joints in Rocks: Mechanical, Hydraulic and Seismic Behavior and Properties under Normal Stress. *Int J Rock Mech Min Sci* **29** (3):198-223.

Cooper, H. and Jacob, C. 1946. A Generalized Graphical Method for Evaluating Formation Constants and Summarizing Well-Field History. *Eos, Transactions American Geophysical Union* **27** (4): 526–534.

Coussy, O. 2004. *Poromechanics*. Hoboken, New Jersey: John Wiley & Sons.

Cramer, D. and Nguyen, H. 2013. Diagnostic Fracture Injection Testing Tactics in Unconventional Reservoirs. Presented at the SPE Hydraulic Fracturing Technology Conference, The Woodlands, Texas, 4-6 February. SPE 163863.

Cui, L., Cheng, A. H-D., and Abousleiman, Y. 1997. Poroelastic solution for an inclined borehole. *J Appl Mech* **64** (1): 32–38.

de Swaan, A. 1976. Analytic Solutions for Determining Naturally Fractured Reservoir Properties by Well Testing. *SPE J* **16** (03): 117-122.

Detournay, E., and Cheng, A. H-D. 1988. Poroelastic response of a borehole in a non-hydrostatic stress field. *Int J Rock Mech Min Sci & Geomech Abstr* **25** (3):171-182.

Economides, M. and Nolte, K. 2000. Fracturing Diagnosis Using Pressure Analysis. In *Reservoir Stimulation*, 3rd edition. Hoboken, New Jersey: Wiley.

Ekbote, S. and Abousleiman, Y. 2005. Porochemothermoelastic solution for an inclined borehole in a transversely isotropic formation. *J Eng Mech* **131** (5): 522-533.

Ekbote, S. and Abousleiman, Y. 2006. Porochemoelastic solution for an inclined borehole in a transversely isotropic formation. *J Eng Mech* **132** (7): 754-763.

Eliyahu, M., Emmanuel, S., Day-Stirrat, R., and Macaulay, C. 2015. Mechanical Properties of Organic Matter in Shales Mapped at the Nanometer Scale. *Mar Petrol Geol* **59**:294-304.

Farlow, S. 1982. *Partial Differential Equations for Scientists and Engineers*. New York: Wiley.

Freeze, R. and Cherry, J. 1979. *Groundwater*. Englewood Cliffs, New Jersey: Prentice-Hall.

Gambolati, G. 1974. Second-Order Theory of Flow in Three-Dimensional Deforming Media. *Water Resour Res* **10** (06): 1217-1228.

Ge, J., and Ghassemi, A. 2008. Analysis of Failure Potential around a Hydraulic Fracture in Jointed Rock. Presented at the 42th US Rock Mechanics Symposium, San Francisco, CA, USA, 29 June-2 July. ARMA 08-252.

Geertsma, J. 1973. Land Subsidence above Compacting Oil and Gas Reservoirs. *J Petrol Technol* **25** (06):734-744.

Gelet, R., Loret, B., and Khalili, N. 2012. Borehole stability analysis in a thermoporoelastic dual-porosity medium. *Int J Rock Mech Min Sci* **50**: 65-76.

Ghassemi, A., Zhou, X., and Rawal, C. 2010. 3D Poroelastic Analysis of Rock Failure around a Hydraulic Fracture. Presented at the 44th US Rock Mechanics Symposium, Salt Lake City, UT, USA, 27-30 June. ARMA 10-506.

Gu, H., Elbel, J., Nolte, K. et al. 1993. Formation Permeability Determination Using Impulse-Fracture Injection. Presented at the Production Operations Symposium, Oklahoma City, Oklahoma, USA, 21–23 March. SPE 25425.

Hall, N. 1953. Compressibility of Reservoir Rocks. *J Petrol Tech* **5** (01): 309-311.

Hart, J. and Wang, F. 1995. Laboratory Measurements of a Complete Set of Poroelastic Moduli for Berea Sandstone and Indiana Limestone. *J Geophy Res-Sol Ea* **100** (B9): 17741-17751.

Houze, O., Horne, R., and Ramey, H., Jr. 1988. Pressure-Transient Response of an Infinite-Conductivity Vertical Fracture in a Reservoir with Double-Porosity Behavior. *SPE Formation Evaluation* **3** (03): 510–518.

Kazemi, H, Merrill, L, Porterfield, K., Zeman, P. 1976. Numerical simulation of water-oil flow in naturally fractured reservoirs. *SPE J* **16** (6):317-326.

Kuhlman, D. 1990. Microfrac Tests Optimize Frac Jobs. *Oil & Gas Journal* January: 45–49.

Lee, J., Rollins, J., and Spivey, J. 2003. *Pressure Transient Testing*. SPE Textbook Series, Vol. 9. Richardson, Texas: SPE.

Lewallen, K. and Wang, H. 1998. Consolidation of a double-porosity medium. *Int J Solids Struc* **35** (34-35): 4845-4867.

Li, X. 2003. Consolidation around a borehole embedded in media with double porosity under release of geostatic stresses. *Mech Res Commun* **30** (1): 95-100.

Mader, D. 1989. *Hydraulic Proppant Fracturing and Gravel Packing*. Amsterdam, The Netherlands: Elsevier.

Mandel, J. 1953. Consolidation des Sols étude Mathématique. *Geotechnique* **3** (7):287-299.

McCain, W. 1990. *The Properties of Petroleum Fluids*. Tulsa, Oklahoma: PennWell Corp.

McClure, W., Jung, H., Cramer, D., and Sharma, M. 2016. The Fracture –Compliance Method for Picking Closure Pressure from Diagnostic Fracture-Injection Tests. *SPE J*. SPE-179725-PA (in press; posted February 2016).

Mehrabian, A. 2016. The Stability of Inclined and Fractured Wellbores. *SPE J*. SPE-180910-PA (in press; posted March 2016).

Mehrabian, A. and Abousleiman, Y. 2009. The Dilative Intake of Poroelastic Inclusions an Alternative to the Mandel-Cryer Effect. *Acta Geotech* **4** (4): 249-259.

Mehrabian, A. and Abousleiman, Y. 2014. Generalized Biot's Theory and Mandel's Problem of Multiple-Porosity and Multiple-Permeability Poroelasticity. *J Geophys Res-Solid Ea* **119** (4): 2745–2763.

Mehrabian, A. and Abousleiman, Y. 2015a. Gassmann Equations and the Constitutive Relations for Multiple-Porosity and Multiple-Permeability Poroelasticity with Applications to Oil and Gas Shale. *Int J Numer Anal Meth Geomech* **39** (14):1547-1569.

Mehrabian, A. and Abousleiman, Y. 2015b. Geertsma's Subsidence Solution Extended to Layered Stratigraphy. *J Petrol Sci Eng* **130**:68-76.

Mehrabian, A. and Abousleiman, Y. 2016. Wellbore Geomechanics of Extended Drilling Margins and Engineered Lost Circulation Solutions. ARMA 16-457.

Mehrabian, A., Jamison, D., and Teodorescu, S. 2015. Geomechanics of Lost-Circulation Events and Wellbore-Strengthening Operations. *SPE J* **20** (6):1305-1316.

Nguyen, V. 2010. Dual-Porosity and Dual-Permeability Poromechanics Solutions for Problems in Laboratory and Field Applications. PhD dissertation. University of Oklahoma, Norman, Oklahoma.

Nguyen, V. and Abousleiman, Y. 2009. Poromechanics response of inclined wellbore geometry in chemically active fractured porous media. *J Eng Mech* **135** (11):1281-1294.

Nguyen, V. and Abousleiman, Y. 2010a. Incorporating electrokinetic effects in the porochemoelastic inclined wellbore formulation and solution. *Anais da Academia Brasileira de Ciências*. **82** (1): 195-222. ISSN 0001-3765.

Nguyen, V. and Abousleiman, Y. 2010b. Poromechanics Solutions to Plane Strain and Axisymmetric Mandel-Type Problems in Dual-Porosity and Dual-Permeability Medium. *J Appl Mech* **77** (01), 011002: 1–18.

Nguyen, V., Abousleiman, Y., Hoang, S. 2009. Analyses of wellbore instability in drilling through chemically active fractured-rock formations. *SPE J* **14** (02): 283-301.

Nolte, K. 1979. Determination of Fracture Parameters from Fracturing Pressure Decline. Presented at the SPE Annual Technical Conference and Exhibition, Las Vegas, Nevada, USA, 23–26 September. SPE 8341.

Nolte, K. 1988. Principles for Fracture Design Based on Pressure Analysis. *SPE Production Engineering*. **3** (01):22-30.

Nolte, K., Maniere, J., and Owens, K. 1997. After-Closure Analysis of Fracture Calibration Tests. Presented at the SPE Annual Technical Conference and Exhibition, San Antonio, Texas, USA, 5–8 October. SPE 38676.

Nolte, K. and Smith, M. 1981. Interpretation of Fracturing Pressures. *SPE J* **33** (09): 1767–1775.

Nordgren, P. 1972. Propagation of a Vertical Hydraulic Fracture. *SPE J* **12** (04):306-314.

Nunes, M., Bedrikovetsky, P., Newbery, B. et al. 2010. Theoretical Definition of Formation Damage Zone with Applications to Well Stimulation. *J Eng Res Tech* **132** (3), 033101: 1–7.

Ozkan, E. and Raghavan, R. 1991. New Solutions for Well-Test-Analysis Problems: Part 1-Analytical Considerations. *SPE Formation Evaluation* **6** (03): 359–368.

Penny, G., Conway, M., and Lee, W. 1985. Control and Modeling of Fluid Leakoff during Hydraulic Fracturing. *J Pet Technol* **37** (06): 1071-1081.

Rice, J. and Cleary, M. 1976. Some Basic Stress Diffusion Solutions for Fluid-Saturated Elastic Porous Media with Compressible Constituents. *Rev Geophys Space Phys* **14** (2):227-241.

Serra, K. Reynolds, A. and Raghavan, R. 1983. New Pressure Transient Analysis Methods for Naturally Fractured Reservoirs. *J Petrol Tech* **35** (12): 2271-2283

Slatt, R. and Abousleiman, Y. 2011. Merging Sequence Stratigraphy and Geomechanics for Unconventional Gas Shales. *The Leading Edge*. **30** (3):274-282.

Slatt, R. and O'Brien, N. 2011. Pore Types in the Barnett and Woodford Gas Shales: Contribution to Understanding Gas Storage and Migration Pathways in Fine-Grained Rocks. *AAPG Bulletin*. **95** (12):2017-2030.

Soliman, M., Craig, D., Bartko, K. et al. 2005. Post-Closure Analysis to Determine Formation Permeability, Reservoir Pressure, and Residual Fracture Properties. Presented at the 14th SPE Middle East Oil & Gas Show and Conference, Bahrain, 12–15 March. SPE 93419.

Soliman, M., Miranda, C., and Wang, H. 2010. Application of After-Closure Analysis to a Dual-Porosity Formation, to CBM, and to a Fractured Horizontal Well. *SPE J* **25** (04): 472–483.

Sonier, F., Souillard, P., Blaskovich, F. 1988. Numerical simulation of naturally fractured reservoirs. *SPE Reservoir Engineering* **3** (4):1114-1122.

Stewart, G. and Ascharsobbi, F. 1988. Well Test Interpretation for Naturally Fractured Reservoirs. Presented at the 63rd SPE Annual Technical Conference and Exhibition, Houston, Texas, USA, 2–5 October. SPE-18173.

Talley, G., Swindell, T., Waters, G. et al. 1999. Field Application of After-Closure Analysis of Fracture Calibration Tests. Presented at the SPE Mid-Continent Operations Symposium, Oklahoma City, Oklahoma, USA, 28–31 March. SPE 52220.

Tran, M., Abousleiman, Y., and Nguyen, V. 2011. The Effects of Filter-Cake Buildup and Time-Dependent Properties on the Stability of Inclined Wellbores. *SPE J* **16** (04): 1010-1028.

Uribe, O., Chipperfield, S., Tiab, D. et al. 2007. Advances in After-Closure Analysis for Naturally Fractured Reservoirs. Presented at the SPE Latin American and Caribbean Petroleum Engineering Conference, Buenos Aires, Argentina, 15–18 April. SPE 107257.

Uribe, O., Tiab, D., and Restrepo, D.P. 2008. Interpretation of After Closure Tests in Naturally Fractured Reservoirs. *Dyna rev fac nac minas* **75** (155): 211–222.

Verruijt, A. 1969. Elastic Storage of Aquifers, in Flow through Porous Media, edited by DeWlest M. 331-376, Academic, New York.

Wang, H. 2000. *Theory of Linear Poroelasticity with Applications to Geomechanics and Hydrogeology*. Princeton, New Jersey: Princeton University Press.

Warpinski, R. 1985. Measurement of Width and Pressure in a Propagating Hydraulic Fracture. *SPE J* **25** (01):46-54.

Warpinski, N., Wolhart, S., and Wright, C. 2004. Analysis and Prediction of Microseismicity Induced by Hydraulic Fracturing. *SPE J* **9** (01):24-33.

Warren, J. and Root, P. 1963. The Behavior of Naturally Fractured Reservoirs. *SPE J* **3** (3): 245–255.

Wilson, R. and Aifantis, E. 1982. On the Theory of Consolidation with Double Porosity. *Int J Eng Sci* **20** (9): 1009–1035.

Zimmerman, R., Chen, G., Hadgu, T., and Bodvarsson, G. 1993. A Numerical Dual-Porosity Model with Semianalytical Treatment of Fracture/Matrix Flow. *Water Resour Res* **29** (7):2127-2137.

Appendix A: After-Closure Wellbore Pressure Solution Considering Inter-Porosity Flow

Instantaneous Point Source Solution. In this section, the pressure influence solution resulting from an instantaneous point source with a unit fluid volume injection in a plane with single porosity and single permeability (Carslaw and Jaeger 1959; Abousleiman et al. 1994) is extended to the dual-porosity dual-permeability case.

Combining the constitutive Eq. 1.11 with the stress equilibrium equation (Eq. 1.14) and strain-displacement relations (Eq. 1.18), the following Navier's equation can be derived:

$$\left(\overline{K}+\frac{4}{3}\overline{G}\right)\nabla(\nabla\cdot u)-\overline{G}\nabla\times(\nabla\times u)+\overline{\alpha}^{I}\nabla p^{I}+\overline{\alpha}^{II}\nabla p^{II}=0 \quad \text{..... (A-1)}$$

In this problem, the displacement field is irrotational because it is assumed to be radial; therefore, the following equation can be obtained: $\nabla\times u=0$, and substituting it into Eq. A-1 provides

$$\left(\overline{K}+\frac{4}{3}\overline{G}\right)\nabla(\nabla\cdot u)+\overline{\alpha}^{I}\nabla p^{I}+\overline{\alpha}^{II}\nabla p^{II}=0 \quad \text{..... (A-2)}$$

Using the fact that $\nabla\cdot u=\varepsilon$ and integrating Eq. A-2, the following equation can be obtained:

$$\varepsilon=-\frac{\overline{\alpha}^{I}}{\overline{K}+\frac{4}{3}\overline{G}}p^{I}-\frac{\overline{\alpha}^{II}}{\overline{K}+\frac{4}{3}\overline{G}}p^{II}+f(t) \quad \text{..... (A-3)}$$

where *f*(*t*) is an integration function only dependent on time.

Furthermore, because the domain studied here is infinite, and all of the strain and pore pressures must vanish at infinity, it is obtained that $f(t)\equiv 0$, or

$$\varepsilon = -\frac{\overline{\alpha}^{I}}{\overline{K} + \frac{4}{3}\overline{G}} p^{I} - \frac{\overline{\alpha}^{II}}{\overline{K} + \frac{4}{3}\overline{G}} p^{II} \quad \text{(A-4)}$$

which is an extension of Eq. 5.24 from Coussy (2004).

Combining Eq. A-4 with the constitutive equations (Eqs. 2 and 3) provides

$$\zeta^{I} = \left(\frac{\left(\overline{\alpha}^{I}\right)^2}{\overline{\eta}} + \frac{1}{\overline{M}^{I}} \right) p^{I} + \left(\frac{\overline{\alpha}^{I}\overline{\alpha}^{II}}{\overline{\eta}} + \frac{1}{\overline{M}^{I,II}} \right) p^{II} \quad \text{(A-5)}$$

$$\zeta^{II} = \left(\frac{\overline{\alpha}^{I}\overline{\alpha}^{II}}{\overline{\eta}} + \frac{1}{\overline{M}^{I,II}} \right) p^{I} + \left(\frac{\left(\overline{\alpha}^{II}\right)^2}{\overline{\eta}} + \frac{1}{\overline{M}^{II}} \right) p^{II} \quad \text{(A-6)}$$

which can be written in the matrix form

$$\begin{bmatrix} \zeta^{I} \\ \zeta^{II} \end{bmatrix} = A \begin{bmatrix} p^{I} \\ p^{II} \end{bmatrix} \quad \text{(A-7)}$$

where

$$A = \begin{bmatrix} \frac{\left(\overline{\alpha}^{I}\right)^2}{\overline{\eta}} + \frac{1}{\overline{M}^{I}} & \frac{\overline{\alpha}^{I}\overline{\alpha}^{II}}{\overline{\eta}} + \frac{1}{\overline{M}^{I,II}} \\ \frac{\overline{\alpha}^{I}\overline{\alpha}^{II}}{\overline{\eta}} + \frac{1}{\overline{M}^{I,II}} & \frac{\left(\overline{\alpha}^{II}\right)^2}{\overline{\eta}} + \frac{1}{\overline{M}^{II}} \end{bmatrix} \quad \text{(A-8)}$$

and $\overline{\eta} = \overline{K} + 4\overline{G}/3$.

Substituting the Darcy's flow equations (Eq. 1.16) into the mass balance equations (Eq. 1.15), the following is obtained:

$$\frac{\partial \zeta^{I}}{\partial t} = \frac{\mathrm{v}^{I} k^{I}}{\mu} \nabla^2 p^{I} + \lambda\left(p^{II} - p^{I}\right) \quad \text{(A-9)}$$

$$\frac{\partial \zeta^{II}}{\partial t} = \frac{\mathrm{v}^{II} k^{II}}{\mu} \nabla^2 p^{II} - \lambda\left(p^{II} - p^{I}\right) \quad \text{(A-10)}$$

The above equations can be rearranged and presented in the following matrix form:

$$\frac{\partial}{\partial t}\begin{bmatrix}\zeta^{I}\\ \zeta^{II}\end{bmatrix} = D\nabla^{2}\begin{bmatrix}p^{I}\\ p^{II}\end{bmatrix} + \Gamma\begin{bmatrix}p^{I}\\ p^{II}\end{bmatrix} \quad \text{..... (A-11)}$$

where

$$D = \begin{bmatrix}\dfrac{\mathrm{v}^{I}k^{I}}{\mu} & 0\\ 0 & \dfrac{\mathrm{v}^{II}k^{II}}{\mu}\end{bmatrix} \quad \text{..... (A-12)}$$

$$\Gamma = \lambda\begin{bmatrix}-1 & 1\\ 1 & -1\end{bmatrix} \quad \text{..... (A-13)}$$

Substituting Eq. A-7 into Eq. A-11 provides

$$\frac{\partial}{\partial t}\begin{bmatrix}\zeta^{I}\\ \zeta^{II}\end{bmatrix} = DA^{-1}\nabla^{2}\begin{bmatrix}\zeta^{I}\\ \zeta^{II}\end{bmatrix} + \Gamma A^{-1}\begin{bmatrix}\zeta^{I}\\ \zeta^{II}\end{bmatrix} \quad \text{..... (A-14)}$$

Applying the Laplace transform to Eq. A-14 and using the fact that $\zeta^{I}(t=0^{+}) = \zeta^{II}(t=0^{+}) = 0$ at $r > 0$, Eq. A-14 can be rewritten in the Laplace domain as follows:

$$\nabla^{2}\begin{bmatrix}\tilde{\zeta}^{I}\\ \tilde{\zeta}^{II}\end{bmatrix} = AD^{-1}(sI - \Gamma A^{-1})\begin{bmatrix}\tilde{\zeta}^{I}\\ \tilde{\zeta}^{II}\end{bmatrix} \quad \text{..... (A-15)}$$

where the operator ∇^{2} can be expressed in the polar coordinates as follows:

$$\nabla^{2} = \frac{1}{r}\frac{\partial}{\partial r} + \frac{\partial^{2}}{\partial r^{2}} + \frac{1}{r^{2}}\frac{\partial^{2}}{\partial \theta^{2}} \quad \text{..... (A-16)}$$

Because of the symmetry of the problem, Equation A-16 is further simplified as

$$\nabla^{2} = \frac{1}{r}\frac{\partial}{\partial r} + \frac{\partial^{2}}{\partial r^{2}} \quad \text{..... (A-17)}$$

The ordinary differential equation (Eq. A-15) can be solved using the method given in Lesson 29 of Farlow (1982). The solution is written in the following matrix form:

$$\begin{bmatrix} \tilde{\zeta}^{I} \\ \tilde{\zeta}^{II} \end{bmatrix} = P \begin{bmatrix} C^{I} K_0(\sqrt{\lambda^{I} r}) \\ C^{II} K_0(\sqrt{\lambda^{II} r}) \end{bmatrix} \quad \text{(A-18)}$$

where the matrix P satisfies the following condition:

$$P^{-1} A D^{-1} \left(sI - \Gamma A^{-1} \right) P = \begin{bmatrix} \lambda^{I} & 0 \\ 0 & \lambda^{II} \end{bmatrix} \quad \text{(A-19)}$$

and is denoted by

$$P = \begin{bmatrix} m_{11}^{I} & m_{12}^{II} \\ m_{21}^{I} & m_{22}^{II} \end{bmatrix} \quad \text{(A-20)}$$

where $K_0(x)$ is the modified Bessel function of the second kind and the constants C^I and C^{II} are to be determined.

Substitution of Eq. A-18 into Eq. A-7 provides the instantaneous point source solution of pore pressure in the Laplace domain:

$$\begin{bmatrix} \tilde{p}_{\text{inst,point}}^{I} \\ \tilde{p}_{\text{inst,point}}^{II} \end{bmatrix} = A^{-1} P \begin{bmatrix} C^{I} K_0(\sqrt{\lambda^{I} r}) \\ C^{II} K_0(\sqrt{\lambda^{II} r}) \end{bmatrix} \quad \text{(A-21)}$$

where the matrix $A^{-1}P$ can be denoted by

$$A^{-1} P = \begin{bmatrix} n_{11}^{I} & n_{12}^{II} \\ n_{21}^{I} & n_{22}^{II} \end{bmatrix} \quad \text{(A-22)}$$

To obtain the expressions of the coefficients C^I and C^{II}, consider a unit fluid volume is injected instantaneously at the origin of the infinite plane; the solutions provided by Eq. A-21 must satisfy the instantaneous injection condition:

at any t: $\int_0^\infty \left(\zeta^I + \zeta^{II}\right) 2\pi r dr = 1$ ..... (A-23)

Applying the Laplace transform to the above equation, the following equation is obtained:

$$\int_0^\infty \left(\tilde{\zeta}^I + \tilde{\zeta}^{II}\right) r dr = \frac{1}{2\pi s} \quad \text{..... (A-24)}$$

Substituting the solution (Eq. A-21) into Eq. A-24 provides

$$\left(m_{11}^I + m_{21}^I\right)\frac{C^I}{\lambda^I} + \left(m_{12}^{II} + m_{22}^{II}\right)\frac{C^{II}}{\lambda^{II}} = \frac{1}{2\pi s} \quad \text{..... (A-25)}$$

Furthermore, when the unit fluid volume is injected instantaneously at the origin, the amount of fluid volume is assumed to be distributed in both the matrix and fracture at a ratio of $v^I : v^{II}$, or

for any R: $\int_0^R \zeta^I 2\pi r dr\,|_{t\to 0^+} = v^I$; $\int_0^R \zeta^{II} 2\pi r dr\,|_{t\to 0^+} = v^{II}$ ..... (A-26)

Especially when setting $R = \infty$, the following is obtained:

$$\int_0^\infty \zeta^I r dr\,|_{t\to 0^+} = \frac{v^I}{2\pi}; \int_0^\infty \zeta^{II} r dr\,|_{t\to 0^+} = \frac{v^{II}}{2\pi} \quad \text{..... (A-27)}$$

Using the fact that $\lim_{t\to 0} f(t) = \lim_{s\to\infty} sF(s)$ and the solution (Eq. A-21), the following two equations are obtained:

$$\lim_{s\to\infty}\left(sm_{11}^I \frac{C^I}{\lambda^I} + sm_{12}^{II}\frac{C^{II}}{\lambda^{II}}\right) = \frac{v^I}{2\pi} \quad \text{..... (A-28)}$$

$$\lim_{s\to\infty}\left(sm_{21}^I \frac{C^I}{\lambda^I} + sm_{22}^{II}\frac{C^{II}}{\lambda^{II}}\right) = \frac{v^{II}}{2\pi} \quad \text{..... (A-29)}$$

Note that the three equations (Eqs. A-25, A-28, and A-29) are not independent. Eq. A-29 can be derived from Eqs. A-25 and A-28, and Eq. A-28 can be derived from Eqs.

A-25 and A-29. Thus, combining either Eqs. A-28 or A-29 with Eq. A-25 (Eq. A-28 is used in this example) provides the expressions C^I and C^{II}:

$$\begin{pmatrix} C^I \\ C^{II} \end{pmatrix} = \frac{1}{2\pi} \begin{pmatrix} b_{11}^I & b_{12}^{II} \\ \dfrac{m_{11}^I + m_{21}^I}{\lambda^I} & \dfrac{m_{12}^{II} + m_{22}^{II}}{\lambda^{II}} \end{pmatrix}^{-1} \begin{pmatrix} \mathrm{v}^I \\ \dfrac{1}{s} \end{pmatrix} \quad \text{..... (A-30)}$$

where $b_{11}^I = \lim_{s\to\infty} \dfrac{sm_{11}^I}{\lambda^I}$ and $b_{12}^I = \lim_{s\to\infty} \dfrac{sm_{12}^{II}}{\lambda^{II}}$.

Instantaneous Line Source Solution. Consider an instantaneous line source with a uniform intensity and a length, 2*L*. The matrix pore pressure at an arbitrary point (*x*,*y*) can be obtained by integrating the previously discussed point source solution:

$$p_{\text{inst,line}}^I(x,y,t) = \int_{-L}^{L} p_{\text{inst,point}}^I(r,t)dx' \quad \text{..... (A-31)}$$

where $r = \sqrt{(x-x')^2 + y^2}$.

Applying the Laplace transform with both sides of the above formula provide

$$\tilde{p}_{\text{inst,line}}^I(x,y) = \int_{-L}^{L} \tilde{p}_{\text{inst,point}}^I(r)dx' \quad \text{..... (A-32)}$$

or

$$\tilde{p}_{\text{inst,line}}^I(x,y) = 2\int_0^L \left[n_{11}^I C^I K_0(\sqrt{\lambda^I}\, r) + n_{12}^{II} C^{II} K_0(\sqrt{\lambda^{II}}\, r) \right] dx' \quad \text{..... (A-33)}$$

Especially at the origin (0,0), the following is obtained:

$$\tilde{p}_{\text{inst,line}}^I(0,0) = 2\int_0^L \left[n_{11}^I C^I K_0(\sqrt{\lambda^I}\, x') + n_{12}^{II} C^{II} K_0(\sqrt{\lambda^{II}}\, x') \right] dx' \quad \text{..... (A-34)}$$

The integration in Eq. A-34 can be calculated using Mathematica software, which provides the instantaneous line source solution of matrix pore pressure at the origin as follows:

$$\tilde{p}^{I}_{\text{inst,line}}(0,0) = \pi L\left\{n^{I}_{11}C^{I}\left[K_0(\sqrt{\lambda^{I}}L)L_{-1}(\sqrt{\lambda^{I}}L)+K_1(\sqrt{\lambda^{I}}L)L_0(\sqrt{\lambda^{I}}L)\right]\right.$$
$$\left.+\,n^{II}_{12}C^{II}\left[K_0(\sqrt{\lambda^{II}}L)L_{-1}(\sqrt{\lambda^{II}}L)+K_1(\sqrt{\lambda^{II}}L)L_0(\sqrt{\lambda^{II}}L)\right]\right\} \quad \text{..... (A-35)}$$

where $L_{-1}(x)$ and $L_0(x)$ are modified Struve functions of order -1 and 0, respectively.

Similarly, the instantaneous line source solution of fracture pore pressure at the origin can be obtained as follows:

$$\tilde{p}^{II}_{\text{inst,line}}(0,0) = \pi L\left\{n^{I}_{21}C^{I}\left[K_0(\sqrt{\lambda^{I}}L)L_{-1}(\sqrt{\lambda^{I}}L)+K_1(\sqrt{\lambda^{I}}L)L_0(\sqrt{\lambda^{I}}L)\right]\right.$$
$$\left.+\,n^{II}_{22}C^{II}\left[K_0(\sqrt{\lambda^{II}}L)L_{-1}(\sqrt{\lambda^{II}}L)+K_1(\sqrt{\lambda^{II}}L)L_0(\sqrt{\lambda^{II}}L)\right]\right\} \quad \text{..... (A-36)}$$

Continuous Line Source Solution. Now, consider a continuous line source with a uniform intensity along length 2L and of time t. The matrix pore pressure at the origin can be obtained by integrating the instantaneous line source solution (Eq. A-35):

$$p^{I}_{\text{cont,line}}(t) = \int_0^t p^{I}_{\text{inst,line}}(t-t')dt' = \int_0^t p^{I}_{\text{inst,line}}(t')dt' \quad \text{..... (A-37)}$$

Using the formula

$$\mathcal{L}\left\{\int_0^t f(\tau)d\tau\right\} = \frac{1}{s}\mathcal{L}\{f(t)\} \quad \text{..... (A-38)}$$

and substituting Eq. A-35 into Eq. A-37, the continuous line source solution of the matrix pore pressure at the origin can be expressed in the Laplace domain as follows:

$$\tilde{p}^{I}_{\text{cont,line}} = \frac{\pi L}{s}\left\{n^{I}_{11}C^{I}\left[K_0(\sqrt{\lambda^{I}}L_e)L_{-1}(\sqrt{\lambda^{I}}L_e)+K_1(\sqrt{\lambda^{I}}L_e)L_0(\sqrt{\lambda^{I}}L_e)\right]\right.$$
$$\left.+\,n^{II}_{12}C^{II}\left[K_0(\sqrt{\lambda^{II}}L_e)L_{-1}(\sqrt{\lambda^{II}}L_e)+K_1(\sqrt{\lambda^{II}}L_e)L_0(\sqrt{\lambda^{II}}L_e)\right]\right\} \quad \text{..... (A-39)}$$

Similarly, the continuous line source solution of the fracture pore pressure at the origin in the Laplace domain is

$$\tilde{p}^{II}_{\text{cont,line}} = \frac{\pi L}{s}\left\{n^{I}_{21}C^{I}\left[K_0(\sqrt{\lambda^{I}}L_e)L_{-1}(\sqrt{\lambda^{I}}L_e)+K_1(\sqrt{\lambda^{I}}L_e)L_0(\sqrt{\lambda^{I}}L_e)\right]\right.$$
$$\left.+\,n^{II}_{22}C^{II}\left[K_0(\sqrt{\lambda^{II}}L_e)L_{-1}(\sqrt{\lambda^{II}}L_e)+K_1(\sqrt{\lambda^{II}}L_e)L_0(\sqrt{\lambda^{II}}L_e)\right]\right\} \quad \text{..... (A-40)}$$

Finite Interval Line Source Solution. The finite interval line source solution is used to simulate the matrix and fracture pore pressures at the wellbore after fracture closure. Based on the previous source solutions, the after-closure solutions (matrix: $p^{I}_{\text{line,w}}$; fracture: $p^{II}_{\text{line,w}}$) resulting from an injection of a volume of $Q_0 t_p$ for a finite duration tc are expressed as follows:

$$p^{I}_{\text{line,w}}(\Delta t) = \frac{Q_0 t_p}{2HL_e t_c}\left[p^{I}_{\text{cont,line}}(t_c+\Delta t) - p^{I}_{\text{cont,line}}(\Delta t)\right] \quad \text{..... (A-41)}$$

$$p^{II}_{\text{line,w}}(\Delta t) = \frac{Q_0 t_p}{2HL_e t_c}\left[p^{II}_{\text{cont,line}}(t_c+\Delta t) - p^{II}_{\text{cont,line}}(\Delta t)\right] \quad \text{..... (A-42)}$$

where Δt is the after-fracture-closure time, H is the fracture height, and $2L_e$ is the equivalent fracture length, which is expected to be longer than the actual maximum fracture length.

Appendix B: After-Closure Pressure Analysis

Pseudo-Linear Period. Substitution of Eq. A-7 into Eq. A-11 provides the governing equation of pressure:

$$\frac{\partial}{\partial t}\begin{bmatrix} p^I \\ p^{II} \end{bmatrix} = A^{-1}D\nabla^2\begin{bmatrix} p^I \\ p^{II} \end{bmatrix} + A^{-1}\Gamma\begin{bmatrix} p^I \\ p^{II} \end{bmatrix} \quad \text{..... (B-1)}$$

Multiplying both sides of the Equation B-1 by $-t$ provides

$$-t\frac{\partial}{\partial t}\begin{bmatrix} p^I \\ p^{II} \end{bmatrix} = -tA^{-1}D\nabla^2\begin{bmatrix} p^I \\ p^{II} \end{bmatrix} - tA^{-1}\Gamma\begin{bmatrix} p^I \\ p^{II} \end{bmatrix} \quad \text{..... (B-2)}$$

because $t\rightarrow 0^+$ (i.e., in the pseudo-linear flow regime, the pressure derivatives have the following asymptotic behavior):

$$-t\frac{dp^I}{dt} = O(t^{1/2})\,;\; -t\frac{dp^{II}}{dt} = O(t^{1/2}) \quad \text{..... (B-3)}$$

which is shown in Figure 3.1.

Furthermore, when $t\rightarrow 0^+$, both p^I and p^{II} are finite. As a result, the last term of Eq. 12 has a higher infinitesimal $O(t)$, which implies that the governing equation for $-t\partial p^I/\partial t$ and $-t\partial p^{II}/\partial t$ can be approximated by the following equation:

$$-t\frac{\partial}{\partial t}\begin{bmatrix} p^I \\ p^{II} \end{bmatrix} = -tA^{-1}D\nabla^2\begin{bmatrix} p^I \\ p^{II} \end{bmatrix} \quad \text{..... (B-4)}$$

or

$$\frac{\partial}{\partial t}\begin{bmatrix} p^I \\ p^{II} \end{bmatrix} = A^{-1}D\nabla^2\begin{bmatrix} p^I \\ p^{II} \end{bmatrix} \quad \text{..... (B-5)}$$

which is the without-inter-porosity-flow case.

Because the solutions provided in Appendix A are in the Laplace domain, it can be tedious to directly investigate the asymptotic behaviors of $-t\partial p^I/\partial t$ and $-t\partial p^{II}/\partial t$ at $t\rightarrow 0$.

Fortunately, with the previous analysis, they can be approximated using the solutions of the without-inter-porosity-flow case ,which can be obtained in the time domain.

The solutions of the without-inter-porosity-flow case are provided in Appendix C as follows:

$$\begin{bmatrix} \bar{p}^{I}_{\mathrm{line,w}}(\Delta t) \\ \bar{p}^{II}_{\mathrm{line,w}}(\Delta t) \end{bmatrix} = \frac{Q_0 t_p}{4\pi H t_c} \begin{bmatrix} \bar{n}^{I}_{11}\bar{\lambda}^{I} & \bar{n}^{II}_{12}\bar{\lambda}^{II} \\ \bar{n}^{I}_{21}\bar{\lambda}^{I} & \bar{n}^{II}_{22}\bar{\lambda}^{II} \end{bmatrix} \cdot \begin{bmatrix} \bar{C}^{I}\left\{ \frac{2\sqrt{\pi(t_c+\Delta t)}}{\sqrt{\bar{\lambda}^{I}}L_e} Erf\left(\frac{\sqrt{\bar{\lambda}^{I}}L_e}{2\sqrt{(t_c+\Delta t)}} \right) - \frac{2\sqrt{\pi\Delta t}}{\sqrt{\bar{\lambda}^{I}}L_e} Erf\left(\frac{\sqrt{\bar{\lambda}^{I}}L_e}{2\sqrt{\Delta t}} \right) + E_1\left(\frac{\bar{\lambda}^{I}L_e^2}{4(t_c+\Delta t)} \right) - E_1\left(\frac{\bar{\lambda}^{I}L_e^2}{4\Delta t} \right) \right\} \\ \bar{C}^{II}\left\{ \frac{2\sqrt{\pi(t_c+\Delta t)}}{\sqrt{\bar{\lambda}^{II}}L_e} Erf\left(\frac{\sqrt{\bar{\lambda}^{II}}L_e}{2\sqrt{(t_c+\Delta t)}} \right) - \frac{2\sqrt{\pi\Delta t}}{\sqrt{\bar{\lambda}^{II}}L_e} Erf\left(\frac{\sqrt{\bar{\lambda}^{II}}L_e}{2\sqrt{\Delta t}} \right) + E_1\left(\frac{\bar{\lambda}^{II}L_e^2}{4(t_c+\Delta t)} \right) - E_1\left(\frac{\bar{\lambda}^{II}L_e^2}{4\Delta t} \right) \right\} \end{bmatrix} \quad \text{..... (B-7)}$$

where the symbol bar stands for the without-inter-porosity-flow case.

It is easy to check that, during the pseudo-linear flow period when $\Delta t \rightarrow 0^{+}$, the solutions provided by Eq. B-7 have the following asymptotic behaviors:

$$\begin{aligned} \bar{p}^{I}_{\mathrm{line,w}}(\Delta t) \rightarrow & \frac{Q_0 t_p \bar{n}^{I}_{11}\bar{C}^{I}\lambda^{I}}{4\pi H t_c}\left[\frac{2\sqrt{\pi t_c}}{\sqrt{\bar{\lambda}^{I}}L_e} Erf\left(\frac{\sqrt{\bar{\lambda}^{I}}L_e}{2\sqrt{t_c}} \right) + E_1\left(\frac{\bar{\lambda}^{I}L_e^2}{4t_c} \right) \right] \\ & + \frac{Q_0 t_p \bar{n}^{II}_{12}\bar{C}^{II}\bar{\lambda}^{II}}{4\pi H t_c}\left[\frac{2\sqrt{\pi t_c}}{\sqrt{\bar{\lambda}^{II}}L_e} Erf\left(\frac{\sqrt{\bar{\lambda}^{II}}L_e}{2\sqrt{t_c}} \right) + E_1\left(\frac{\bar{\lambda}^{II}L_e^2}{4t_c} \right) \right] \quad \text{..... (B-8)} \\ & - \frac{Q_0 t_p \left(\bar{n}^{I}_{11}\bar{C}^{I}\sqrt{\bar{\lambda}^{I}} + \bar{n}^{II}_{12}\bar{C}^{II}\sqrt{\bar{\lambda}^{II}} \right)}{2\sqrt{\pi} H L_e t_c}\sqrt{\Delta t} \end{aligned}$$

$$\bar{p}^{II}_{\text{line,w}}(\Delta t) \rightarrow \frac{Q_0 t_p \bar{n}^I_{21} \bar{C}^I \lambda^I}{4\pi H t_c}\left[\frac{2\sqrt{\pi t_c}}{\sqrt{\bar{\lambda}^I} L_e} Erf\left(\frac{\sqrt{\bar{\lambda}^I} L_e}{2\sqrt{t_c}}\right) + E_1\left(\frac{\bar{\lambda}^I L_e^2}{4t_c}\right)\right]$$
$$+ \frac{Q_0 t_p \bar{n}^{II}_{22} \bar{C}^{II} \bar{\lambda}^{II}}{4\pi H t_c}\left[\frac{2\sqrt{\pi t_c}}{\sqrt{\bar{\lambda}^{II}} L_e} Erf\left(\frac{\sqrt{\bar{\lambda}^{II}} L_e}{2\sqrt{t_c}}\right) + E_1\left(\frac{\bar{\lambda}^{II} L_e^2}{4t_c}\right)\right] \quad \text{..... (B-9)}$$
$$- \frac{Q_0 t_p \left(\bar{n}^I_{21} \bar{C}^I \sqrt{\bar{\lambda}^I} + \bar{n}^{II}_{22} \bar{C}^{II} \sqrt{\bar{\lambda}^{II}}\right)}{2\sqrt{\pi} H L_e t_c} \sqrt{\Delta t}$$

It can be observed that, at $\Delta t \rightarrow 0^+$, a straight-line behavior is expected in both plots of $\bar{p}^I$ and $\bar{p}^{II}$ vs. $\Delta t^{1/2}$.

Based on Eqs. B-8 and B-9, the pressure derivatives have the following asymptotic behavior during the pseudo-linear period:

$$-\frac{d\bar{p}^I_{\text{line,w}}(\Delta t)}{d\Delta t} \rightarrow \frac{Q_0 t_p \left(\bar{n}^I_{11} \bar{C}^I \sqrt{\bar{\lambda}^I} + \bar{n}^{II}_{12} \bar{C}^{II} \sqrt{\bar{\lambda}^{II}}\right)}{4\sqrt{\pi} H L_e t_c} \frac{1}{\sqrt{\Delta t}} \quad \text{..... (B-10)}$$

$$-\frac{d\bar{p}^{II}_{\text{line,w}}(\Delta t)}{d\Delta t} \rightarrow \frac{Q_0 t_p \left(\bar{n}^I_{21} \bar{C}^I \sqrt{\bar{\lambda}^I} + \bar{n}^{II}_{22} \bar{C}^{II} \sqrt{\bar{\lambda}^{II}}\right)}{4\sqrt{\pi} H L_e t_c} \frac{1}{\sqrt{\Delta t}} \quad \text{.....(B-11)}$$

or

$$-\Delta t \frac{d\bar{p}^I_{\text{line,w}}(\Delta t)}{d\Delta t} \rightarrow \frac{Q_0 t_p \left(\bar{n}^I_{11} \bar{C}^I \sqrt{\bar{\lambda}^I} + \bar{n}^{II}_{12} \bar{C}^{II} \sqrt{\bar{\lambda}^{II}}\right)}{4\sqrt{\pi} H L_e t_c} \sqrt{\Delta t} \quad \text{..... (B-12)}$$

$$-\Delta t \frac{d\bar{p}^{II}_{\text{line,w}}(\Delta t)}{d\Delta t} \rightarrow \frac{Q_0 t_p \left(\bar{n}^I_{21} \bar{C}^I \sqrt{\bar{\lambda}^I} + \bar{n}^{II}_{22} \bar{C}^{II} \sqrt{\bar{\lambda}^{II}}\right)}{4\sqrt{\pi} H L_e t_c} \sqrt{\Delta t} \quad \text{..... (B-13)}$$

It can be observed that, at $\Delta t \rightarrow 0^+$, the slope of -1/2 is expected in log-log plots of $-dp^I/d\Delta t$ and $-dp^{II}/d\Delta t$ vs. Δt, and the slope of 1/2 is expected in log-log plots of $-\Delta t dp^I/d\Delta t$ and $-\Delta t dp^{II}/d\Delta t$ vs. Δt.

Transient Period between Pseudo-Linear and Pseudo-Radial Regimes. When checking the solutions from the without-inter-porosity-flow case provided by Eq. B-7, it can be interesting to investigate the pressure derivatives asymptotic behavior at some intermediate time between the pseudo-linear and pseudo-radial flow regimes. In the case of without inter-porosity flow, the matrix pressure derivative can be obtained as follows:

$$\frac{dp^{I}_{\text{line,w}}(\Delta t)}{d\Delta t} = \frac{Q_0 t_p \bar{n}^{I}_{11} \bar{C}^{I} \sqrt{\bar{\lambda}^{I}}}{4\sqrt{\pi} H L_e t_c}\left[\frac{1}{\sqrt{t_c+\Delta t}}\,Erf\left(\frac{\sqrt{\bar{\lambda}^{I}}L_e}{2\sqrt{(t_c+\Delta t)}}\right)-\frac{1}{\sqrt{\Delta t}}\,Erf\left(\frac{\sqrt{\bar{\lambda}^{I}}L_e}{2\sqrt{\Delta t}}\right)\right] + \frac{Q_0 t_p \bar{n}^{II}_{12} \bar{C}^{II} \sqrt{\bar{\lambda}^{II}}}{4\sqrt{\pi} H L_e t_c}\left[\frac{1}{\sqrt{t_c+\Delta t}}\,Erf\left(\frac{\sqrt{\bar{\lambda}^{II}}L_e}{2\sqrt{(t_c+\Delta t)}}\right)-\frac{1}{\sqrt{\Delta t}}\,Erf\left(\frac{\sqrt{\bar{\lambda}^{II}}L_e}{2\sqrt{\Delta t}}\right)\right] \quad \text{(B-14)}$$

Recalling the Taylor theory, a smooth function $f(x)$ can be approximated by the following formula:

$$f(x+x_0) \approx f(x) + f'(x)x_0 \quad \text{(B-15)}$$

Setting $f(\Delta t) = \frac{1}{\sqrt{\Delta t}}\,Erf\left(\frac{\sqrt{\bar{\lambda}^{I}}L_e}{2\sqrt{\Delta t}}\right)$ and $x_0 = t_c$, Eq. B-16 can be approximated by the following formula:

$$\frac{dp^{I}_{\text{line,w}}(\Delta t)}{d\Delta t} \approx \frac{Q_0 t_p \bar{n}^{I}_{11} \bar{C}^{I} \sqrt{\bar{\lambda}^{I}}}{4\sqrt{\pi} H L_e}\left[-\frac{\sqrt{\bar{\lambda}^{I}}L_e e^{-\frac{\bar{\lambda}^{I}L_e^2}{4\Delta t}}}{2\sqrt{\pi}(\Delta t)^2}-\frac{Erf\left(\frac{\sqrt{\bar{\lambda}^{I}}L_e}{2\sqrt{\Delta t}}\right)}{2(\Delta t)^{3/2}}\right] + \frac{Q_0 t_p \bar{n}^{II}_{12} \bar{C}^{II} \sqrt{\bar{\lambda}^{II}}}{4\sqrt{\pi} H L_e}\left[-\frac{\sqrt{\bar{\lambda}^{II}}L_e e^{-\frac{\bar{\lambda}^{II}L_e^2}{4\Delta t}}}{2\sqrt{\pi}(\Delta t)^2}-\frac{Erf\left(\frac{\sqrt{\bar{\lambda}^{II}}L_e}{2\sqrt{\Delta t}}\right)}{2(\Delta t)^{3/2}}\right] \quad \text{(B-16)}$$

If there is some intermediate time Δt such that the following inequality and asymptotic behavior is held

$$\frac{\sqrt{\bar{\lambda}^{I}}L_e e^{-\frac{\bar{\lambda}^{I}L_e^2}{4\Delta t}}}{2\sqrt{\pi}(\Delta t)^2},\frac{\sqrt{\lambda^{II}}L_e e^{-\frac{\bar{\lambda}^{II}L_e^2}{4\Delta t}}}{2\sqrt{\pi}(\Delta t)^2}<<1;\ Erf\left(\frac{\sqrt{\bar{\lambda}^{I}}L_e}{2\sqrt{\Delta t}}\right),Erf\left(\frac{\sqrt{\bar{\lambda}^{II}}L_e}{2\sqrt{\Delta t}}\right)\approx 1 \quad \text{..... (B-17)}$$

then Eq. B-18 could be further approximated by the following formula:

$$-\frac{dp^{I}_{\text{line,w}}(\Delta t)}{d\Delta t}\approx\frac{Q_0 t_p\left(\bar{n}^{I}_{11}\bar{C}^{I}\sqrt{\bar{\lambda}^{I}}+\bar{n}^{II}_{12}\bar{C}^{II}\sqrt{\bar{\lambda}^{II}}\right)}{8\sqrt{\pi}HL_e}\frac{1}{(\Delta t)^{3/2}} \quad \text{..... (B-18)}$$

Then, the slope of -3/2 is expected at some intermediate time in the log-log plot of $-dp^{I}/d\Delta t$ vs. Δt.

or

$$-\Delta t\frac{dp^{I}_{\text{line,w}}(\Delta t)}{d\Delta t}\approx\frac{Q_0 t_p\left(\bar{n}^{I}_{11}\bar{C}^{I}\sqrt{\bar{\lambda}^{I}}+\bar{n}^{II}_{12}\bar{C}^{II}\sqrt{\bar{\lambda}^{II}}\right)}{8\sqrt{\pi}HL_e}\frac{1}{(\Delta t)^{1/2}} \quad \text{..... (B-19)}$$

Then, the slope of -1/2 is expected at some intermediate time in the log-log plot of $-\Delta t dp^{I}/d\Delta t$ vs. Δt.

Similar approximations for fracture pressure at some intermediate time also can be obtained as follows:

$$-\frac{dp^{II}_{\text{line,w}}(\Delta t)}{d\Delta t}\approx\frac{Q_0 t_p\left(\bar{n}^{I}_{21}\bar{C}^{I}\sqrt{\bar{\lambda}^{I}}+\bar{n}^{II}_{22}\bar{C}^{II}\sqrt{\bar{\lambda}^{II}}\right)}{8\sqrt{\pi}HL_e}\frac{1}{(\Delta t)^{3/2}} \quad \text{..... (B-20)}$$

$$-\Delta t\frac{dp^{II}_{\text{line,w}}(\Delta t)}{d\Delta t}\approx\frac{Q_0 t_p\left(\bar{n}^{I}_{21}\bar{C}^{I}\sqrt{\bar{\lambda}^{I}}+\bar{n}^{II}_{22}\bar{C}^{II}\sqrt{\bar{\lambda}^{II}}\right)}{8\sqrt{\pi}HL_e}\frac{1}{(\Delta t)^{1/2}} \quad \text{..... (B-21)}$$

Appendix C: After-Closure Wellbore Pressure Solution without Inter-Porosity Flow

Instantaneous Point Source. Supposing there is no inter-porosity flow between the matrix and fracture system, the governing equations of pressure can be obtained by setting $\Gamma = 0$ in Eq. B-1, which become

$$\frac{\partial}{\partial t}\begin{bmatrix} p^{I} \\ p^{II} \end{bmatrix} = A^{-1}D\nabla^{2}\begin{bmatrix} p^{I} \\ p^{II} \end{bmatrix} \quad \text{..... (C-1)}$$

Substituting Eq. A-7 into Eq. C-1 provides

$$\frac{\partial}{\partial t}\begin{bmatrix} \zeta^{I} \\ \zeta^{II} \end{bmatrix} = DA^{-1}\nabla^{2}\begin{bmatrix} \zeta^{I} \\ \zeta^{II} \end{bmatrix} \quad \text{..... (C-2)}$$

Using the method in Lesson 29 of Farlow (1982), the solutions of Eq. C-2 can be obtained in the time domain as follows:

$$\begin{bmatrix} \bar{\zeta}^{I}(r,t) \\ \bar{\zeta}^{II}(r,t) \end{bmatrix} = \bar{P}\begin{bmatrix} \dfrac{\bar{C}^{I}\bar{\lambda}^{I}}{4\pi t}e^{-\frac{r^{2}\bar{\lambda}^{I}}{4t}} \\ \dfrac{\bar{C}^{II}\bar{\lambda}^{II}}{4\pi t}e^{-\frac{r^{2}\bar{\lambda}^{II}}{4t}} \end{bmatrix} \quad \text{..... (C-3)}$$

where the symbol overbar denotes the solutions of the without-inter-porosity-flow case; the matrix $\bar{P}$ satisfies the following condition

$$\bar{P}^{-1}AD^{-1}\bar{P} = \begin{bmatrix} \bar{\lambda}^{I} & 0 \\ 0 & \bar{\lambda}^{II} \end{bmatrix} \quad \text{..... (C-4)}$$

and is denoted by

$$\bar{P} = \begin{bmatrix} \bar{m}_{11}^{I} & \bar{m}_{12}^{II} \\ \bar{m}_{21}^{I} & \bar{m}_{22}^{II} \end{bmatrix} \quad \text{..... (C-5)}$$

The matrix and fracture pressure influence resulting from an instantaneous point source with unit volume are

$$\begin{bmatrix} \bar{p}^{I}_{\text{inst,point}} \\ \bar{p}^{II}_{\text{inst,point}} \end{bmatrix} = A^{-1}\begin{bmatrix} \bar{\zeta}^{I} \\ \bar{\zeta}^{II} \end{bmatrix} = A^{-1}\bar{P}\begin{bmatrix} \dfrac{\bar{C}^{I}\bar{\lambda}^{I}}{4\pi t} e^{-\frac{r^2\bar{\lambda}^{I}}{4t}} \\ \dfrac{\bar{C}^{II}\bar{\lambda}^{II}}{4\pi t} e^{-\frac{r^2\bar{\lambda}^{II}}{4t}} \end{bmatrix} \quad \text{..... (C-6)}$$

$$= \begin{bmatrix} \bar{n}^{I}_{11}\dfrac{\bar{C}^{I}\bar{\lambda}^{I}}{4\pi t} e^{-\frac{r^2\bar{\lambda}^{I}}{4t}} + \bar{n}^{II}_{12}\dfrac{\bar{C}^{II}\bar{\lambda}^{II}}{4\pi t} e^{-\frac{r^2\bar{\lambda}^{II}}{4t}} \\ \bar{n}^{I}_{21}\dfrac{\bar{C}^{I}\bar{\lambda}^{I}}{4\pi t} e^{-\frac{r^2\bar{\lambda}^{I}}{4t}} + \bar{n}^{II}_{22}\dfrac{\bar{C}^{II}\bar{\lambda}^{II}}{4\pi t} e^{-\frac{r^2\bar{\lambda}^{II}}{4t}} \end{bmatrix}$$

where

$$A^{-1}\bar{P} = \begin{bmatrix} \bar{n}^{I}_{11} & \bar{n}^{II}_{12} \\ \bar{n}^{I}_{21} & \bar{n}^{II}_{22} \end{bmatrix} \quad \text{..... (C-7)}$$

Calculation of the Constants. By using the same idea as the previous calculation in Appendix A, the constants can be determined using the following two equations:

$$\left(\bar{m}^{I}_{11} + \bar{m}^{I}_{21}\right)\frac{\bar{C}^{I}}{2\pi} + \left(\bar{m}^{II}_{12} + \bar{m}^{II}_{22}\right)\frac{\bar{C}^{II}}{2\pi} = \frac{1}{2\pi} \quad \text{..... (C-8)}$$

$$\bar{m}^{I}_{11}\frac{\bar{C}^{I}}{2\pi} + \bar{m}^{II}_{12}\frac{\bar{C}^{II}}{2\pi} = \frac{\mathrm{v}^{I}}{2\pi} \quad \text{..... (C-9)}$$

or

$$\begin{pmatrix} \bar{C}^{I} \\ \bar{C}^{II} \end{pmatrix} = \begin{pmatrix} \bar{m}^{I}_{11} & \bar{m}^{II}_{12} \\ \bar{m}^{I}_{21} & \bar{m}^{II}_{22} \end{pmatrix}^{-1}\begin{pmatrix} \mathrm{v}^{I} \\ \mathrm{v}^{II} \end{pmatrix} \quad \text{..... (C-10)}$$

Line Source Simulation. First, matrix and fracture pressure influences resulting from the instantaneous line source with unit intensity can be obtained by integrating the instantaneous point source solutions along the fracture length 2*L* as follows:

$$\begin{bmatrix} \overline{p}^{I}_{\text{inst,line}} \\ \overline{p}^{II}_{\text{inst,line}} \end{bmatrix}(x,y) = \int_{-L}^{L} \begin{bmatrix} \overline{n}^{I}_{11} \dfrac{\overline{C}^{I}\overline{\lambda}^{I}}{4\pi t} e^{-\frac{r^2\overline{\lambda}^{I}}{4t}} + \overline{n}^{II}_{12} \dfrac{\overline{C}^{II}\overline{\lambda}^{II}}{4\pi t} e^{-\frac{r^2\overline{\lambda}^{II}}{4t}} \\ \overline{n}^{I}_{21} \dfrac{\overline{C}^{I}\overline{\lambda}^{I}}{4\pi t} e^{-\frac{r^2\overline{\lambda}^{I}}{4t}} + \overline{n}^{II}_{22} \dfrac{\overline{C}^{II}\overline{\lambda}^{II}}{4\pi t} e^{-\frac{r^2\overline{\lambda}^{II}}{4t}} \end{bmatrix} dx' \quad \text{.....(C-11)}$$

Especially at the origin (0,0),

$$\begin{bmatrix} \overline{p}^{I}_{\text{inst,line}} \\ \overline{p}^{I}_{\text{inst,line}} \end{bmatrix}(0,0) = \begin{bmatrix} \overline{n}^{I}_{11} \dfrac{\overline{C}^{I}\sqrt{\overline{\lambda}^{I}}}{2\sqrt{\pi t}} Erf\left(\dfrac{\sqrt{\overline{\lambda}^{I}}L}{2\sqrt{t}}\right) + \overline{n}^{II}_{12} \dfrac{\overline{C}^{II}\sqrt{\overline{\lambda}^{II}}}{2\sqrt{\pi t}} Erf\left(\dfrac{\sqrt{\overline{\lambda}^{II}}L}{2\sqrt{t}}\right) \\ \overline{n}^{I}_{21} \dfrac{\overline{C}^{I}\sqrt{\overline{\lambda}^{I}}}{2\sqrt{\pi t}} Erf\left(\dfrac{\sqrt{\overline{\lambda}^{I}}L}{2\sqrt{t}}\right) + \overline{n}^{II}_{22} \dfrac{\overline{C}^{II}\sqrt{\overline{\lambda}^{II}}}{2\sqrt{\pi t}} Erf\left(\dfrac{\sqrt{\overline{\lambda}^{II}}L}{2\sqrt{t}}\right) \end{bmatrix} \text{..... (C-12)}$$

Then, for a continuous line source with unit intensity, the pressure influences at the origin are as follows:

$$\begin{bmatrix} \overline{p}^{I}_{\text{cont,line}} \\ \overline{p}^{II}_{\text{cont,line}} \end{bmatrix}(0,0) = \int_{0}^{t} \begin{bmatrix} \overline{n}^{I}_{11} \dfrac{\overline{C}^{I}\sqrt{\overline{\lambda}^{I}}}{2\sqrt{\pi t'}} Erf\left(\dfrac{\sqrt{\overline{\lambda}^{I}}L}{2\sqrt{t'}}\right) + \overline{n}^{II}_{12} \dfrac{\overline{C}^{II}\sqrt{\overline{\lambda}^{II}}}{2\sqrt{\pi t'}} Erf\left(\dfrac{\sqrt{\overline{\lambda}^{II}}L}{2\sqrt{t'}}\right) \\ \overline{n}^{I}_{21} \dfrac{\overline{C}^{I}\sqrt{\overline{\lambda}^{I}}}{2\sqrt{\pi t'}} Erf\left(\dfrac{\sqrt{\overline{\lambda}^{I}}L}{2\sqrt{t'}}\right) + \overline{n}^{II}_{22} \dfrac{\overline{C}^{II}\sqrt{\overline{\lambda}^{II}}}{2\sqrt{\pi t'}} Erf\left(\dfrac{\sqrt{\overline{\lambda}^{II}}L}{2\sqrt{t'}}\right) \end{bmatrix} dt' \text{ ..... (C-13)}$$

or

$$\begin{bmatrix} \overline{p}^{I}_{\text{cont,line}} \\ \overline{p}^{II}_{\text{cont,line}} \end{bmatrix}(0,0) = \begin{bmatrix} \dfrac{\overline{n}^{I}_{11}\overline{C}^{I}\overline{\lambda}^{I}L}{2\pi} \left\{ \dfrac{2\sqrt{\pi t}}{\sqrt{\overline{\lambda}^{I}}L} Erf\left(\dfrac{\sqrt{\overline{\lambda}^{I}}L}{2\sqrt{t}}\right) + E_1\left(\dfrac{\overline{\lambda}^{I}L^2}{4t}\right) \right\} \\ + \dfrac{\overline{n}^{II}_{12}\overline{C}^{II}\overline{\lambda}^{II}L}{2\pi} \left\{ \dfrac{2\sqrt{\pi t}}{\sqrt{\overline{\lambda}^{II}}L} Erf\left(\dfrac{\sqrt{\overline{\lambda}^{II}}L}{2\sqrt{t}}\right) + E_1\left(\dfrac{\overline{\lambda}^{II}L^2}{4t}\right) \right\} \\ \dfrac{\overline{n}^{I}_{21}\overline{C}^{I}\overline{\lambda}^{I}L}{2\pi} \left\{ \dfrac{2\sqrt{\pi t}}{\sqrt{\overline{\lambda}^{I}}L} Erf\left(\dfrac{\sqrt{\overline{\lambda}^{I}}L}{2\sqrt{t}}\right) + E_1\left(\dfrac{\overline{\lambda}^{I}L^2}{4t}\right) \right\} \\ + \dfrac{\overline{n}^{II}_{22}\overline{C}^{II}\overline{\lambda}^{II}L}{2\pi} \left\{ \dfrac{2\sqrt{\pi t}}{\sqrt{\overline{\lambda}^{II}}L} Erf\left(\dfrac{\sqrt{\overline{\lambda}^{II}}L}{2\sqrt{t}}\right) + E_1\left(\dfrac{\overline{\lambda}^{II}L^2}{4t}\right) \right\} \end{bmatrix} \text{..... (C-14)}$$

where $E_1(x)$ and $Erf(x)$ are the exponential integral function and error function, respectively.

For an injection of a volume of $Q_0 t_p$ for a duration t_c, the matrix and fracture pore pressure at the origin can be expressed in the time domain as follows:

$$\begin{bmatrix} \bar{p}^{I}_{\mathrm{line,w}}(\Delta t) \\ \bar{p}^{II}_{\mathrm{line,w}}(\Delta t) \end{bmatrix} = \frac{Q_0 t_p}{4\pi H t_c} \begin{bmatrix} \bar{n}^{I}_{11}\bar{\lambda}^{I} & \bar{n}^{II}_{12}\bar{\lambda}^{II} \\ \bar{n}^{I}_{21}\bar{\lambda}^{I} & \bar{n}^{II}_{22}\bar{\lambda}^{II} \end{bmatrix}$$

$$\cdot \begin{bmatrix} \bar{C}^{I}\left\{ \frac{2\sqrt{\pi(t_c+\Delta t)}}{\sqrt{\bar{\lambda}^{I}}L_e} Erf\left(\frac{\sqrt{\bar{\lambda}^{I}}L_e}{2\sqrt{(t_c+\Delta t)}} \right) - \frac{2\sqrt{\pi \Delta t}}{\sqrt{\bar{\lambda}^{I}}L_e} Erf\left(\frac{\sqrt{\bar{\lambda}^{I}}L_e}{2\sqrt{\Delta t}} \right) + E_1\left(\frac{\bar{\lambda}^{I}L_e^2}{4(t_c+\Delta t)} \right) - E_1\left(\frac{\bar{\lambda}^{I}L_e^2}{4\Delta t} \right) \right\} \\ \bar{C}^{II}\left\{ \frac{2\sqrt{\pi(t_c+\Delta t)}}{\sqrt{\bar{\lambda}^{II}}L_e} Erf\left(\frac{\sqrt{\bar{\lambda}^{II}}L_e}{2\sqrt{(t_c+\Delta t)}} \right) - \frac{2\sqrt{\pi \Delta t}}{\sqrt{\bar{\lambda}^{II}}L_e} Erf\left(\frac{\sqrt{\bar{\lambda}^{II}}L_e}{2\sqrt{\Delta t}} \right) + E_1\left(\frac{\bar{\lambda}^{II}L_e^2}{4(t_c+\Delta t)} \right) - E_1\left(\frac{\bar{\lambda}^{II}L_e^2}{4\Delta t} \right) \right\} \end{bmatrix}$$

..... (C-15)